University of Strathclyde

Department of Electronic and Electrical Engineering

On a dual wavelength optical sensor system for measuring strain and temperature simultaneously in tokamak port plug

By

Paul Crolla

MSci

A thesis presented in
partial fulfilment of the
requirements for the
Degree
of
Doctor of Philosophy

2014

This thesis is the result of the author‘s original research. It has been composed by the author and has not been previously submitted for examination which has led to the award of a degree.

Signed:

Date:

‘It always seems impossible until it’s done.‘

Nelson Mandela

Abstract

A large variety of sources will provide energy, including nuclear fusion energy from tokamak type reactors; still at a research stage of development to produce 500 MW of energy. The reactor's structure will be affected by temperature changes and ionising radiation (neutrons produced by the burning plasma); it is therefore necessary to instrument the structure with long lasting, accurate, temperature and strain monitoring devices. This thesis demonstrates that using electrical sensors in the supporting structures of a fusion reactor for measuring strain and temperature will be strongly affected by the ionising radiation and the electromagnetic fields. This is because it was found that errors of over 100% can be present on the measurements due to combined electromagnetic and radiation effects. An optical fibre sensor was constructed to a strain resolution of $\pm 10\mu\epsilon$ and temperature resolution of ±5°C. The fibre sensor is an off the shelf solution dual-wavelength fibre Bragg grating. The thesis proposes a method of coating the fibre in layers of silver and copper to protect this sensor. A new method of embedding the fibre in a stainless steel piece is described using a silver solder to couple the fibre with the steel increasing its temperature and strain sensitivity by approximately three times, with the solder melted using an induction heater. To measure the temperature and strain response from the fibre Bragg grating a broadband optical filter was used as a real-time interrogation system. Data capture and analysis software solution was created running at 30Hz and ~1pm resolution; temperature and strain requirements were met. This work describes a method of performing measurements of strain and temperature not subject to electromagnetic interference, with good electrical isolation possible and capable of operating in a near vacuum. The sensor package provides a robust, weldable solution for connecting the sensor to the port plug structure and/ or plasma instrumentation equipment that will provide regular repeatable measurements of strain and temperature.

Acknowledgements

Firstly, I would like to thank my parents for their love and support through my long years of studying; providing a roof over my head, free meals and a good grounding.

A sincere gratitude to Professor Sir Jim McDonald and Professor Graeme Burt for giving me the opportunity to study for a PhD within their research group and for being able to support me to the completion of it.

I would also like to thank my friends, within the Group and beyond, who have helped me through the tough times, the good times and everything in-between. You were always ready to share a whisky or two with me when times were tough. Grzegorz and Philip cannot pass without specific mention for they have assisted me through many tough challenges both intellectual and practical.

I would also like to acknowledge Bob in the electronics workshop for his excellent work in preparing my circuit ideas. George, Jim, David, and Davie for putting up with my complete lack of knowledge of metal craft and making my ideas become reality.

Finally, I must thank Dr Pawel Niewczas for, firstly, agreeing to supervise a young, over-enthusiastic physicist; secondly, for putting up with my non-straightforward attitude to work; and thirdly, for providing guidance when I had taken a wrong turn. For all this an more I am forever grateful.

Contents

Appendix:

List of Tables

List of Figures

Abbreviations

ac	Alternating Current
ADC	Analogue-to-Digital Converter
ASE	Amplified Spontaneous Emission
AWG	Arrayed WaveGuide
CCG	Chemical Composition Grating
CMOS	Common Metal Oxide Semiconductor
DAC	Digital-to-Analogue Converter
DAQ	Data Acquisition system
DAQ	Digital AcQuisition Board
dc	Direct Current
DEMO	DEMOnstration Power Plant
DWDM	Dense Wave Division Multiplexing
EFPI	Extrinsic Fabry-Perot Interferometer
EMI	Electromagnetic interference
EMI	Electromagnetic Interference
FBG	Fibre Bragg Grating
FBG	Fibre Bragg Grating
FC/APC	Fibre-optic Connector/ Angled Physical Contact
FFP	Fibre Fabry-Perot
FFT	Fast Fourier Transform
FP	Fabry-Perot
FP	Fabry-Perot Interferometer
FP-TF	Fabry-Perot Tuneable Filter
FPI	Fabry-Perot Interferometer
Intrinsic FSO	Full Scale Output
FSR	Free Spectral Range
FWHM	Full Width Half Maximum
GFDL	GNU Free Documentation License
I/O	Input/ Output
I/P	Input
IR	Infra-red

IS	Interrogation System
ITU	International Telecommunication Union
JET	Joint European Torus
LED	Light emitting diode
LIDAR	Light Detection And Ranging
MAST	MegaAmpere Spherical Tokamak
MEMS	Micro-Electro-Mechanical Systems
MHD	Magnetic Displacement Event
MM	Multi-mode
NPP	Nuclear Power Plant
O/P	Output
OFS	Optical Fibre Sensors
OSA	Optical Spectrum Analyser
PC	Personal Computer
PCI	Peripheral Component Interconnect
PIN	P-type, Intrinsice, N-type semiconductor
PM	Polarisation Maintaining
PXI	PCI eXtensions for Instrument control
RIA	Radiation Induced Attenuation
RIC	Radiation Induced Conductivity
RIED	Radiation Induced Electrical Degradation
RIEMF	Radiation Induced ElectroMotive Force
rms	Root Mean Square
RT	Real Time
SFS	Super Fluorescent Source
SLD	Superluminescent Diode
SM	Singlemode
SMF	SingleMode Fibre
SNR	Signal to Noise Ratio
SS	Stainless Steel
TEC	Thermoelectric Cooler
TIEMF	Temperature Induced ElectroMotive Force

TTL	Transistor-Transistor Logic
UKAEA	United Kingdom Atomic Energy Authority
USA	United States of America
UV	Ultraviolet
VDE	Vertical Displacement Event
WDM	Wave Division Multiplexing

Symbols list

α	thermal expansion coefficient of material
α_f	Coefficient of thermal expansion of optical fibre
α_N	Constant for Newton's heating law
α_p	Molecular polarizability
α_s	Coefficient of thermal expansion of surrounding material
$\alpha_s c$	Seebeck coefficient
$\alpha_s c(x)$	Seebeck coefficient at position x
β_{ij}	Contracted strain optic tensor of the fibre
δ	Wavelength reading error
$\Delta\epsilon$	Change in linear strain
$\Delta\epsilon$	Change in strain
$\Delta\epsilon_{temp}$	Change in strain due to change in temperature
$\Delta\Lambda$	Change in grating period
$\Delta\lambda_{B1}$	Change in wavelength of grating 1
$\Delta\lambda_{B2}$	Change in wavelength of grating 2
$\Delta\lambda_{temp}$	Change in wavelength due to change in temperature
$\Delta\lambda_{total}$	Total change in Bragg wavelength
$\Delta\lambda_B$	Change in Bragg wavelength
ΔE	Electromotive force or voltage from thermocouple
Δl	Change in length of beam
ΔL_f	Change in length of fibre
ΔL_m	Change in length of surrounding material

Δn	difference between core and cladding refractive indexes
$\Delta n_{mod}(0)$	refractive index modulation at time 0
$\Delta n_{mod}(t)$	refractive index modulation at time t
ΔT	Change in temperature
ΔT_{TC}	Difference in temperature between the thermocouple and termini
ΔV	Change in volume
δ_e	Optical phase shift
$\Delta\lambda_{B\epsilon}$	Change in Bragg wavelength due to change in strain
$\boldsymbol{\Phi}_0$	True values of measurement variables
$\boldsymbol{\Phi}$	Measurement variables matrix
$\mathbf{K_0}$	True values of characteristic matrix of sensor
$\mathbf{K}$	Characteristic matrix of sensor
ϵ	strain
ϵ_{cc}	Material specific constant for normalised integrated coupling constant
ϵ_{ij}	block-reduced strain tensor
ϵ_V	Volumetric strain
ϵ_z	strain in z direction along fibre
η	overlap between fundamental and core mode
η_{cc}	normalised integrated coupling constant
K_ϵ	Strain dependence of Bragg wavelength
K_T	Temperature dependence of Bragg wavelength
l_{TC}	lenght of thermocouple
Λ	period of refractive index change
λ	Wavelength
λ_B	Bragg wavelength of FBG
ν	Poisson's ratio of material
Φ_1	Measurement variable 1
Φ_2	Measurement variable 2
Φ_op	Incident optical power
ρ	Resistivity
ρ_d	density
$\sigma(T)$	Conductance at temperature T

σ_0^{MI}	Initial conductance of mineral insulated cable
$\sigma_R^{MI}IC$	Conductance of mineral insulated cable due to RIC
σ_e	RMS value of the quantisation noise
σ_e^2	Quantisation noise power
Θ_{FP}	Angle of transmitted beams
ζ	thermo-optic coefficient
A	Area
A_{sensor}	Area of sensor
A_{tp}	Area from twisted pair cable
a	Constant that relates current generated in cable due to reactor power
A_{sig}	Amplification factor of the pre-amp
a_f	Maximum power of Gaussian function
Al	Aluminium elemental symbol
B	magnetic flux density
b_{cc}	Material specific constant for normalised integrated coupling constant
$b_{current}$	Residual current in wire
B_{ph}	Post-conversion electrical bandwidth of the system
B_{0cc}	Material specific constant for normalised integrated coupling constant
b_f	average value of Gaussian function
c	Constant that relates cable resistance to reactor power
c_f	Variable for Gaussian function
C_p	Heat capacity
$Co-60$	Elemental symbol for Cobalt 60
D	Deuterium elemental symbol
d_{FP}	Separation of etalon mirrors
d_{RIC}	RIC material constant
e	Elementary charge
e_{max}	Maximum quantisation error
e_{sh}	rms shot noise voltage
e_{th}	Circuit RMS voltage
E_H	Heating energy
E_o	Voltage output of transimpedance amplifier

F_e	Finesse of etalon
F_w	FWHM of Gaussian
Ge	Elemental symbol for Germanium
h	Height
He	Helium elemental symbol
I	current
I_{ph}	average current generated by photons flowing through the photodiode
I_{sh}	Shot noise current
I_i	Incident optical intensity
I_p	Photodiode current
$I_t(\delta_e)$	Transmitted intenstity
$K_{\epsilon i}$	Sensitvity of FBG i to strain
K_B	Boltzmann's constant
K_{RIC}	RIC material constant
K_{Ti}	Sensitvity of FBG i to temperature
l	Length
l_0	Initial length of beam
L_0	Original length of fibre
l_g	length of guage material
L_gr	Length of grating
m_m	molar mass of molecule
N	Number of grating periods
n	refractive index
n_{FP}	Cavity's refractive index
n_1	Unaltered core refractive index of FBG
n_2	Altered core refractive index of FBG
n_eff	Effective refractive index of FBG
N_m	
O	Oxygen elemental symbol
$p_{11}p_{12}$	Components of the fibre optic strain tensor
P_{1310}	Optical power spectrum of 1310nm SLD
P_{1550}	Optical power spectrum of 1550nm SLD

$P_{REACTOR}$	Thermal power of nuclear fission reactor
p_α	relates change in strain to change in Bragg wavelength
$p.d.$	potential difference
q	quantisation between digital levels in analogue to digital capture system
R	Resistance
R_{idr}	Ionisation dose rate
R_f	Resistance of feedback resistor in transimpedance amplifier
R_m	Fractional reflectance of etalon mirrors
R_p	Responsivity of the photodiode
Si	Elemental symbol for silicon
T	Temperature
T	Tritium elemental symbol
T_{0cc}	Material specific constant for normalised integrated coupling constant
T_s	Surrounding temperature
$T(t)$	Material temperature at time t
VK^{-1}	Volts per Kelvin
V_{RIEMF}	Voltage between sheath and core of cable due to RIEMF
V_0	Initial volume
w	Width

Chapter 1

Introduction

The use of sensor systems for monitoring large and complex infrastructure has been increasing in recent years; this is due to increasing plant complexity, the need to operate systems closer to their limits (combined with longer system lifetimes), to maximise their usage and the decreasing costs of the sensor systems and hence their affordability. Sensor systems and ruggedised packages for many environments have been developed and deployed; however, little work has been carried out in the deployment of condition monitoring sensors for the nuclear fusion environment.

The future development of nuclear fusion reactors will provide a sustainable energy source. The next generation nuclear fusion research device, called ITER, Latin for *the way* (originally an acronym of International Thermonuclear Experimental Reactor), will be the largest ever built; with a volume ten times that of JET (Joint European Torus), which is the world's largest fusion reactor currently. It is for the ITER and future DEMO (DEMOnstration Power Plant) [1] environments that this thesis sets out to propose a method and a system for monitoring temperature and strain using packaged fibre optic sensors.

1.1 Research Motivation

The ITER reactor will operate at the extremes of material science and mechanical engineering. This is due to the very high temperatures required to facilitate fusion, and the high energy radiation emitted from the reaction causing the degradation of surrounding materials. Furthermore, very high field superconducting magnets (up to $5\,T$) have never been used before on such a scale.

In [2] four cases are identified where structural monitoring may be required, these are

(i) structures subject to continuous vibration or degradation of materials,

(ii) feedback loop to improve future design based on experience,

(iii) novel methods of construction,

(iv) decline in construction and growth in maintenance needs.

The above cases support the need for significant structural monitoring of the ITER reactor and support systems. Each case is applied to the ITER scenario below.

(i) A nuclear fusion reactor's structure will be continuously degrading as both the ionising radiation will penetrate all parts of the structure and the high temperatures of the plasma vessel will cause the wall structure to be damaged.

(ii) The purpose of ITER is to test technologies and materials for the future commercial application of fusion for energy generation. It is important therefore that as much data is gathered about the effect of radiation on the supporting structures as possible. The analysis of this data will be used to influence the design(s) of the next generation of fusion reactors.

(iii) A number of methods have been suggested for the construction of port plug structures on ITER, none of which have been tested before in a nuclear fusion environment and as such they will require careful monitoring throughout the reactor's lifetime.

(iv) Once ITER is built it is envisaged that there will be no significant changes to the reactor for at least ten years after the first plasma ignition, and all maintenance will be performed by robotic handling equipment controlled remotely as the radiation levels are lethal to human operators. To be able to make an assessment of the levels of maintenance required sufficient data must be available so that down-time of the machine can be minimised thus maximising experimental uptime.

To be able to use the machine safely at these physical limits there is a requirement for adequate high performance condition monitoring. The measurement of physical variables such as temperature, pressure, strain and radiation flux is required. This thesis shall examine the simultaneous point measurement of temperature and strain. This information could then be interpreted to create the stress field of the device.

The stress and temperature fields of the device are very important in the monitoring of deformations and for the safety case. It is envisaged that monitoring instrumentation will be directly linked into the control system thus making sure that the operators have full knowledge of the system state at all times.

Electrical sensing technology is currently used on the Joint European Torus (JET), the largest controlled nuclear fusion reactor at the present time. After an upgrade to the plasma systems at JET, allowing a higher energy plasma for a longer period to be produced, spurious noise signatures were detected on the strain gauge lines used to monitor the legs or struts of the supporting structure. It is possible that in the ITER reactor the larger $\mathbf{H}$ will create even higher levels of EMI.

1.2 Background to the research

The research activities reported in this thesis were undertaken in association with a United Kingdom Atomic Energy Authority, Fusion Division, (UKAEA Fusion) research project, namely, "The Development of A Demonstration System for Measuring Strain and Temperature in an ITER Port Plug."

The project's principal objective was to develop an optically-based measurement system capable of strain and temperature monitoring within the environment of an ITER port plug. This required the evaluation of state of the art optical sensors that could be integrated into the port plug's metallic structure and not adversely affect it. A suitable interrogation system capable of dual-wavelength discrimination was also required; this is because two measurements must be made to be able to distinguish changes in strain from differences in temperature.

The project principal achievement was the construction of a laboratory demonstrator consisting of a cantilever beam with embedded sensor held within an oven and capable of simultaneous strain and temperature measurements.

This demonstrator system required the creation of following components:

- Wide bandwidth fibre optic based interrogation system (wavelength selection component, photoreceiver module, novel power supply for filter)
- Advanced control software for the optical interrogation system, the creation of novel wavelength referencing technique
- Metal encapsulated fibre optic sensor that responds in a repeatable way to strain and temperature changes

1.3 Research Objectives

The research presented in this thesis is related to the development of a robust solution for the remote monitoring of strain and temperature at remote locations throughout an ITER port plug. Thus there are two objectives required to meet this aim.

(i) To develop a weldable, high-temperature optical fibre sensor to detect changes in strain (within $10\mu\epsilon$ and temperature (within 5°C) simultaneously.

(ii) To develop a suitable measurement system capable of discriminating between strain and temperature.

1.4 Contribution to the research

In terms of novelty of the research undertaken, the following contributions can be identified:

- The effects of ionising radiation present in nuclear fusion reactor port plugs on electrical sensors is quantified an an error analysis provided
- New method for the embedding of optical fibre sensors in stainless steel
- Design of the system for embedding optical fibre sensors in stainless steel
- Control software of a piezo-electric wide-band optical filter.
- Linearisation of the output of the optical filter
- Development of a real-time signal processing platform allowing for the implementation of innovative software solutions to improve the accuracy and interrogation speed of spectrally encoded sensors.
- Modelling of the use of a dual-wavelength sensor to make accurate, simultaneous, measurements of strain and temperature

1.5 Thesis Outline

This thesis has been split into seven principal chapters and these are described below.

Chapter 1 describes the background to this piece of research, the reasons and motivation for performing this work, the research objectives of the thesis, the thesis' contribution to knowledge, this thesis outline and the publications associated with this thesis.

Chapter 2 describes the principles of measuring temperature and strain using electrical sensors. It then explains the problems associated with such sensors in the environment required for operation of a nuclear fusion reactor, including the temperature, pressure and radiation. Only the details required to make the case for the use of an optical method is presented here and further technical detail can be found in the open literature.

Chapter 3 overviews the fundamental operation of the optical components used within the measurement system. It reviews the different types of optical sensors that could be used and defines the reasons for selecting the chemical composition grating. Further technical details can be found in the open literature. This chapter also contains the background theory on metal coating and embedding of optical fibres, presenting several methods for performing both.

Chapter 4 describes the use of a piezoelectric Fabry-Pérot wide-band tuneable filter in a sensor interrogation system. Various system topologies are proposed and the details of the potentially most successful solution are presented. In addition, the system measurement errors and capabilities are analysed and discussed in detail.

Chapter 5 describes the design and manufacturing procedure for the creation of a steel embedded, metal-coated, chemical composition grating. The initial experimental results are described and combined with a series of finite element models to demonstrate the viability of this approach to embedding in stainless steel.

Chapter 6 presents the calibration of the interrogation system and the response of the created sensor package to temperature and strain changes. It also describes the methodology used to compensate, in real-time, for the non-linearity of the tuneable filter response.

Chapter 7 summaries the principle conclusions of the work carried out, highlighting the main achievements, and proposes further research and development work to build on the results to date.

1.6 Associated Publications

P. Crolla, P. Niewczas, and J. R. McDonald, "An alternative method for the measurement of strain and temperature in a nuclear reactor," UPEC 2009, Glasgow, UK, Sept. 2009.

P. Niewczas, G. Fusiek, C. Lescure, M. Johnson, E. Ivings, A. West, P. Crolla, and M. Walsh, "Concept level evaluation of the full-scale deployment of fibre Bragg grating sensors for measuring forces in JET during plasma disruption events", Proceedings of Condition Monitoring 2008, Edinburgh, UK, Sept. 2008.

P. Crolla, "Temperature and strain measurement using a metal embedded dual wavelength optical sensor," Presentation, Research Presentation Day, Faculty of Engineering, University of Strathclyde, January 2008.

P. Crolla,"Development of a Photonic Dual Temperature and Strain Sensor for Condition Monitoring of an ITER Port Plug", invited presentation at The Rank Prize Funds, Mini-Symposium on Photonics and Optics in Sustainable Energy, Grasmere, UK, Nov. 2007.

P. Crolla, "Advanced sensors for condition monitoring of an ITER port plug," Poster, Research Presentation Day, Faculty of Engineering, University of Strathclyde, January 2007.

Chapter 2

Strain and Temperature Measurement Techniques

2.1 Introduction

In this chapter the definition of an ITER port plug along with the definitions of strain and temperature and techniques to measure them using electrical sensors are discussed. Each sensor is described in technical detail and the effects of temperature, radiation and electromagnetic fields on the operation of these sensors are then explored and quantified. The chapter finishes with a number of case studies of the combined effects of the port plug environment on strain and temperature measurements using electrical sensors. This thesis does not fully consider all the secondary systems required to monitor the mechanical structures supporting the tokamak.

2.2 An ITER Port Plug

The ITER tokamak reactor is an experimental nuclear fusion vessel designed to solve the engineering challenges of operating a nuclear fusion reaction for extended periods. The burning plasma will be monitored by many different diagnostic techniques, including LIDAR (Light Detection And Ranging), which will make measurements of plasma temperature, density, impurity concentration, and energy and particle confinement times. This will provide information to the reactor control systems and also allow the improvement of reactor performance and efficiency.

These diagnostic systems will be housed in removable structures called 'port plugs'. The port plugs will be attached to the reactor vessel on the upper and equatorial areas of the vessel, see Figure 2.1 for outline placement of the port plugs.

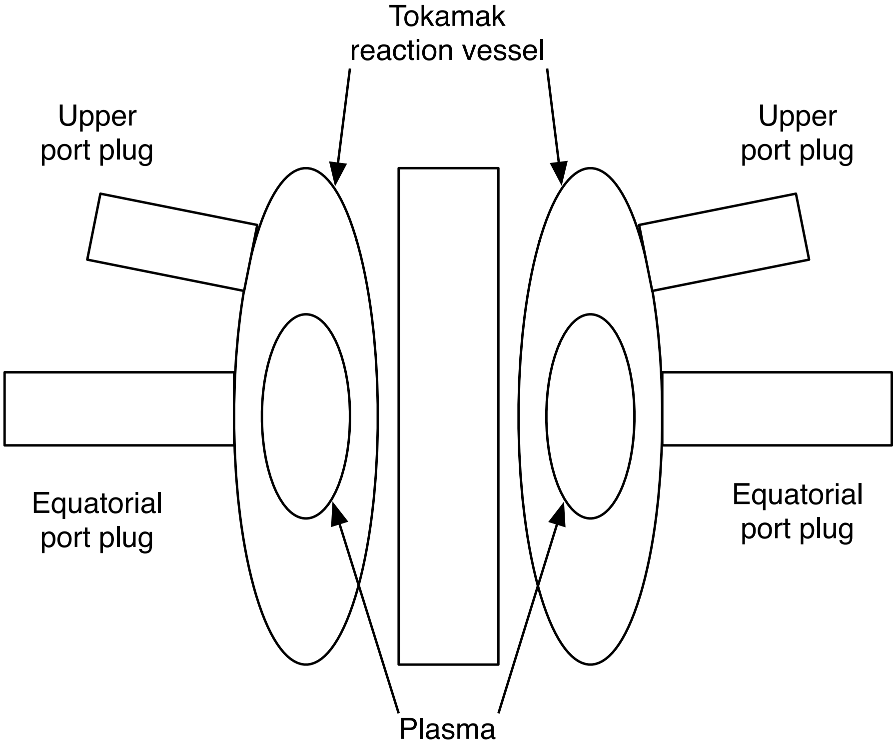

Figure 2.1: Outline diagram of tokamak structure showing positions of port plugs relative to the plasma

In Figure 2.2 is shown the naming scheme of the walls of the port plug relative to the rest of the reactor structure.

For this thesis a port plug being designed and built by the UKAEA is considered

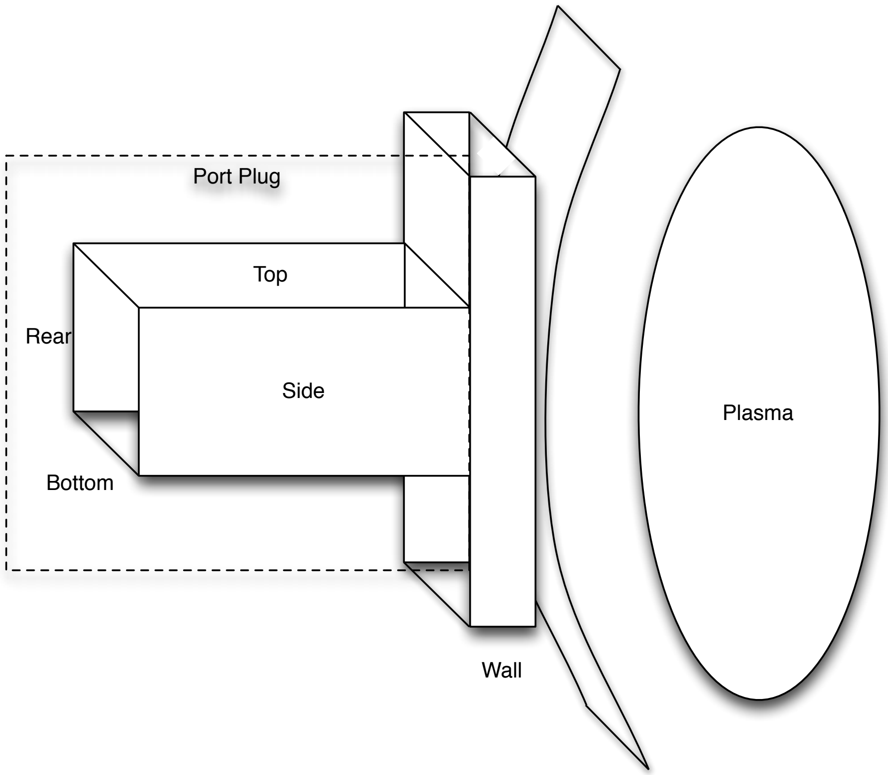

Figure 2.2: Diagram showing the different walls of the port plug and their relation to the plasma

as a case study. This port plug will contain a LIDAR system [3].

2.3 Strain Measurement

To be able to accurately measure strain one must have an accurate definition of strain. There are two types of strain, engineering and true strain [4] , it is possible to convert between these. In this work it is the engineering strain that is considered as the changes in strain are predicted to be within the valid measurement range of engineering strain.

2.3.1 Definition of Engineering Strain

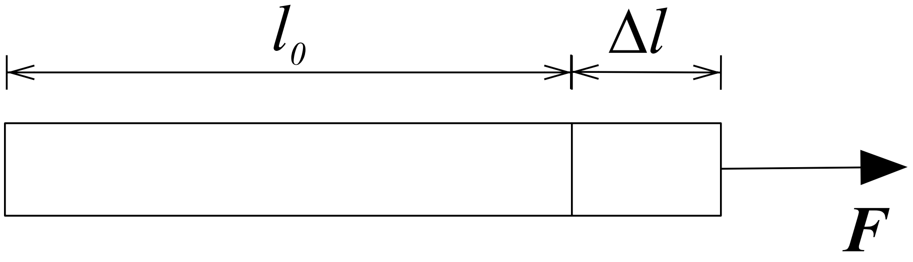

Figure 2.3: Example of a beam stretched by a linear force

In one dimension engineering strain ϵ is defined as the ratio of the change in length against the length before force applied. This is expressed in the formula below[5]

$$strain(\epsilon) = \frac{\Delta l}{l_0}. \tag{2.1}$$

where l_0 is the length of the object before any force is applied and Δl is the difference in length between the original length and current length; these variables are graphically expressed in Figure 2.3. Strain is a dimensionless measurand; however it is usually denoted by ϵ or more commonly, due to the small changes generally present, in $\mu\epsilon$ or micro-strain.

Strain can also be described in three dimensions as,

$$Volumetric\,Strain(\epsilon_v) = \frac{\Delta V}{V_0}, \tag{2.2}$$

where ϵ_v is the volumetric strain, the total strain in three dimensions, ΔV is the change in volume due to strain change in one or more directions and V_0 is the original volume of the material under investigation. This thesis is only concerned with the measurement of linear engineering strain. This is because linear engineering strain is applicable up to strains of 1% [4] .

2.3.2 Strain Measuring Devices

Foil Strain Gauges

The measurement of strain has been traditionally performed using electrical strain gauges. These gauges operate via a strain to resistance change transformation, i.e.,

$$R = \rho\frac{l}{A}, \tag{2.3}$$

where R is the resistance of the strain gauge, A (m^2) is the area in of the conductor plane transverse to the direction of current, l (m) is the length of the conductor and ρ (Ω m) is the resistivity of the conductor. A diagram of the layout of a foil strain gauge is shown in Figure 2.4.

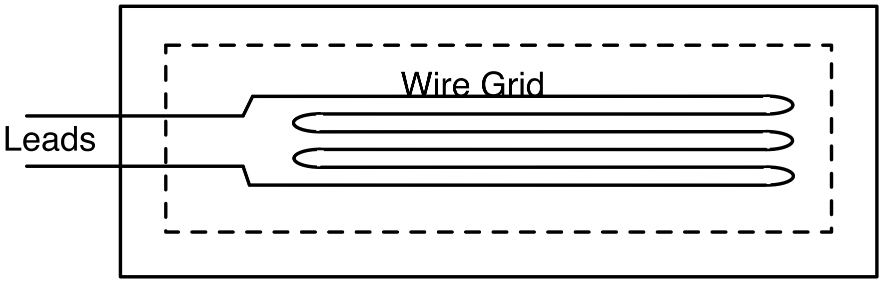

Figure 2.4: Layout of a foil type strain gauge

In the case of a strain gauge under tension the conductor lengthens slightly and the conduction area decreases. The combined effect is to increase the resistance of the gauge. The change in resistance can be measured as a change in voltage across a resistive voltage divider. However it is usual to use more than one gauge. These further gauges can be used to increase the voltage change by being placed in opposition to the first gauge, i.e. when one is in tension the other is in compression. With four gauges, and uni-directional strain, it is possible to de-couple two gauges from the strain so that they change only with temperature thus the measurements are temperature compensated; this is shown in Figure 2.5.

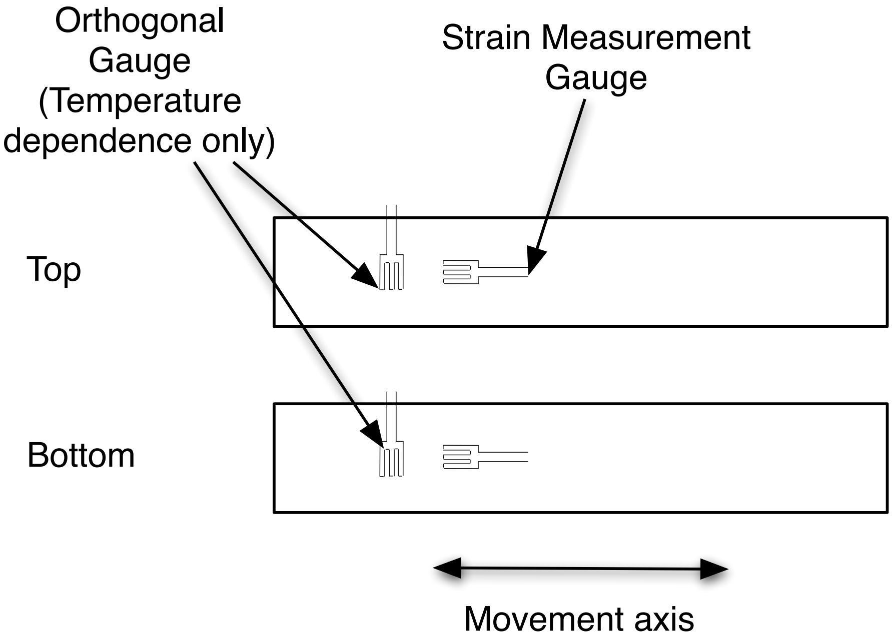

Figure 2.5: Layout of a four gauge measurement set-up; two sensors orthogonal to the strain change direction and thus only subject to change in temperature.

The measurement of the voltage difference using a Wheatstone bridge is shown in Figure 2.6.

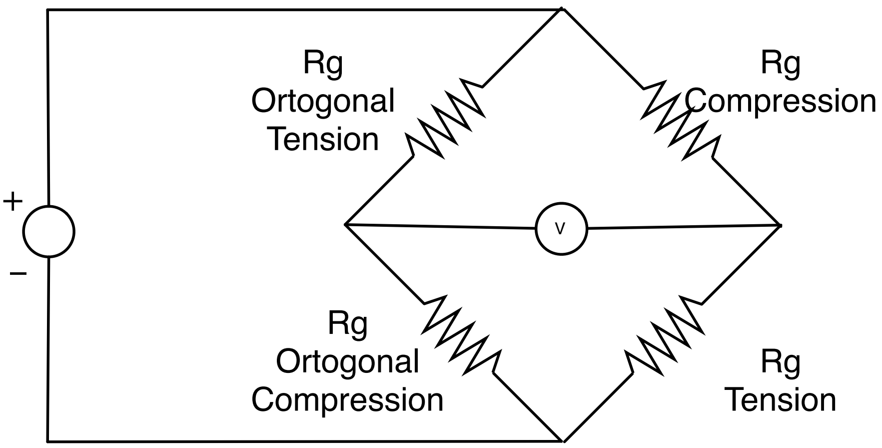

Figure 2.6: Circuit diagram of Wheatstone bridge where any or all Rx could be replaced by strain gauges

2.4 Temperature Measurements

There are a number of different electronic techniques for the measurement of temperature. These include thermocouples, thermistors and resistance measurements. The details of each method including its accuracy and error sources, are detailed below.

2.4.1 Thermocouples

A pair of electrically conductive and thermally dissimilar materials that are coupled together to form an interface is a thermocouple. The legs extending away from this point are known as thermoelements. The Seebeck effect produces a voltage in all such thermoelements where they are not at a uniform temperature. Any electric interface between dissimilar electric conductors is a real thermoelectric junction. The free end of a thermoelement is a terminus, whereas couplings between chemically identical thermoelements are splices or joins.

Seebeck Effect

The e.m.f. is generated through the Seebeck effect only by a process that converts thermal energy to electrical energy. The Seebeck effect is the process by which a net source of e.m.f. is produced between pairs of points on any individual electrically conducting material due to a difference of temperature between them. The Seebeck effect occurs without dissimilar materials. It is not a junction phenomenon, nor is it related to Volta's contact potential.

The absolute Seebeck coefficient is expressed in units of Volt per unit temperature, e.g. $V \cdot K^{-1}$ or, less commonly, $V \cdot {}^{\circ}F^{-1}$. This is the measurement sensitivity of the Seebeck effect. It is defined over any thermoelectrically homogenous region of a slender individual conducting material by

$$\sigma(T) = \lim_{\Delta T_{TC} \to 0} \frac{\Delta E}{\Delta T} = \frac{dE}{dT}, \tag{2.4}$$

or

$$dE = \sigma(T) \cdot dT. \tag{2.5}$$

The Seebeck coefficient is a transport property of all electrically conducting materials [6].

The Peltier and Thomson effects are insignificant as they are current dependent and produce no voltage. Thermo-magneto-electric effects are significant only in the presence of large magnetic fields and infrequently degrade applied thermoelectric thermometry.

Temperature measurements using a thermocouple

It is the thermoelements that determine the sensitivity and calibration of the thermocouple. The net e.m.f. (electromotive force or voltage) observed during thermometry is determined by the temperatures at the end points of the thermoelectric elements, i.e. the ΔT between the thermocouple and the thermoelement termini; both thermoelements are terminated at a thermally stable block.

Table 2.1: These are the operational ranges of the main types of thermocouples and the materials they are constructed with [7]

Thermocouple type	Metal type I	Metal Type II	Temperature Range
B-type	Platinum - rhodium (30%)	Platinum-rhodium (6%)	0 - 1820°C
E-type	Chromel	Constantan	-270 - 400 °C
J-type	Iron	Constantan	-210 - 1200 °C
K-type	Chromel	Alumel	-270 - 1372 °C
N-type	Nicrosil	Nisil	-270 - 1300 °C
R-type	Platinum - rhodium (13%)	Platinum	-50 - 1786°C
S-type	Platinum - rhodium (10%)	Platinum	-50 - 1786°C
T-type	Copper	Constantan	-270 - 400 °C

$$E_{12} = \overline{\sigma}(T_2 - T_1), \tag{2.6}$$

where E_{12} is the voltage generated by the temperature difference between the temperature of the thermocouple at point 1, T_1 and the temperature of the terminal at point 2 T_2, and $\overline{\sigma}$ is the average Seebeck coefficient across the temperature range considered [6].

Thermocouples are available in many different varieties, these are classified in IEC 60584-3:2007 and IPTS 1968 (with relevant cross-referencing by national standards bodies) by a lettering system. The types available and their respective temperature ranges are summarised in Table 2.1 [7] [8].

The tolerances for thermocouples are given by the international standard IEC

Table 2.2: The absolute tolerances of each type of thermocouple all values in °C [9]

Temperature	B type	E type	J type	K type	N type	R type	S type	T type
-200	-	-	-	3.0	3.0	-	-	3.0
-100	-	-	-	2.5	2.5	-	-	1.5
0	-	1.7	1.5	1.5	1.5	1.0	1.0	0.5
200	-	1.7	1.5	1.5	1.5	1.0	1.0	0.8
400	-	2.0	1.6	1.6	1.6	1.0	1.0	-
600	1.5	3.0	2.4	2.4	2.4	1.0	1.0	-
800	2.0	4.0	-	3.2	3.2	1.0	1.0	-
1000	2.5	-	-	4.0	4.0	1.0	1.0	-
1200	3.0	-	-	9.0	9.0	1.3	1.3	-
1400	3.5	-	-	-	-	1.9	1.9	-
1600	4.0	-	-	-	-	2.5	2.5	-

60584-2:1995 [9]. The absolute tolerances are summarised in Table 2.2 for standard operation. The magnitude of the relative tolerance must also be taken into account when designing temperature measurement systems, especially when they are being applied across systems with large temperature changes.

2.5 Reasons for pursuing alternative sensing techniques

The sensing methods and characteristics of a number of different electrical sensors have been described in the preceding sections. The performance of the sensors meeting the functional requirements of a nuclear fusion tokamak port plug environment will now be discussed. Specifically, the radiation environment of the ITER port plug will be defined, followed by the effects of the radiation environment on sensors and cables.

2.5.1 ITER port plug environment

The sensing environment present in an ITER port plug is a challenging one; resulting from the high levels of ionising radiation and elevated temperature [10]. The ionising radiation has two sources, direct radiation from the fusion process and indirect radiation from secondary reactions of the fusion neutrons with the surrounding vessel. These secondary reactions produce gamma rays (γ) along with slower neutrons. It is necessary to consider all components of this radiation field to be able to calculate a total effect on electrical transducers and cabling.

The temperature of a port plug will be 100°C during operation and 240°C during bake out to remove impurities from all surfaces. The heat to bring the port plug to temperature will be provided by circulating 4.4MPa water. If there are issues with the water circulation system it is possible that heat spots could form within the port plug which must be detected to prevent any damage occurring [10].

2.5.2 Ionising Radiation

Before discussing the damage caused by ionising radiation, it is necessary to set out exactly what is meant by ionising radiation. Damage can be caused by ionising radiation to both the central nuclear structure and the surrounding electron cloud e.g. an incident beta particle can cause an outer electron to be ejected from the electron cloud if the incident particle imparts enough energy for the electron to escape the hold of the nucleus.

Ionising radiation comes in various forms, the main ones being alpha particles (He-4 nuclei), beta particles (fast moving electrons), gamma rays (high energy electromagnetic waves) and neutrons at many different energies [11], along with more exotic varieties which will not be considered here. For this thesis only the effects of neutrons and gamma rays are considered because the other particles interact in negligible amounts with the sensor systems.

2.5.3 Nuclear Fusion Reactions

The fusion reactions occurring within the reactor, when burning tritium and deuterium, follow one of many fusion paths; however, only three are of any significance for ITER, these are the deuterium-tritium (D-T) reaction and two types of the deuterium-deuterium (D-D) reaction [11] [12]. These are summarised in Equations 2.7, 2.8 and 2.9 respectively.

$$^{2}H \, + \, ^{3}H \rightarrow \, ^{4}He \, + \, n \, , \, , \tag{2.7}$$

$$^{2}H \, + \, ^{2}H \rightarrow \, ^{3}He \, + \, n \, , \, , \tag{2.8}$$

$$^{2}H \, + \, ^{2}H \rightarrow \, ^{3}He \, + \, p \, , \, , \tag{2.9}$$

where n is a neutron, p is a proton, ^{2}H is a deuterium nucleus, ^{3}H is a tritium nucleus, and $^{3}He/^{4}He$ is a helium nuclei with atomic mass 3/4 respectively.

The D-T reaction is preferred for controlled fusion reactors over either D-D reactions due to its higher energy release [12], 17.6 MeV to 3.3 MeV and 4.0 MeV respectively, and the fact that the Coulomb barrier (electrostatic repulsion between the nuclei) is the same for all of the above reactions.

2.5.4 Thermocouples under ionising radiation

There have been limited studies on the performance of thermocouples under radiation; and are especially limited under fusion levels of irradiation [13] [14] [15]. The effect of radiation on thermocouples and mineral insulated cable has been studied since the 1960‘s for use in fission nuclear reactors. There are a number of electrical effects that result from neutron bombardment. These effects are: radiation induced electromotive force (RIEMF) [16] [17] [18][19], radiation induced conductivity (RIC,) and radiation induced electrical degradation (RIED.) These observed effects are a combination of the nuclear and electrical processes of transmutation and atomic ionisation.

2.5.5 Radiation induced electromotive force

Radiation Induced Electromotive Force, RIEMF, is brought about by nuclear reactions causing the release of electrons in the insulating material of cables. The effect acts like a current source rather than as its name suggests. An empirical formula has been developed for application to a fission environment [16]. The experiments from which this formula is derived were performed in the Japanese Materials Testing Reactor (JMTR). These formulae relate the current to the reactor power with direct proportion, this is because the higher the power the larger the neutron flux and the cable resistance varies with the inverse of the power. The larger the neutron flux, the greater the charge density in the insulating material; resulting in higher current. However, the resistance for MgO cables decreases with increasing neutron flux (due to the charge release). This is related in the formulae below.

$$V_{RIEMF} = RI_{RIEMF} \ , \tag{2.10}$$

$$I_{RIEMF} = aP_{REACTOR} + b_{CURRENT} \ , \tag{2.11}$$

$$\frac{1}{R} = c(P_{REACTOR})^n \ , \tag{2.12}$$

$$\begin{aligned} V_{RIEMF} &= \frac{(aP_{REACTOR} + b)}{cP^n_{REACTOR}} \\ &= \frac{a}{cP^{(n-1)}_{REACTOR}} + \frac{b_{CURRENT}}{cP^n_{REACTOR}}, \end{aligned} \tag{2.13}$$

where V_{RIEMF} is the voltage between sheath and the core of the cable, R is the resistance between the sheath and core of a cable or the resistance between two cores in a dual core cable, a is a constant that relates the current generated in the cable to the power output of the reactor, $b_{CURRENT}$ is the residual current in the wire with no voltage or radiation applied, c is a constant for relating reactor power to resistance of cable, $P_{REACTOR}$ is the thermal power level of a fission reactor used for performing experiments. These formulae are applicable to the neutron environment within a port plug as the neutrons have lost energy by the time they interact with the instrumentation within the port plug. The neutron spectra within the port plug is made up of more thermal and fast neutrons than the plasma.

2.5.6 Radiation induced conductivity

Radiation induced conductivity (RIC) causes signal to noise ratio (SNR) degradation, which changes the accuracy of readings from any given instrumentation. The RIC effect does this by increasing the conductivity of the insulating material of a mineral insulated cable through the excitation of electrons from the insulator‘s valence band to it‘s conduction band [20][21] [22][23][24][25]; this will cause a loss in the cable and the longer the cable the more the signal strength will decrease. At a 14.1MeV neutron flux of 9×10^{15}ns^{-1}m^{-2} the conductivity was 1×10^{-12} S compared to 0.11×10^{-12}S with no irradiation [25]. Their experiments indicate that the RIC can be expressed by an equation of the form,

$$\sigma^{MI}_{RIC} = \sigma^{MI}_0 + K_{RIC} R^d_{RIC}, \tag{2.14}$$

where σ^{MI}_0 is the conductivity with no radiation applied and $K_{RIC} R^d_{RIC}$ is the contribution resulting from RIC. R is the ionization dose rate, and K_{RIC} and d_{RIC} are constants strongly dependent on the material. d is normally in the range of 0.5-1, however, d of 1.6 has been reported. The differing effects of d are illustrated in Figure 2.7. It can be seen that for a difference of 0.5 in d the change in σ can be 10^3. Careful measurements of this effect and good modelling of its influence at different cable positions are therefore required to be able to accurately calibrate cables and transducers used in the ITER environment.

2.5.7 Radiation induced electrical degradation

Radiation induced electrical degradation, RIED, is the permanent enhancement of the conductivity of the mineral insulation due to the change in the composition of the material via transmutation of elements [25] [26][27] under the influence of elevated temperatures and action of an electric field. Nuclear transmutation is the changing of the nucleus of one isotope of an element into the nucleus of another element or isotope via a spontaneous or stimulated nuclear reaction . Such reactions can degrade the purity and structure of a material over time leading to degradation in conduction and insulation. This effect only comes into play at temperatures above

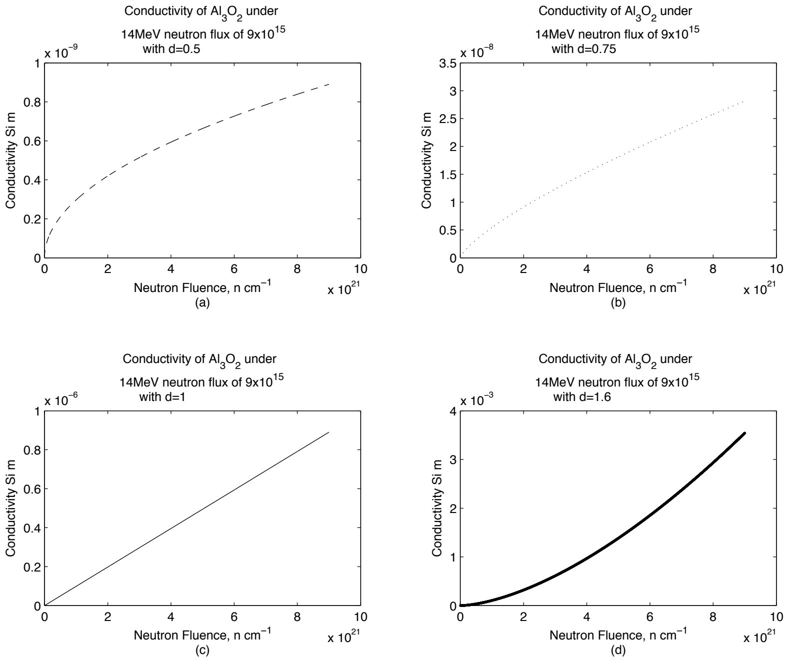

Figure 2.7: Graphs according to Equation 2.14 that illustrate the increase in conductivity with radiation flux, with d= 0.5, 0.75, 1, and 1.6 in (a), (b), (c), and (d), respectively.

300°C for Al_2O_3[14] and higher for MgO. It can therefore be discounted for having any effect within a port plug where the temperature should not exceed 350°C at any time; however it could become significant if the sensors are to be built into the thermal blanket modules where temperatures may reach in excess of 1000°C. Aluminium oxide's threshold fluence is lower than that of magnesium oxide. This is important as it implies that magnesium oxide insulated cables could last longer than aluminium oxide insulated ones. Both types have been considered in nuclear applications as they are suitable for high pressure and vacuum environments, and protect leads somewhat from moisture and thermal shock.

2.5.8 Transmutation and structural changes

Transmutation is the changing of the nuclear structure of an atom from one element or isotope to another [11]. This can occur spontaneously, as happens in radon gas to radium metal or by stimulation by energy carrier bombardment (e.g. neutron, proton, gamma ray etc.) The process of transmutation can be specified by:

$$i + X \longrightarrow j + Y \; , \tag{2.15}$$

where i is an incident particle or photon, X is the nucleus of the original atom, j is the emitted particle or photon and Y is the resultant nucleus. Y may be the same as X or its mass and/or atomic number (number of protons in nucleus) may have changed. Therefore transmutation can degrade the purity of a material over time leading to degradation in conduction and insulation. For example, this effect will cause a thermocouple output to drift under intense radiation as the two metals forming the thermocouple will gradually transmute into different elements. In [14] the application considered is one close to the first wall of the reactor (highest energy neutrons). The thermal and fast neutron fluxes at the first wall are relatively low and therefore will only de-calibrate the thermocouples by less than 2% [15].However the situation inside a port plug is somewhat different, the fast moving neutrons will be slowed (but not stopped) by the water and steel of the port plug, thus the flux of thermal and fast neutrons will have increased. Furthermore [14] asserts that any structural damage will be annealed out by heating to at least 60% of the absolute melting temperature of the material, for Nicrosil-Nisil this is around 700°C, this temperature is far in excess of the maximum bake out temperature (250 °C), and above the maximum permissible temperature (350 °C) for anywhere outside of the vacuum vessel. This leads to the conclusion that any error will accumulate over time.

Transmutation of elements also impacts on the use of strain gauges as these must be attached using an epoxy to the material to be monitored. The epoxy material properties (e.g. Young‘s modulus and elasticity) will change over time with exposure to radiation. In [15] it was found that under proton radiation M40J/AG-80 epoxy‘s bend modulus changed with proton fluence. Initially increasing by 4% then decreasing by 5.8% below initial magnitude at $15 \times 10^{15} pcm^{-2}s^{-1}$. The data available indicates no absolute limit in the change of the epoxy‘s bend modulus under irradiation. Therefore under increasing fluence the measurements performed using the epoxy attached strain gauge will be subject to an unknown error.

2.5.9 Temperature Effects

Along a mineral insulated cable exposed to elevated temperatures (above room temperature) a voltage can be generated. Such a voltage is called a thermally induced electromotive force (TIEMF). These voltages are generated at points along the cable where there is a discrepancy in the metal-insulator interface; such discrepancies can be due to incorrect crystal growth or damage during transport/ installation. It is unclear at this point whether this voltage is generated due to strain built in at manufacturing or due to another effect. Such is the variability in manufacture of mineral insulated cables that when using a reference cable it is difficult to identify the sources of generated voltages and use this information to calibrate sensor measurements. Furthermore it has been demonstrated that the thermoelectric sensitivity of a cable can change over time when exposed to elevated temperatures [14] [28]. Thus heat spots on the cable could increase or decrease voltage generation over time depending on the degree of heating and length of exposure. The thermoelectric sensitivity of a cable can also change with the fluence of ionizing radiation, resulting in the thermally generated voltage evolving over time due to temperature and fluence dependent components [28]. The Seebeck coefficient, α, is a measure of the thermoelectric sensitivity and is defined as the dc voltage generated by a difference in temperature along a cable with no current flowing through it:

$$\alpha = \left(\frac{dV}{dT}\right)_{I=0}, \tag{2.16}$$

where dV is incremental voltage, dT is the incremental temperature and I is the current following in the cable. The total TIEMF voltage generated over a conductor of length l is then,

$$V = \int_l \alpha(x) \frac{dT}{dx}(x)\, dx, \tag{2.17}$$

where x is the direction of the temperature gradient, $dT/dx(x)$is the temperature gradient at position x, l is the distance over which the voltage is being measured, V is the voltage due to a temperature gradient and $\alpha(x)$ is the material dependent Seebeck coefficient. $\alpha(x)$ can vary over the length of the cable. This variation can be due to material purity, and/or manufacturing defects [14].

In the application to the port plugs there are temperature gradients expected over the flange that connects the port plug to the larger holding structure [29]. It is at these points that connections through vacuum seals will be required to be made to link to the external communication circuits.

2.5.10 Electromagnetic Effects

There are a number of plasma disruptions that can cause the plasma to destabilize and collapse. For example vertical displacement events (VDEs) and major disruptions, resulting from long-wavelength non-axisymmetric magnetohydrodynamic (MHD) instabilities [16][30][31]. Both can result in complete quenching of the thermal energy and current of the plasma. These disruptions are highly localised and can dump damaging levels of heat and charge onto a small area of the vessel's walls. During a vertical displacement event (VDE) vertical part of the plasma is inherently unstable and when the divertor-plasma attraction becomes too great the plasma will move, possibly pulling the vessel with it. The plasma will eventually touch the wall for 10 to 20 ms causing currents to flow in a hybrid circuit through the plasma and vessel. Such events occur over a very short time resulting in large time varying magnetic fluxes of order $1Ts^{-1}$. For example during a VDE the rate of change of magnetic flux is 0.9T s-1 in the radial direction and 1.6 Ts^{-1} in the poloidal direction. Such a flux incident on a loop of cable not parallel with the flux change will have a voltage induced on it if the loop is not completely closed; furthermore when connected through the internal impedance of the instrumentation amplifiers the loops will be closed and produce a current. The induced voltage on the signal cables due to changes in magnetic flux can be expressed as

$$V_{induced} = -\frac{\partial B}{\partial t} A \ , \tag{2.18}$$

where B is the magnetic flux density passing through area A, t is time and $V_{induced}$ is the voltage induced by the changing magnetic flux. In the case of a twisted pair cable this would be the area resulting from the imperfect twisting during manufacture and/or during installation. For the purposes of the investigation a cable is assumed to have a total susceptible area equivalent to a circle of 10mm in radius along a length of 3m of twisted pair cable ‘ very probable situation, especially when connectors are considered. There are also a number of dynamic electromagnetic temperature effects including the Nernst-Ettinghasuen effect and the Righi-Leduc effect; these effects are not considered here as their magnitude within a port plug is insignificant. However, when considering applications closer to the first wall [14], for example blanket module monitoring, then electromagnetic effects such as Righi-Leduc and Nernst-Ettinghasuen should be taken into account.

2.6 Measurement Technologies Currently Implemented on Fusion Reactors

The current, largest, nuclear fusion reactor in the world, JET, uses minimal condition monitoring of the super-structure of the reactor; most effort being focused on technologies to interrogate the plasma itself.

The JET restraints [32], or legs, have pairs of strain gauges attached, only a limited amount of information can be found on the JET CODAS (COntrol and Data Acquisition System), this was summarised in [33].

In [33] a fibre optic strain measurement system is proposed and tested on the struts of the JET vessel. This fibre Bragg grating based system was used to measure the dynamic strain, and was not corrected for temperature fluctuations.

On the UKAEA's MAST (MegaAmpere Spherical Tokamak) reactor there are a number of thermocouples installed on the current carrying conductors that wrap around the reactor. These are necessary due to the large currents (of order 10^4 A flowing in these conductors and thus a large amount of heat is generated, of order 10^3 W when operating at 4.6×10^3 A of current[1].

---

[1] Own order of magnitude calculations

2.7 Scenarios

For this thesis only locations within the Port Plug(s) of the ITER are of concern. The monitoring of mirrors and the structures that hold them within the diagnostic channels of the port plug will be necessary. Sensors located on the sides of the port plug can be considered simultaneously. However, the top, bottom, front and rear panels must be considered separately as the incident radiation, heating, and EMI are different for each surface.

Within the port plug, as previously mentioned, there is sensitive optical equipment such as mirrors and lenses. These also require monitoring to make sure that they have not been exposed to more heat or radiation than they were designed for. The ITER conditions will place stresses on them that may cause them to bend or contort, therefore stress/strain monitoring is necessary. Within the port plug LIDAR (Light Detection and Ranging) system there the a first mirror that has a line of sight directly into the reactor; thus are exposed to higher radiation flux than the second and third mirrors. They will also be subject to a greater heat and particle flux ($\mathrm{He}^{+2}, \mathrm{D}^{+1}, \mathrm{T}^{+1}$) then equipment placed further inside the port plug.

What follows is a treatment of the locations within the port plug where sensors could be placed. The thermocouple probes are taken to be of generic shape such as in Figure 2.8, covered with a dielectric for insulation and a metal cover.

A possible layout of sensors, cables and conduits is shown in Figure 2.9.

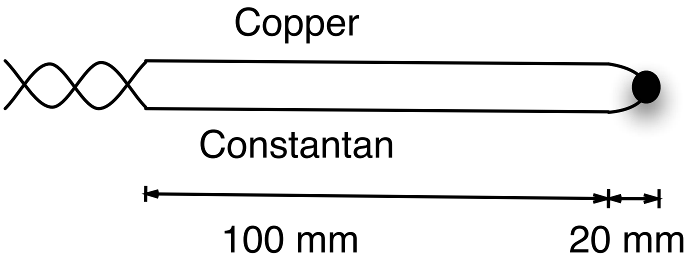

Figure 2.8: The basic layout of a thermocouple probe.

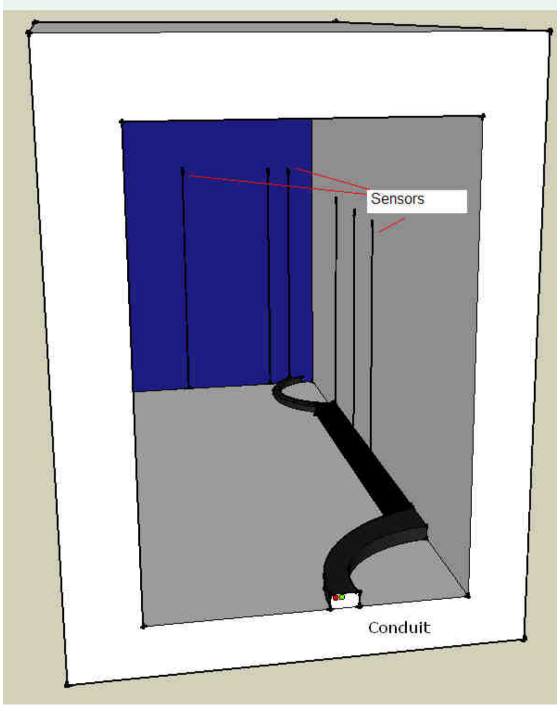

Figure 2.9: View towards plasma end of port plug (blue) with indications of possible sensor positions and conduits.

The induced e.m.f calculations are made under the following assumptions:

- the poloidal flux change during a Vertical Displacement Event (VDE) is 1.6T s^{-1}
- the radial flux change during a VDE is 0.9 T s^{-1}
- the total susceptible area coming from the sensor and it's associated leads is a circular loop of radius 10 mm which equates to 314 mm^2
- of this 314mm^2, 20% is contributed from the sensor.

- the area available for magnetic flux induced e.m.f along the twisted pair cable, i.e. that which is not cancelled, is 47 $\mathrm{mm}^2\,\mathrm{m}^{-1}$ (total cable length is 5.3 m)
- transmutation of a thermocouple can introduce an error of 1% after a fluence of $10^{21}\mathrm{n\,cm}^{-2}$of neutron irradiation
- Voltages generated during irradiation are
    - under 15 $\mathrm{kGy\,h}^{-1}$ (4.2 $\mathrm{Gy\,s}^{-1}$) of gamma irradiation RIEMF in steel core cables can be a few nanoVolts. See section 2.5.5
    - under 10 $\mathrm{Gy\,s}^{-1}$ of gamma radiation RIEMF in copper core/ magnesium oxide insulated cables was less than 20 nV. See section 2.5.5
- Thermally induced e.m.f (see section 2.5.9)
    - at 305°C the e.m.f generated in steel and copper core cables can be as much as 2 μV
    - at 305°C the e.m.f generated in nickel core cable can be as much as 50 μV
- Thermoelectric sensitivity
    - The thermal sensitivity of copper changes with the flux of incident neutron radiation [34]; The Seebeck coefficient changed at a rate of $10^{-21}\,\mu V^{\circ}\,\mathrm{C}^{-1}\,(\mathrm{n\,cm}^{-2})^{-1}$ rising to 0.27 $\mu\mathrm{V}^{\circ}\mathrm{C}^{-1}$
    - The thermal sensitivity of steel core cable changes with the temperature on it; The Seebeck coefficient saturated at 0.13 $\mu\mathrm{V}^{\circ}\mathrm{C}^{-1}$ after a fluence of $5 \cdot 10^{19}\mathrm{n\,cm}^{-2}$.
- the thermocouple generated voltages, from [7], are
    - type K
        - at 100°C $\mathrm{V} =$ 4.096 mV
        - at 220°C $\mathrm{V} =$ 8.940 mV
    - type N
        - at 100°C $\mathrm{V_O}$ = 2.774 mV
        - at 220°C $\mathrm{V_O}$ = 6.579 mV

- the voltage outputs from a standard strain gauge at $100\mu\epsilon$ and $1000\mu\epsilon$ are
  - for $100\mu\epsilon$ $V_O = 416\mu$V
  - for $1000\mu\epsilon$ $V_O = 4160\,\mu$V

The rear panel noise sources will be detailed in the following section with the other locations summarised in tables and figures in section A.1.

2.7.1 Rear Panel

The rear of the port plug is furthest away from the plasma. This means that the nuclear heating averages 0.1 $\mathrm{MWm^{-3}}$. However, there are empty space channels through the port plug along which neutrons can pass, this could lead to hot spots on the rear wall and internal surfaces. Furthermore, localised interference will be induced on the cables at these hot spots. This means extremely accurate calculations are required to model the induced voltages at these points.

In this scenario the sensor is placed on the floor of the port plug, as in Figure 2.10. The dimensions are 1.7m vertically down from the instrumentation interface, and 2.5m in the horizontal direction.

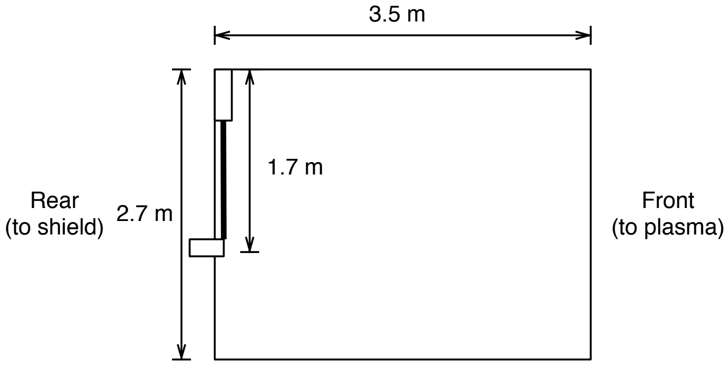

Figure 2.10: Side view of port plug rear face sensor and connection (strain gauge or thermocouple)

top

Radiation Effects

The neutron radiation fluence will cause the transmutation of the thermocouple over time and introduce an error of around 1%. The RIEMF and TIEMF induced on the rear panel connections will be approximately $10\,\mu$V. The RIEMF introduces an error of around 0.3% during a deuterium-tritium pulse, this was shown by experiment in [15].

EMI

With the strain gauges or thermocouples placed on the rear panel the sensor and cabling will be orthogonal to the radial magnetic field. This field is expected to change at a rate of $0.9\ \ \mathrm{T\,s^{-1}}$in a plasma disruption. The cabling that travels up from the port access point is exposed to the radially changing field taken at a rate of $0.9\ \ \mathrm{T\,s^{-1}}$. The induced e.m.f is

$$\varepsilon_{sensor} = -\frac{dB}{dt}A_{sensor} = -(-0.9)\cdot 63\times 10^{-6} = 57\mu\mathrm{V} \tag{2.19}$$

where A_{sensor} is the area (in m^2) of the sensor.

$$\varepsilon_{vert} = -\frac{dB}{dt}A_{tp} = -(-0.9)\cdot 160\times 10^{-6} = 72\mu\mathrm{V} \tag{2.20}$$

where A_{tp} is the area resulting from errors in the twisting of the cable.

$$\varepsilon_{total} = \varepsilon_{sensor} + \varepsilon_{hor} + \varepsilon_{vert} = 130\mu\mathrm{V} \tag{2.21}$$

Thus for the described system an e.m.f of 130μV would be induced on the sensor signal during a Vertical Displacement Event (VDE).

Total Error

During a normal deuterium-tritium pulse the noise signals will be dominated by the RIEMF and TIEMF; the induced e.m.f. will be approximately 10μ V on this transducer/ connection system. This results in an absolute error of 0.2% at 100°C for a K-type thermocouple and 0.36% for an N-type thermocouple at 100°C.

In addition an error of approximately 1% can be expected due to transmutation of the atoms within the thermocouple.

During a Vertical Displacement Event, the noise signals on the thermocouple and strain gauge cables are dominated by EMI. This induced voltage is approximately $130\mu V$ during a VDE, based on the above assumptions of cable length, and susceptibility.

$$T^{EMI}_{error_N} = \frac{0.130}{4.096} = 0.032 \tag{2.22}$$

$$T^{EMI}_{error_K} = \frac{(}{0}.1302.7747 = 0.047 \tag{2.23}$$

Thus for the K- and N-type thermocouples at 100°C the errors due to EMI (dominating) are (to 1 significant figure) ±3 °C and ±5°C respectively.

$$T^{EMI}_{error_{100}} = \frac{0.130}{0.416} = 0.312 \tag{2.24}$$

$$T^{EMI}_{error_{1000}} = \frac{(}{0}.1304.160 = 0.0312 \tag{2.25}$$

Thus the errors in the defined strain gauge at $100\mu\varepsilon$ and $1000\mu\varepsilon$ are approximately 30% and 3% respectively during a VDE (dominated by the EMI effect).

2.8 Summary

It is obvious from the literature that there is a lack of condition monitoring of fusion reactor systems currently. In the future with higher power, and longer running, experimental and commercial fusion reactors it will be necessary to develop full reactor condition monitoring systems. This is because the fusion environment is highly toxic and damaging to materials and components placed in and around the fusion chamber[35].This thesis will propose a system that can be used throughout the fusion reactor inside the bio-shield, but outside the fusion chamber.

This chapter has explained the following

- a number of different electrical methods for the measurement of strain,
- the difficulties integrating these strain measurement methods into a fusion reactor,
- several methods for the measurement of temperature,
- the limitations and drawbacks of the thermocouple, thermistor and resistance type measurements,
- the fusion reactor environment - temperature, pressure, radiation,
- a set of studies of the different possible positions for sensors,
- the effects of radiation on electrical sensors.

The following were calculated in this thesis:

- the lengths of cables to be used within the port plugs for particular sensor positions,
- the area of cable that would be available for magnetic flux to move through that would not be cancelled out by another loop,

- the errors in the measurement of strain and temperature resulting from the EMI generated during a vertical displacement event,
- the errors due to radiation within the port plug were calculated.

Chapter 3

Optical Sensing Methods and Metal Embedding Theory

3.1 Introduction

In this chapter the possible applications of fibre optic sensors within a nuclear environment are identified, the operating principles of fibre Bragg gratings (FBGs) and Fabry-Pérot interferometers as optical sensors will be described. This is followed by a description of the effects of the environment close to a nuclear fusion reactor on the sensors in terms of de-calibration and mechanical effects. This chapter also includes a review of methods to coat the fibre in various types of metal and also techniques to embed the fibre within a metal substrate.

3.1.1 Application of optical fibre sensors within nuclear fusion environments

There are numerous applications for optical fibre sensors (OFSs) within and around current and future nuclear fusion reactors. For example FBGs have been deployed to measure the force on the legs/ supports of the JET reactor during disruption event [36]. These sensors have much higher resolution than the currently installed legacy strain gauges. A further application of fibre sensors could be to monitor the magnetic field and temperature at points in and around the reaction vessel. This has traditionally been performed using coils of wire, but could be now performed using optical fibre sensors [37]. The superconducting magnetic coils of a tokamak fusion reactor are also a place where it has been envisaged and demonstrated that optical fibre sensors could be deployed to monitor multiple parameters [38]. With the realisation of the flexibility of fibre optic sensors it is likely that many more applications will be recognised and solutions deployed in nuclear fusion reactors.

3.1.2 Application of optical fibre sensors to monitoring within nuclear fission reactors

Fibre optic sensors have been identified both in Europe and the USA as a useful technology for the condition monitoring of nuclear power plants [39][40]. Fibre optic sensors in fission reactors can be used to work out where they could also be applicable within the nuclear fusion environment. For example both types of reactors have containment structures made of concrete which require regular inspections to check for any defects; however by embedding fibre optics sensors into the reinforced concrete the number of inspections could be reduced on the basis of a continuous monitoring system able to detect changes in the structure.

In [41] the application of optical fibre sensors to the nuclear power plant (NPP) industry (fission) is discussed and sets of results from different sensors are presented. The article highlights the monitoring of the structure using FBGs embedded in the concrete inside steel tubes to test the tensive response or attached to the outside of concrete cylinders to test the compressive response. The paper [42] highlights that where fission radiation is concerned, that the effect of gamma and neutron radiation induced attenuation is minimal in the $1.3\mu m$ and $1.5\mu m$ regions of the spectrum . Further if pure silica core fibres were used then the effect can be removed by some temperature cycling. The effect of dose and dose-rate is examined in [43] and it can be shown that the effect of dose on radiation induced attenuation (RIA) dominates at low dose rates (normal operation) and at higher dose rates (especially with temperature at or above 100°C)

Optical fibre sensors could also be used in the NPP to detect cracks on high temperature water carrying pipes since a crack will cause the local temperature to increase significantly. By attaching fibre sensors to the exterior of the pipe's insulation this temperature increase could be detected early and remedying actions taken. There are two main methods of doing this with optical sensors, using Raman or Brillouin scattering to monitor the temperature all along the fibre or using multiplexed point sensors such as the FBGs. Although full monitoring of the pipe would be desirable it would result in massive amounts of generated data that would need to be archived; by carefully selecting the locations of FBGs along the pipe on the basis of the most probable locations of cracks such as joints and elbows then 95% of all pipe failures could be detected [41]. Thus the use of FBGs is more desirable for the monitoring of pipes in an NPP.

A further application of optical fibre sensors (although not FBGs in their current form) is the detection of gases within the atmosphere of the NPP. For instance the build up of hydrogen gas creates the potential for an explosion to occur [44]. The use of a fibre optic sensor as opposed to an electric sensor decreases the likelihood of ignition of the hydrogen build up and removes the requirement for power sources within the containment shield.

3.2 FBGs

The application of optical measurements and, in-particular, optical fibre systems to sensing applications is a relatively new field. There are still many areas in which they could be exploited.

Optical sensors have been deployed to measure a number of physical phenomena [45], including temperature, strain, magnetic field strength, electric current and pressure; this is not an exhaustive list as research into new methods is currently on-going.

An optical sensor is considered in this thesis to be any optical device (in the infra-red, visible and ultraviolet wavelength bands) that is affected by an exterior effect, e.g. change in temperature or pressure, such that the change induces a quantitative and measurable change in an optical measurand. Examples of optical measurands are wavelength (frequency), intensity, polarisation and phase. There are a number of different optical sensors each exploiting a different physical phenomenon.

This thesis is concerned with the embedding of a sub-type of FBG into a thin slab of metal. Then for it to be used to measure strain and temperature simultaneously. Here the FBG will be described in technical detail.

3.2.1 Grating Structure

FBGs are most often described as a periodic variation in the refractive index of the core of the fibre that has been induced by some controllable external effect. The underlying physical mechanism of an FBG is Fresnel reflection. A recent, and detailed, review of the manufacture and properties of different types of FBGs is given in [46].

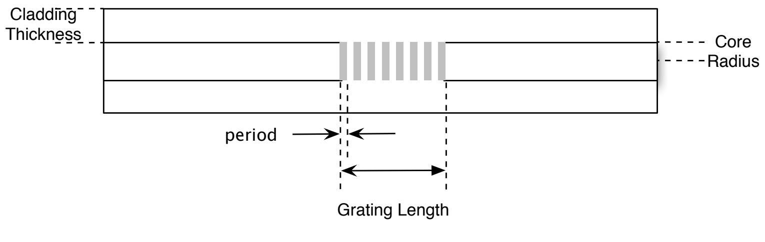

Figure 3.1: Refractive index layer structure of FBG

In Figure 3.1 is shown diagrammatically, and not to scale, the structure of a standard FBG. In the real structure the core is much smaller than the surrounding cladding material and the period is also much smaller with many periods to make up one grating (approximately 10000) [46]. The reflected wavelength from an FBG is set by the effective refractive index and the periodicity of the refractive index changes. The effective refractive index, n_{eff} is calculated by,

$$n_{eff} = \frac{n_1 + n_2}{2} \; , \tag{3.1}$$

where n_1 is the refractive index of the unaltered core and n_2 is the refractive index of the altered core. The reflected Bragg wavelength, λ_B is calculated by

$$\lambda_B = n_{eff}\Lambda \; , \tag{3.2}$$

where Λ is the period of the refractive index change. The reflection profile, from coupled mode theory, is given by

$$R(Lgr, \lambda) = tanh^2(\frac{\pi \Delta n L_{gr}}{\lambda}\eta) \; , \tag{3.3}$$

where L_{gr} is the grating length, λ is the reflected wavelength, η is the overlap between the fundamental mode and core, and Δn is the difference between the core and cladding refractive indices. η is typically between 0.8 and 0.9. Δn is typically between 0.001 and 0.01. The spectral full-width at half-maximum (FWHM) of the grating is given by,

$$\Delta\lambda_{FWHM} = \lambda_B s \sqrt{\frac{\Delta n}{2n_{eff}}^{2} + (\frac{1}{N})^2} \; , \tag{3.4}$$

where $\Delta\lambda_{FWHM}$ is the full width half-maximum of the grating's optical power, λ_B is the Bragg wavelength, δn is the difference in refractive index between the affected and unaffected periods, N is the number of periods and n_{eff} is the effective refractive index of the grating. The change in λ_B due to a change in temperature is calculated by,

$$\Delta\lambda_B = K_T \Delta T \; , \tag{3.5}$$

where $\Delta\lambda_B$ is the change in λ_B due to a temperature change, ΔT is the change in temperature, and K_T originates from,

$$K_T = \lambda_B(\alpha + \zeta) \; , \tag{3.6}$$

where α is the thermal expansion coefficient and ζ is the thermo-optic coefficient; these are both physical properties of the material used. α originates from the expansion of the material due to applied heat and varies with temperature. ζ relates the change in temperature to a change in refractive index.

The change in λ_B due to a change in strain is calculated by,

$$\Delta\lambda_{B\epsilon} = \lambda_{B0}(1 - p_\alpha)\Delta\epsilon \ , \tag{3.7}$$

where $\Delta\lambda_{B\epsilon}$ is the change in λ_B due to the change in applied strain, $\Delta\epsilon$ is the change in applied linear strain and p_α is given by,

$$p_\alpha = \frac{n_{eff}^2}{2}[p_{12} - \nu(p_{11} - \rho_{12})] \ , \tag{3.8}$$

where n_{eff} is as before, ν is Poisson's ratio of the material, and ρ_{12}, ρ_{11} are components of the fibre optic strain tensor.

An FBG can be effectively modelled as a series of thin film layers built upon each other. This is described in detail in [47]. From this theory a simple computer program was constructed in MATLAB© that calculates the reflectivity pattern of gratings with different changes in refractive index. Some examples of these reflection patterns are shown below. With further development it is possible to demonstrate the patterns for multiple gratings written at the same spatial position on the fibre.

3.2.2 Refractive Index Dependence on Density

The refractive index of silica glass is dependent on the density of the glass; the density can change due to the effects of ionising radiation on compaction,

$$\frac{n^2 - 1}{n^2 + 2} = \frac{4\pi}{3} N_m \alpha_p \ , \tag{3.9}$$

where n is the refractive index of the silica, N_m is the number of molecules per unit volume and α_p is the molecular polarizability. This relationship is known as the Lorentz-Lorenz equation[48].

This can be expressed in terms of mass density by using the relationship between density ρ_d in $\mathrm{kg\,m^{-3}}$ and N in molecules per m^3.

$$\rho = m_m \cdot \frac{N}{N_a} \ , \tag{3.10}$$

where N_a is Avogadro's number 6.02×10^{23} [49]and m_m is the molar mass of the molecule (in kg) under consideration; in this case silica SiO_2, molecular mass of

60.0843 kg/mol. Thus combining equations (3.9) (3.10) it is possible to describe the dependence of the refractive index of silica on its density, as shown in Equation 3.11 below,

$$n^2 = -\frac{2\rho_d + C_0}{\rho_d - K_0} , \tag{3.11}$$

where C_0 is considered a constant and defined by

$$C_0 = \frac{3}{4\pi}\frac{m_m}{N_a\alpha} , \tag{3.12}$$

where the variables are as defined previously.

With equation 3.11 it is thus possible to calculate the change in refractive index with changes in density due to external influences, for instance with radiation dose.

3.2.3 Grating classification by growth characteristics

The scheme of classification by growth characteristics is used to categorise gratings by the growth behaviour of the grating during inscription. Mainly short period gratings are described by this scheme. FBGs can be categorised into different types 0, I, II, IIa; each type can be described by its reflection coefficient and reflection shape. These are outlined below.

The general method of making an FBG is to illuminate the core of the fibre with an intense ultraviolet laser fringe pattern. This 'inscribes' or 'writes' a periodic (or aperiodic) variation of the refractive index. Different core doping elements can be used depending on the desired FBG characteristics [50].

Type 0 Gratings

These are also known as *Hill* gratings; they are formed by the interference pattern created from launched light reflecting off the cleaved end of a fibre. As the grating forms further light is reflected thus increasing the power of the grating. The wavelength of these types of grating is, however, dependent on the wavelength of light used to inscribe; thus only gratings in the ultra-violet region can be formed as only these wavelengths can affect the refractive index of the fibre in this manner.

Type I Gratings

These common gratings exhibit a monotonous growth pattern.These are mainly written in germanosilicate fibres and are stable to $\sim$ 320°C.

Type II Gratings

These are created by high power single-pulse shots of UV light. The pulse causes a damage pattern mainly on the core-cladding interface. The gratings exhibit high losses on the short wavelength side of the Bragg wavelength (*red end*) [51].

Type IIa Gratings

This type of grating's reflection strength grows initially like a type I grating and then decreases before growing again. They are sometimes referred to as negative index gratings; however, it is likely that the gratings contain two components, a positive index grating (type I) and a negative index grating [52].

Chemical Composition Gratings

These gratings are not a clear subset of any of the previously described grating types and as such must be considered separately. Although the optical properties of the finished grating are the same as type I and type IIa, the manufacturing procedure, growth characteristics and thermal properties vary significantly. The refractive index modulation is ascribed to a periodic variation of one or more dopants in the core.

This particular type of grating is formed by a periodic variation in the concentration of a chemical within the fibre's structure. These gratings were developed in Sweden [53]. The process for grating formation was summarised in [54]. A fluorine co-doped germanium singlemode fibre is hydrogenated in a high pressure hydrogen environment. On to this hydrogenated fibre is written a traditional Bragg grating by exposure to a UV fringe pattern. Hydroxyl groups are then formed in those regions exposed to UV only through a UV assisted photo-chemical reaction. This creates a type I grating and also a periodic variation in the concentration of hydroxyl groups that matches the periodicity of the grating. The final stage is to slowly heat the grating up to 1000°C which erases the type I grating. Continuing in the thermal treatment results in the complete formation of a thermally stable chemical composition grating.

3.2.4 Interrogation of an FBG

The reflected wavelength from the FBG must be detected in some repeatable manner to enable the use of the FBG as a sensor. This is most often done by launching light from a broadband light source, such as a super-luminescent diode,and coupling the light via 50/50 coupler to a fibre optic line containing one or more FBGs.

The FBG reflects a wavelength based on the local conditions it is experiencing, given its small size it can be considered a point sensor. This reflected wave is coupled down another line (shown as 3 in Figure 3.2) at the end of which there is a wavelength discrimination system. The discrimination system could be a tuneable optical filter or an arrayed waveguide.

3.2.5 Environmental Effects on FBGs

In this section the effect of high temperatures and ionising radiation on FBGs will be explored.

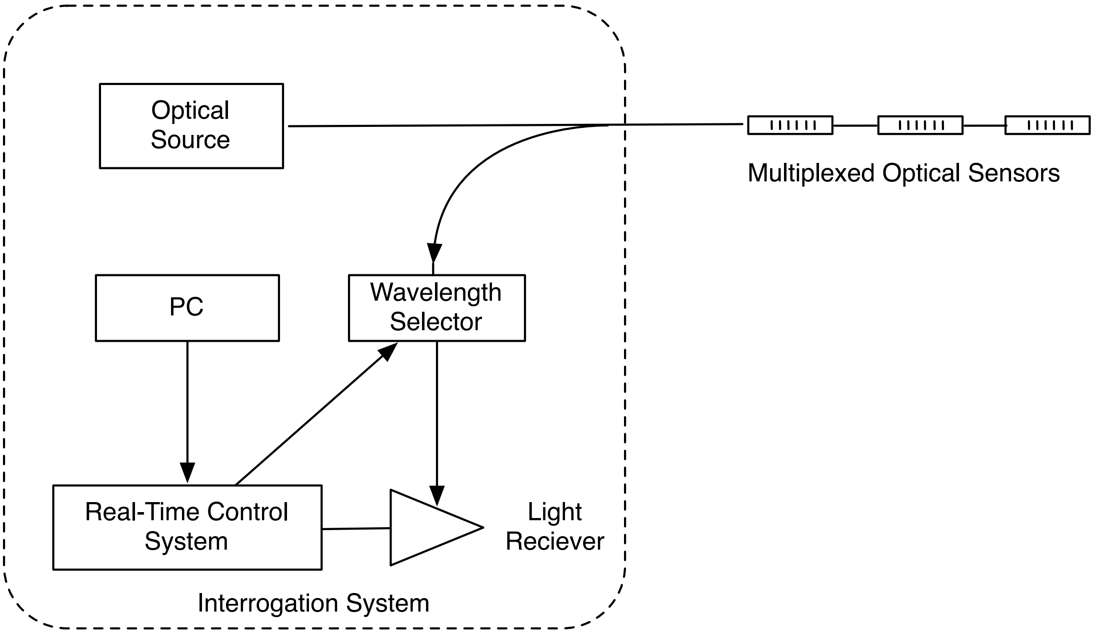

Figure 3.2: Interrogation of an optical sensor's reflected signal

High Temperatures

When considering temperature effects on FBGs it is necessary to consider long-term tests of gratings subject to temperatures above 300°C (573 K). In [55] a grating written in tin-doped silica fibres using a UV excimer laser is shown to be stable for a long term (estimated at 10 years) at up to 550 K (277°C) and transiently (up to 50 minutes) stable to 1100 K (827°C). This grating does satisfy the need for long term stability at 300°C and even up to 400°C. It is stable for at least 10 years at high temperatures. This has been modelled by considering the change in normalised integrated coupling constant (η) with time and temperature. This is defined as,

$$\eta = \frac{\Delta n_{mod}(t)}{\Delta n_{mod}(0)} , \tag{3.13}$$

where $\Delta n_{mod}(0)$ is the refractive index modulation at time = 0 and $\Delta n_{mod}(t)$ is the refractive index modulation at time = t.

The time-dependence of η is well approximated by a power-law dependence,

$$\eta = \frac{1}{1 + Bt_{ic}^{\epsilon}} , \tag{3.14}$$

where $B = B_{0a}e^{bT}$ and $\epsilon = T/T_{0a}$ where B_0, b, and T_{0a} are material specific constants. Using these equations and the data in [55] it is possible to model a tin-doped FBG sensor and these models were used and the graphs created and shown in Figure 3.3 and Figure 3.4. However it has not been proven in a nuclear environment and it is not commercially available, thus this grating type will not be considered further.

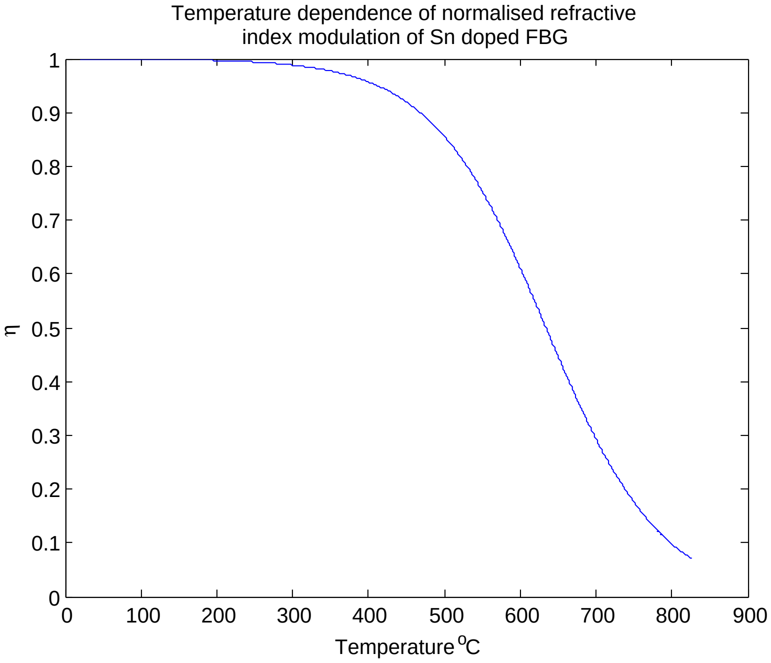

Figure 3.3: Change in normalised refractive index due to temperature change of a tin doped FBG

A set of commercially available FBGs were tested under high temperatures (up to 1000°C) for hundreds of hours [56]. This was part of a programme to understand the usability of FBGs within aerospace applications. It was demonstrated that at over 750°C an oxygen-CCG peak forms and that this can be calibrated for the making of temperature measurements. Further it was demonstrated that FBGs are capable of being cycled up to 1000°C multiple times without loss of accuracy. [56] demonstrates that the use of the FBGs for making accurate measurements within a high temperature environment such as ITER is possible.

A chemical composition type grating that uses erbium as the periodic doping agent is proposed and demonstrated in [57]. These gratings were formed similarly to the CCGs of [53] but may not suffer from rapid degradation above 1000°C that has been associated with the out-diffusion of fluorine. The FBGs were cycled to 800°C and their response fitted to a second order polynomial. Dual wavelength operation of the erbium doped gratings was not demonstrated, and this is required for de-convoluting strain and temperature under this system of operation. Further rare-earth dopants have unknown responses within radiative environments.

A comparison of type I and type IIA FBGs with CCGs was made in [58]. The gratings were exposed to high temperatures for more than 600 hrs each. They demonstrated that CCG type gratings will last longer at higher temperatures than those written in B-Ge co-doped and Ge-doped fibres. The Ge-doped grating reflected until the oven reached 750°C at which point the grating was erased. The CCG was able to reach 1100°C before it began to degrade. This again demonstrates that the CCGs are a viable solution for high temperature environments.

Radiation and Optical Fibre Sensors

This section starts by describing the generic effects that ionising radiation found in a tokamak support system could have on silica. It is widely accepted that neutron and gamma radiation with energies greater than 1 MeV can cause atomic displacement and bond breaking within a silica network [59]. This results in various radiation related defects being being induced in the fibre.

In [60] it is shown that hydrogen loading of optical fibres causes the decrease in transmission (or the increased absorption) of light in the 1300-1500 nm range once given 1MGy of gamma dose and under the neutron fluence of $10^15\,\mathrm{n\,cm^{-2}}$. Though this work does show that the effect of hydrogen loading is to reduce Radiation Induced Attenuation (RIA) in the visible end;, that is not relevant for this work to consider hydrogen loaded fibres for the creation of a sensor for working in a nuclear fusion reactor.

The effects of ionising radiation on silica in the visible wavelength domain has been closely studied and described [61, 62, 63, 64, 65, 66]

In [67] it is shown that acrylate fibre coatings that contain hydrogen increase the total dose received by the fibre from 14 MeV neutrons. This is because recoil protons are created in the coating by the interaction of the 14 MeV with the acrylate. These cause further damage in the fibre core. Further they show that gamma irradiation experiments on optical fibre performance cannot be easily substituted for high energy neutron ones. This is demonstrated through experiments which show that the radiation induced loss from equivalent fluences of gamma ray irradiation and 14 MeV neutron irradiation is 2.5 times higher in the neutron irradiation case. This relationship holds to at least 3×10^{12} cm^{-2} with the ratio decreasing to two above 3×10^{13} cm^{-2}. This is important for the comparison of different irradiation experiments on optical fibres.

[68] considered the effects of gamma radiation exposure on three different types of optical sensor, semiconductor absorption temperature sensors, multimode extrinsic Fabry-Perot cavity sensors and FBGs of differing types. Semiconductor absorption temperature sensors are outside the scope of this thesis due to their operating limits being below the outline requirements. The Fabry-Perot cavity sensor is shown to be highly dependent on radiation exposure and will not be considered further in this thesis. The different types of FBG gave dissimilar results; however they show that, the temperature sensitivity of the FBGs is not affected within 3% (accuracy limit); the peak shape, in terms of amplitude and FWHM is unaffected under γ irradiation and further that a peak position change no greater than 25 pm is observed under 1 MGy of gamma irradiation.

Nitrogen doped fibre sensors were considered for nuclear reactor operation in [69]. Nitrogen doped fibres were shown to exhibit higher resistance to gamma irradiation than germanium doped ones, 0.025 nm change in peak position for N-doped compared to over 0.175 nm change for Ge-doped fibres after 0.1MGy of gamma ray exposure. Further the spectral width of the reflected spectrum from a N-doped sensor does not change unlike that from an Ge-doped fibre. This indicates that for temperature measurements under gamma irradiation it would be best to use N-doped type IIa fibres. However, this set of tests was only performed over 55 hours to a maximum gamma dose of 1 MGy and longer term tests would be required to prove their usability.

[70] experimentally tested four FBGs, manufactured in four different ways, in

the low flux irradiation channel of the BR1 test reactor at SCK.CEN in Belgium. The gratings were exposed to a total of neutron dose of 9.9×10^{17}n cm^{-2} and total gamma ray dose of 3.8 MGy. The neutron energy profile is not representative of that found in the port plugs of ITER; however, it does give an indication of the effects that could occur. [70] found that after four years of operation the grating with best radiation resistance was that written using a pulsed 248nm (UV) source. This grating saturated at 0.4nm longer than its starting wavelength under the same measurement conditions (temperature, pressure and strain). This indicates that FBGs can be used in environments with neutron and gamma irradiation present.

Fluorine (F) and oxyhydrate (OH) core doped optical fibres were tested in the JMTR [71]. These tests indicated that OH doped fibres exhibit less radiation induced attenuation in the infrared wavelengths and that F-doped fibres have less radiation induced attenuation in the visible wavelengths range. The fluorine doped fibres also have a small working bend ratio due to the small difference in refractive index between the core and cladding.

Three different types of optical fibre sensors were tested under gamma irradiation to 1MGy in [72] and [68]. One of the sensor types was the FBG; the papers considered the effect of gamma irradiation on gratings made with different magnitudes of UV pulses. It was found that the shape of the FBG reflection shape was not affected in terms of amplitude and width. Further it was found that the Bragg wavelength change due to irradiation is not higher than 25 pm and saturates at a total dose of 0.1 MGy. Additionally no change in the temperature sensitivity coefficient (α) was found within 3% (the accuracy of the measurements). This paper shows that gamma irradiation can be corrected for if the effect on the proposed FBGs can be found in advance by testing. In [73] FBGs written in 12 different types of optical fibre were studied under gamma irradiation from a Co-60 source. All but one fibre contained some amount of GeO_2 in the core of the fibre, ranging in levels of less than 0.1 mol% to 20.1 mol%. The other dopants were phosphorus oxide, boron, fluorine, titanium, aluminium oxide, and cerium oxide. Cerium dioxide was shown to increase the RIA of the fibres, even though CeO_2 is known to decrease RIA when used as a hot cell window [74]; however here it is found that it increases the RIA in the core at relatively low doses. A further paper by Henschel *et al*, [75], describes the effects of gamma radiation on two types of FBG, one written using femtosecond infrared light and the other with UV laser light. They show that the Type I fs IR grating written in radiation hard fibre has a better long term peak drift of only 5pm after 1MGy of gamma irradiation. However the tensile stress sensitivity of the grating decreased by ∼4% during the irradiation. This means that further grating development is required to create a highly accurate temperature and strain sensor with this type of FBG.

Table 3.1: Summary of radiation effects on different fibres from the literature

Grating Type	Dosage	Effect	Source
1550nm in 10 mol% GeO_2 Refl.3.6 to 4.2 dB Hydrogen loaded at 12MPa, 100°C	55kGy Co-60 source	$\Delta\lambda_B$ equal to 6°C change no indication of stablising	[76]
1550nm in 10 mol% GeO_2 Refl. 2.4 to 4.2 dB	$\sim 10^{10}$n cm^{-2}	Saturated movement of the Bragg wavelength Stabilised after 5 days exposure	[76]
1546nm in Ge-doped fibre	gamma: 1.5MGy	0.015nm blue [1] peak shift	[77]
1546nm in N_2-doped fibre	gamma: 1.5MGy gamma	0.055nm blue peak shift [2]	[77]
$\tilde{1}$550nm CCG	n: 1.310×10^{19}n cm^{-2} gamma: 290MGy after 50h	>10nm λ_B shift >0.21nm FWHM incr.	[78]
Arc-induced LPFG	gamma: 0.5MGy	No changes in wavelength, thermal or strain coeff.	[79]
$\sim 1546nm$ 10% mol. GeO_2	$> 1MGy$ at 3 kGy/h over 15 days	$\Delta\lambda_B$ increases upto 0.02nm before decreasing to< 25pm	[80]
$\sim$ 1550nm[3] FWHM 0.138 to 1.249nm Transmission 0.1 to 30.3dB Refl. 1.7 to 99.9%	gamma: 0.1MGy	$\Delta\lambda_B$ varies from < 50 pm (G5) to over 150 pm (G8) Δ grating width varies from < 5 pm (G7) to over25 pm	[73]

---

[1] stabilised after 100kGy

[2] stabilised after 900kGy

[3] Three gratings of 12 types of

Multi-parameter Measurement with FBGs

For the accurate measurement of two or more variables, such as temperature and pressure, it is necessary to have two or more separate quantities affected differently by the environmental variables. There are a number of ways to do this using FBGs. Firstly, the simplest method is to use two gratings on two fibres with one de-coupled from the pressure environment, in this instance, and then assuming that this de-coupled grating is exposed to the same temperature as the coupled one.

A multi-parameter sensing method based on Bragg gratings written within multimode and polarisation maintaining single mode fibres is demonstrated in [81]. Multiple dips are seen in the transmission spectra due to the different reflecting modes present in a grating written in multimode fibre. The shapes of these dips can be monitored and calibrated to changes in pressure, strain, temperature etc. These gratings have been shown to work up to 1000°C. It is however quite complicated to monitor and calibrate for such changes in transmission spectra and it is preferable to work with single-mode fibre for reasons of cost and simplicity.

Another method is to use dual wavelength sensors, as is described in [82]. Here they form two gratings, Type Ia and and Type IIa, at the same spatial point on the fibre. Due to their differing sensitivities to temperature and strain it is possible to de-convolve the peak position changes due to temperature and strain. However this sensor is not suitable for use within a nuclear radiation environment as Type I gratings have been shown to be erased quickly under neutron and gamma radiation.

A further method for the measurement of multiple variables is presented in [81]. Here asymmetric gratings are written using IR femtosecond laser pulses. Both multi-mode (MM) and single-mode, polarisation-maintaining (SM/PM) fibres were trialled. The MM grating transmits multiple modes from the grating with each mode being slightly separated in wavelength from each other; each mode has a different sensitivity to changes in temperature/ strain/ bend etc.. The SM/PM fibre has only two orthogonal transmitting modes which are also differently affected by the prevailing environmental conditions.These sensors are interrogated in transmission and the full transmission profile is used to calculate the prevailing conditions at the sensor. However the main drawback of the MM sensor is that over 20nm of bandwidth is required to interrogate one sensor; typical transmission full width at half maximum (FWHM) bandwidth of a 1550nm super luminescent (SLD) is around 50 nm [83] , this would necessitate multiple lines with an optical switch to interrogate multiple sensors. It would not be possible to multiplex many sensors on one line. The SM/PM system represents a possible system for condition monitoring of temperature and strain; however it has the added challenge of polarisation interrogation combined with wavelength monitoring.

In [84] an extrinsic Fabry-Perot interferometer type sensor is used to discriminate between strain and temperature in a carbon-fibre composite material. The same sensor can also be calibrated to i) monitor the progress of cure in an epoxy/amine resin system; ii) the ingress of moisture in a cured epoxy/ amine resin system; iii) measure the vibration characteristics of pre- and post- impact damaged carbon fibre reinforced epoxy panels. However the Fabry-Pérot (FP) interferometer type of sensor cannot be easily multiplexed. Time domain multiplexing is the normal method of for discrimination of multiplexed FP sensor and this can take 1-5s [85] and is thus not viable for the application under investigation. The FP sensors do have potential for application to many other situations where accurate multi-parameter measurements at a slower update rate are required but there is a limited number of points of interest to be monitored.

3.3 Effect of Metal Embedding on FBG response

An equation for the temperature sensitivity of an embedded FBG has to cope with the interaction between the fibre and the metal into which it is embedded in [86],

$$\frac{\Delta\lambda_B}{\lambda_B} = (\alpha_f + \zeta)\Delta T + (1 - P_\alpha)(\alpha_m - \alpha_f)\Delta T \ , \tag{3.15}$$

where α_f is the coefficient of thermal expansion of fibre, and α_m is the coefficient of thermal expansion of the surrounding material, ζ is the thermo-optic coefficient, ΔT is the change in temperature, P_α is the strain-optic tensor, λ_B is the Bragg wavelength of the FBG, and $\delta\lambda_B$ is the change in the Bragg wavelength,everything else being previously defined.

Superficial examination of equation 3.15 suggests that the first term deals with the thermal properties of the fibre itself, while the second term gives the strain created in the interface between fibre and the surrounding material.

Consider shear forces between the fibre and surrounding material. Assume contact is never broken, as shown in [87], this states with reference to wavelength response of an embedded FBG to changing temperature, "No serious wavelength jumps occurred as would be expected if the fibre was slipping inside the metal embedding material".

In isolation, it would expect the following change in length caused by a change in temperature,

$$Fibre : \Delta L_f = L_0 \alpha_f \Delta T \ , \tag{3.16}$$

$$Metal : \Delta L_m = L_0 \alpha_s \Delta T \ , \tag{3.17}$$

where ΔT is the change in temperature in Kelvin, L_0 is the initial length of the fibre embedded in metal in metre (this being equivalent to he length of contact of between the fibre and metal), α_f is the coefficient of thermal expansion (CTE) of the fibre (K^{-1}) and α_s is the CTE of the metal.

The surrounding meal will dominate over the small, thin, fibre; therefore it is reasonable to assume that the fibre will have a negligible effect on the change in size of the metal; instead the metal will stretch the fibre to the metal's length. Thus the distance the metal will stretch the fibre is:

$$\Delta L_m - \Delta L_f = L_0(\alpha_s - \alpha_f)\Delta T \ , \tag{3.18}$$

This equates to a temperature induced strain on the fibre of

$$\Delta\epsilon_{temp} = \frac{\Delta L_m - \Delta L_f}{L_0} = (\alpha_s - \alpha_f)\Delta T \ , \tag{3.19}$$

The effect of a change in strain on the wavelength change of the Bragg grating has been previously given in Equation 3.7, thus it is possible to give the response due to a change in temperature as:

$$\frac{\Delta\lambda_{temp}}{\lambda_B} = (\alpha_f + \zeta)\Delta T + K_\epsilon \Delta\epsilon_{temp} = (\alpha_f + \zeta)\Delta T + (1 - p_\alpha)(\alpha_m - \alpha_f)\Delta T \ , \tag{3.20}$$

This gives the complete FBG response as

$$\frac{\Delta\lambda_{total}}{\lambda_B} = (1 - p_\alpha)\Delta\epsilon + [(\alpha_f + \zeta) + (1 - p_\alpha)(\alpha_m - \alpha_f)]\Delta T \ . \tag{3.21}$$

Thus this model matches the equation shown in [88].

3.4 Radiation Effect on Sensor Accuracy

The different effects of radiation on silica fibres, density changes, radiation induced absorption etc. have been detailed. However it is necessary to quantify the effect each mode of radiation has on the sensor's response. Using the data found in [59] for the change in volume of silica with neutron impact it is possible to calculate change in density. Then using formula 3.9, the effect of this density change on the refractive index can be calculated.

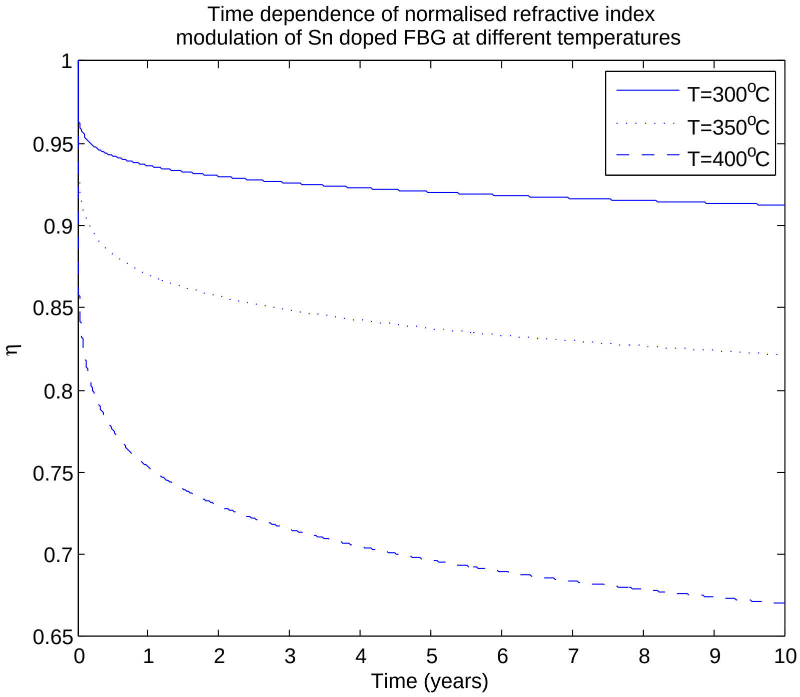

Figure 3.4: Change in normalised refractive index due to temperature and time changes of a tin doped FBG

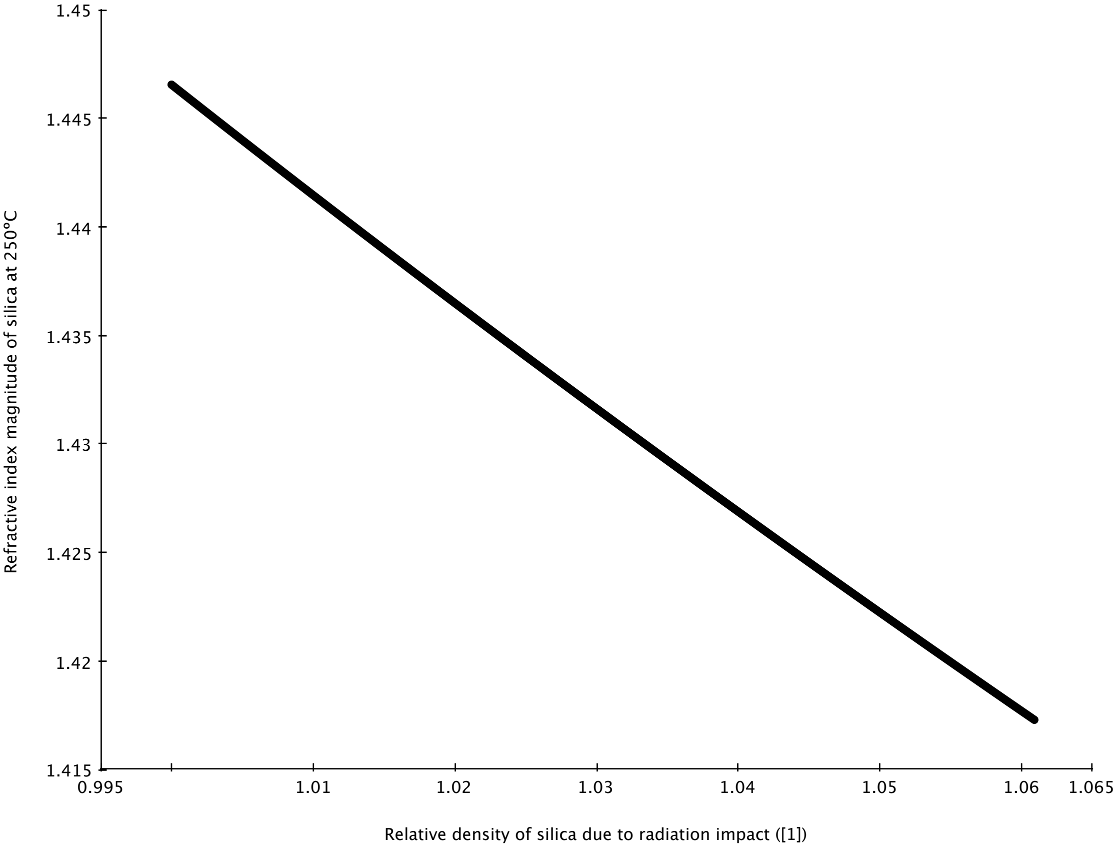

Figure 3.5: Absolute refractive index changes due to density change from radiation impact at 250°C

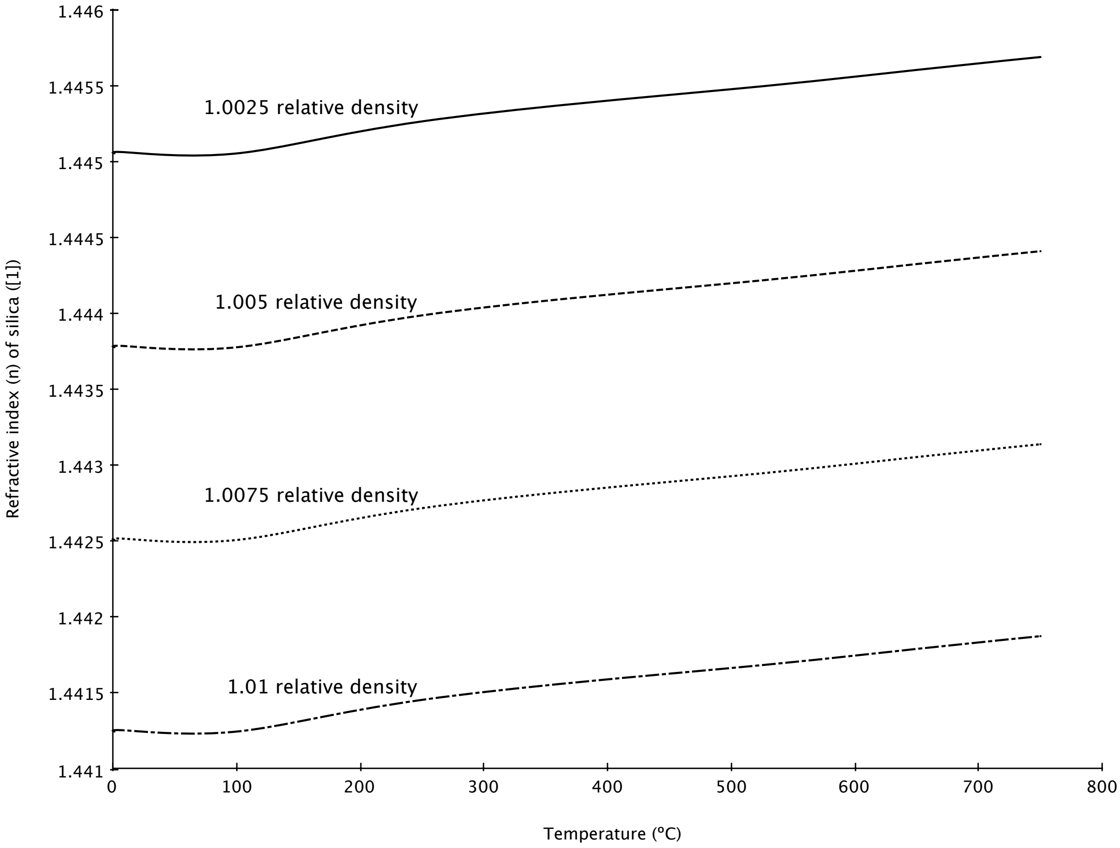

Figure 3.6: Absolute refractive index changes due to temperature changes

In Figure 3.5 it is possible to see the effect of increasing density is to decrease the refractive index. Changes in refractive index due to temperature are much smaller than those due to radiation density changes; this is shown in Figure 3.6.

There is an inverse relationship between refractive index and density. This means that as the density increases then n decreases causing a decrease in λ_B. Therefore in any system deployed into a nuclear fusion reactor this must be part of the calibration. As stated previously there must be a full radiation study of the different positions of the FBGs within the irradiated zone. This is so that an understanding of the dose that it will be exposed to over the experimental period must be known to be able to perform an accurate calibration.

3.5 Optical Wavelength Selection

FBGs reflect only a small component of the total bandwidth emitted from the optical sources typically with an FWHM of 0.3-1 nm. Therefore there are a number of requirements, specific and general, for the selection of an ideal interrogation method.

- High resolution with a large measurement range. The range to resolution ratio is within $1000 : 1$ and $100000 : 1$. For this application a range of at least 300 nm is required (1280-1580 nm). Thus a resolution between 3 pm and 0.3 pm is required.
- Cost effective; the cost of an interrogation system should be competitive with conventional optical or electrical sensors
- Multiplexing capability built in; the system must be able to cope with multiplexed topologies thus possibly making the whole sensing system more cost effective.

There are a number of methods that can be considered; these are the tuneable optical filter, the arrayed waveguide, and interferometric scanning. Each one has a number of advantages and disadvantages compared to the other. These are comprehensively reviewed in [89]. A short outline of each technique and its respective benefits and drawbacks is given below.

3.5.1 Arrayed Waveguide

The arrayed waveguide (AWG) does not require online calibration, however it does require the use of multiple photodiodes and their associated amplifiers for each optical channel. This means that compared to the optical filter, that only requires one amplifier, the AWG method is slower with the same digital to analogue converters; this is due to the requirement for each AWG channel to have its own DAQ channel. Although this problem can be overcome by the selection of a simultaneous DAQ card, the cost of such an accurate card is currently prohibitive. The AWG method also cannot cover both 1310 nm sensors and 1550 nm sensors in a single array, at least with commercially available devices. A diagram of an AWG is shown in Figure 3.7.

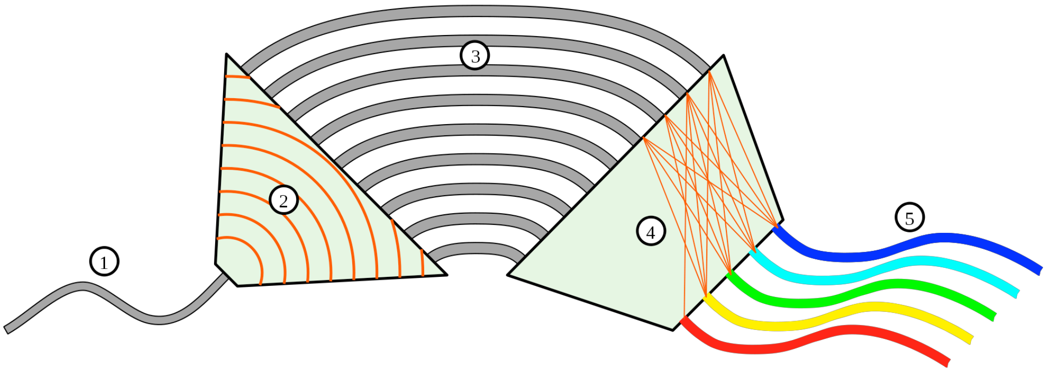

Figure 3.7: Arrayed Waveguide - diagrammatic layout. (1) input single mode fibre; (2) diffraction into linking fibres; (3) linking fibres of different lengths; (4) wavefronts interfere to give single wavelength band at each output fibre; (5) output fibres to photodetectors.[4]

---

[4] Used with permission under GNU Free Documentation License

3.5.2 Mach-Zehnder Interferometer

The most commonly used interferometric scanning method uses a Mach-Zehnder type interferometer [90] with one arm constant and the other varying in length. A diagram of the formation of this type of interferometer is shown in Figure 3.8.

This varying length changes the optical path difference between the arms, inducing a phase change in light travelling along both arms. A phase change, from the initial phase, can be interpreted as a change in wavelength of the FBG due to applied strain or temperature. This system cannot be used to multiplex sensors unless a further interrogation system is used as well. It does give very high resolution and thus can detect very small changes in the measurands accurately. As this system cannot deal with multiple sensors on one line it is not suitable for use in this application. Further, accurate measurement of very small changes is not required in this application.

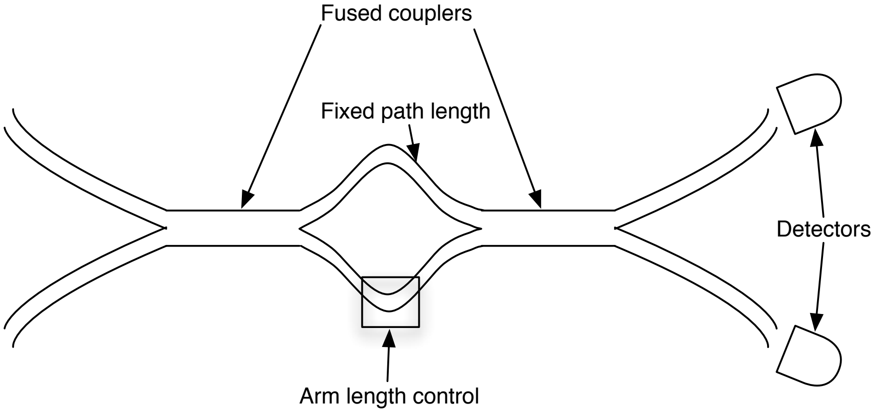

Figure 3.8: Layout of an in-fibre Mach-Zehnder interferometer for wavelength discrimination. One path length is fixed and the other can be varied using an actuator, for example a piezoelectric system.

3.5.3 Tuneable Optical Filter

A Tuneable optical filter can be used to measure the wavelength shift in an FBG peak due to strain or temperature changes. The output of the filter is the convolution of the peak and filter spectra. In a high resolution filter, when the passband spectrum of the filter matches part of the reflected FBG spectrum a current is generated on the photodiode as a result of the photoelectric effect where the energy of the incoming photos equals or exceeds the energy required to release an electron/hole pair from a bound state. The spectrum of the peak is then created by recording the multiple points where current is generated. This spectrum is analysed in software to find the peak(s)' position using a threshold method or other suitable peak detection algorithm.

To be able to work in both the 1310 nm and 1550 nm bands a tuneable optical filter is the only option, if only one interrogation device is to be used. Currently the only wideband optical filter available on the market is that manufactured by Micron Optics Inc. The optical filter from Micron Optics (TFP-2 9000) is of the electrically driven piezoelectric Fabry-Perot etalon type.

3.5.4 Technology Choice

From the available selection of interrogation methods the tuneable optical filter is chosen as it has long term stability, is not highly influenced by temperature variations, has adjustable resolution and is capable of addressing many sensors. A Fabry-Pérot tuneable wideband optical filter is described in detail below.

3.6 Simultaneous measurement of strain and temperature using dual wavelength FBGs

This section examines the proposal for using two chemical composition gratings (CCGs) etched on the same point on a fibre optic cable to enable simultaneous reading of strain and temperature; particularly looking at the method for extracting this data from the wavelength results, and trying to predict the accuracy of this procedure and any problems it may entail.

3.6.1 Matrix Analysis

The key formula is the matrix relating strain and temperature's effect on wavelength shift:

$$\begin{bmatrix} \Delta\epsilon \\ \Delta T \end{bmatrix} = \begin{bmatrix} \Delta\lambda_{B1} \\ \Delta\lambda_{B2} \end{bmatrix} = \begin{bmatrix} K_{\epsilon 1} & K_{T1} \\ K_{\epsilon 2} & K_{T2} \end{bmatrix}, \tag{3.22}$$

where $\Delta\lambda_B$ is the change in peak wavelength, $K_{\epsilon i}$ is the strain sensitivity, K_{Ti} is the temperature sensitivity, $\Delta\epsilon$ is the change in strain, and ΔT is the change in temperature.

The proposal above is to use dual wavelength chemical composition gratings which have different strain/temperature sensitivities at each wavelength. However there is no full data available on the sensitivities of chemical composition gratings. Due to their similarities to normal FBGs so the sensitivities given in Table 3.2 come from [89].

By making use of the different sensitivities to strain and temperature it should be possible to separate the two variables from the results. This is shown in Figure 3.9. To test this approach, set the change in strain at 5000$\mu\epsilon$ and change in temperature to 500K (the expected range for use in the ITER reactor). Putting these values into Equation 3.22 above gives $\Delta\lambda_{B1} = 4000$pm and $\Delta\lambda_{B2} = 5000$pm. Now, if the

Table 3.2: Strain and temperature sensitivities of 1310nm and 1550nm FBGs

Bragg Wavelength	Strain Sensitivity (pm per microstrain)	Temp Sensitivity (pm/ K)
1310	∼1	∼10
1550	∼1.2	∼13

matrix equation is inverted, i.e.:

$$\begin{bmatrix} \Delta\epsilon \\ \Delta T \end{bmatrix} = \begin{bmatrix} K_{\epsilon 1} & K_{T1} \\ K_{\epsilon 2} & K_{T2} \end{bmatrix}^{-1} \begin{bmatrix} \Delta\lambda_{B1} \\ \Delta\lambda_{B2} \end{bmatrix} = \frac{1}{(K_{\epsilon 1}K_{T2} - K_{\epsilon 2}K_{T1})} \begin{bmatrix} K_{\epsilon 1} & K_{T1} \\ K_{\epsilon 2} & K_{T2} \end{bmatrix} , \quad (3.23)$$

and then the values substituted back in, the strain and temperature readings are, as expected, $5000\mu\epsilon$ and 500K. A simple error analysis must be performed first.

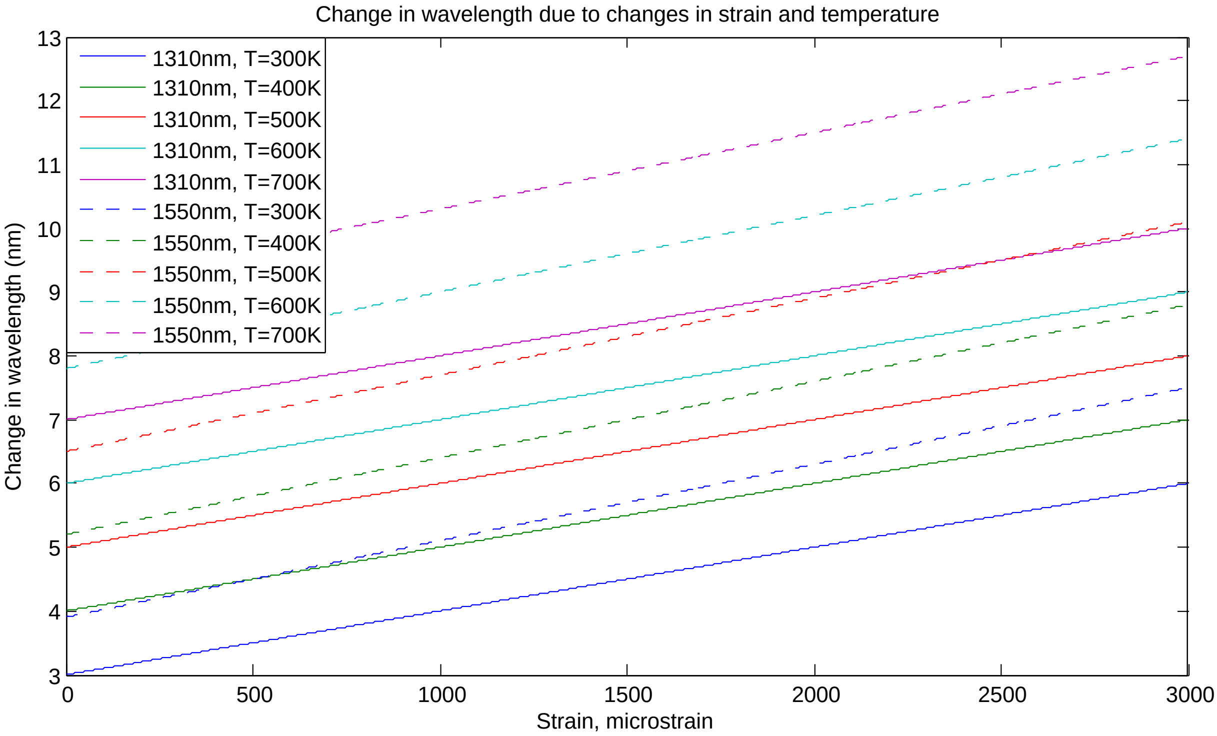

Figure 3.9: Different responses of two wavelength CCGs with varying temperature and strain calculated given the sensitivities given in [89]

3.6.2 Wavelength Uncertainty Analysis

Error Size for 1300nm and 1550nm Grating Pair

If it is assumed that the system can read wavelength to an accuracy of ±1pm (standard accuracy interrogation systems are currently capable of). In the worst cast scenario, this gives $\Delta\lambda B1 = 10001$pm and $\Delta\lambda B2 = 12499$pm. Using these values, strain and temperature changes are calculated as 5023$\mu\epsilon$and 497.8K. Further calculations are shown in Figures 3.10 and 3.11.

The problem is that the temperature and strain sensitivities are reasonably well correlated between the two gratings; there is a 20% increase in the strain sensitivity and a 30% increase in temperature sensitivity. This makes it difficult to separate the two variables when readings are not exact. If, hypothetically, the temperature sensitivity changed from 10pm/K to 25pm/K, while the strain sensitivity remained the same (giving very different ratios), then recalculating values with the same reading inaccuracies would gives the strain and temperature changes as 5002.692$\mu\epsilon$ and 499.8K very nearly perfect. Unfortunately, there are no CCGs of this imaginary specification available on the market currently.

Use of a 830nm FBG

One of the motivations for using 1300nm and 1550nm FBGs is that the wavelengths are similar enough that they can both be seen on a single scan by an interrogation unit. Having two wavelengths further apart would complicate reading the results. However for now consider the possible use of a 830nm FBG. It has been shown that pairing a 1300nm and a 1550nm FBG gives the maximum strain error of $23\mu\epsilon$ and the maximum temperature error of -2.2K (going up to $5000\mu\epsilon$ and 500°C) when reading wavelength to an accuracy of 1pm. Alternatively, pairing with a 830nm FBG gives:

Table 3.3: Strain and temperature sensitivities of 830nm FBG

Bragg Wavelength (nm)	Strain Sensitivity (pm per microstrain)	Temp Sensitivity (pm/ K)
830	~ 0.64	6.8

- $-42\mu\epsilon$ and +4.1°C when paired with 1300nm
- $123.75\mu\epsilon$ and -11.5°C when paired with 1550nm

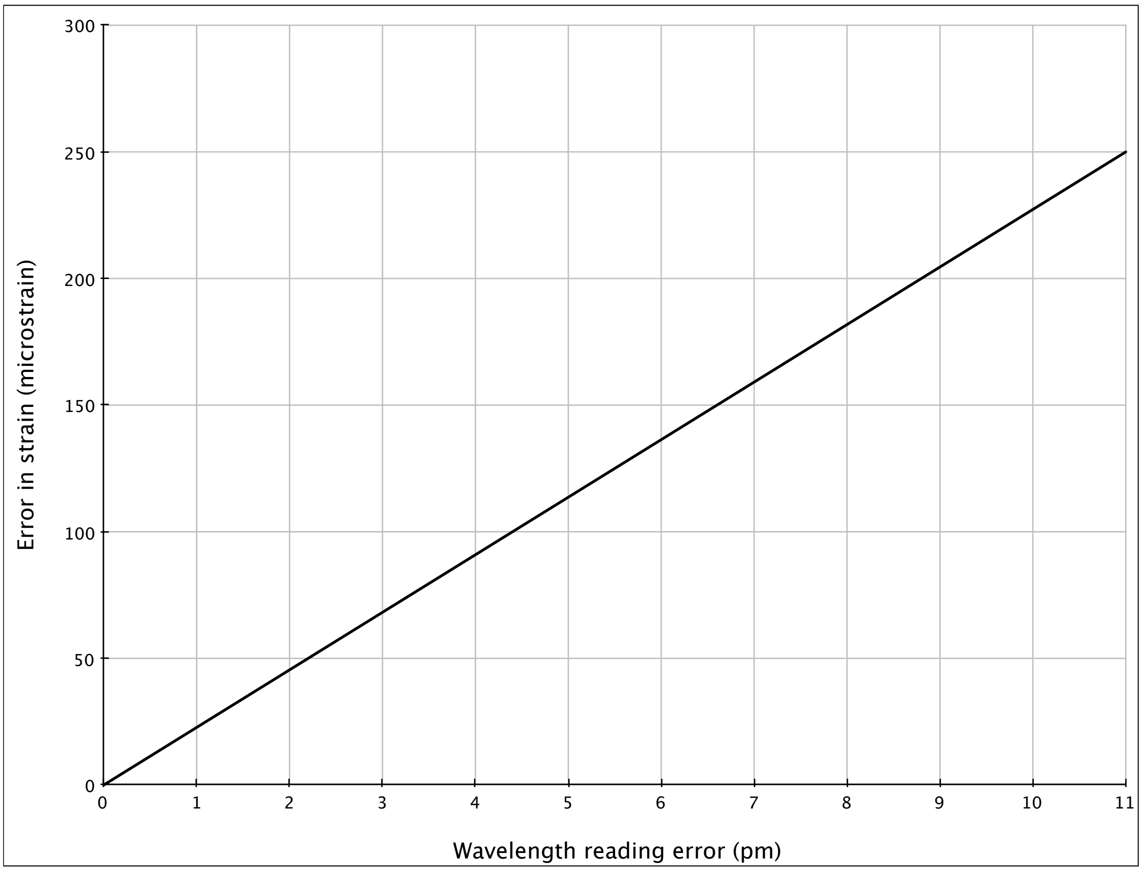

Figure 3.10: Expected strain errors for worst-case scenario with real gratings, when change in strain = $5000\mu\epsilon$ and change in temperature = 500K

The 830nm FBG has more similar temperature and strain sensitivity ratios and therefore less accurate results. In addition, it would require a second interrogation unit since the wavelengths are further apart. Use of the 1300nm and 1550nm pair is clearly preferable.

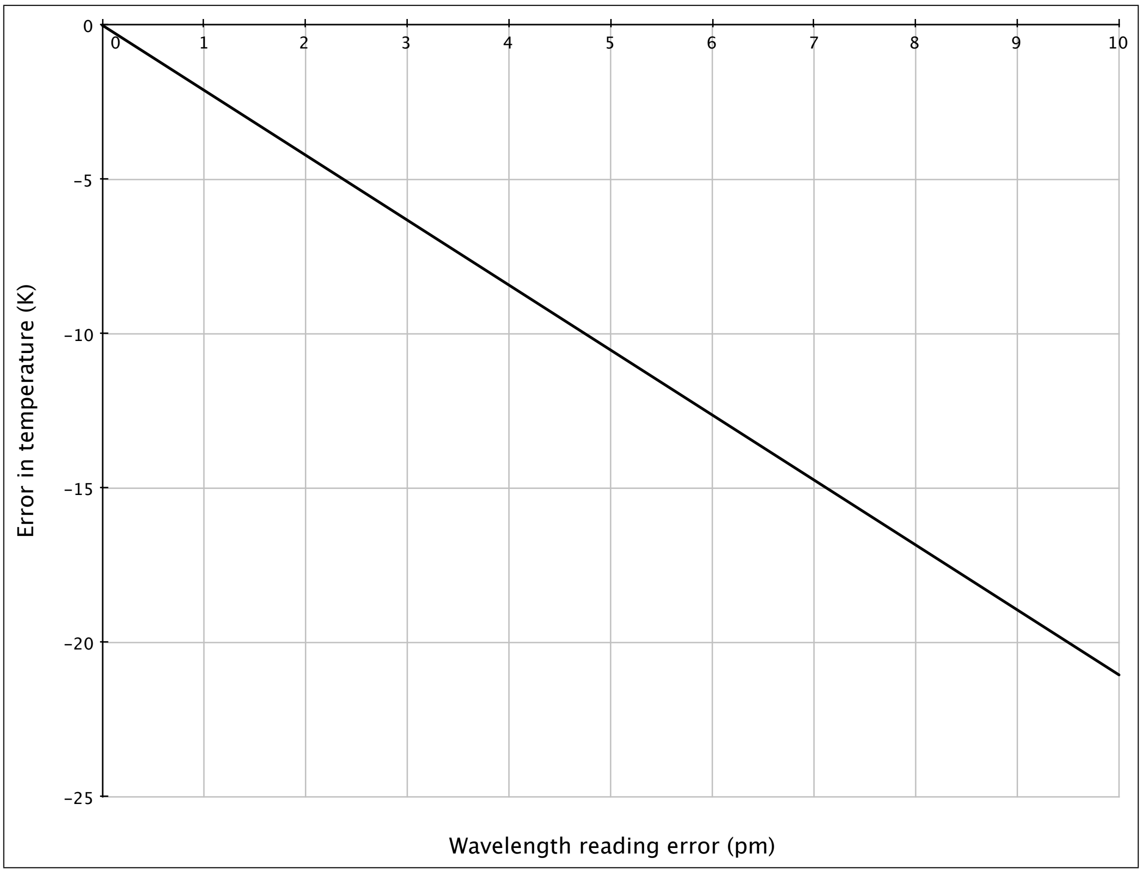

Figure 3.11: Expected temperature errors for worst-case scenario with real gratings, when change in strain = $5000\mu\epsilon$ and change in temperature = 500K

3.6.3 Temperature Dependence of Strain and Temperature Sensitivities

The above analysis assumes that the temperature and strain sensitivities are constant for all temperatures and strains. It is unlikely that this is true, as,

- Strain tensors - temperature dependent
- Poisson ratio - temperature dependent
- Refractive index - temperature dependent [91]
- Thermal expansion co-efficient - temperature dependent.
- Thermo-optic coefficient - since refractive index is temperature dependent, and the thermo-optic coefficient $\zeta = dn/dT$ (i.e. variation of refractive index with temperature) this is also temperature dependent; in addition see [92].

In summary, the assumption that temperature and strain sensitivities will stay constant across the required ranges, $0\mu\epsilon$ to $5000\mu\epsilon$; 273K to 773K, is clearly an approximation. This will add to errors, and needs further analysis.

$$\lambda(T,\epsilon) = \lambda_B \left(1 + \epsilon - \frac{n_0^2(T)}{2}[p_{12}(T)\epsilon + (p_{11}(T) + p_{12})\nu(T)\epsilon] + (\alpha + \zeta)T\right) \ , \quad (3.24)$$

$$\frac{\Delta\lambda(T)}{\Delta\epsilon} = \lambda_B \left(1 - \frac{n_0^2(T)}{2}[\nu(T)p_{11}(T) + p_{12}(T)[\nu(T) + 1]]\right) \ , \quad (3.25)$$

$$\frac{\Delta\lambda(T)}{\Delta\epsilon} = \lambda_B \left(1 - \frac{n_0^2(T)}{2}[p_{12}(T) + \nu(T)(p_{11}(T) + p_{12}(T))]\right) \ , \quad (3.26)$$

where all variables are given in Table 3.4

Unfortunately, the given formula in [93] is different from the standard formula:

$$\frac{\Delta\lambda(T)}{\Delta\epsilon} = \lambda_B \left(1 - \frac{n_0^2(T)}{2}[p_{12}(T) - \nu(T)(p_{11}(T) + p_{12}(T))]\right) \ . \quad (3.27)$$

Due to these inconsistencies between the various sources the dependence of strain and temperature measurement is derived from the first principles in the subsection below.

Table 3.4: Variables for errors in temperature dependence on strain sensitivity

$\nu = 0.25$	$d\nu/dT = 2.5 \times 10^{-5}$
$\lambda_B = 850\,nm$	$d\lambda_B/dT = 7 \times 10^{-12} m\dot{K}^{-1}$
$n_{eff} = 1.5$	$dn/dT(silica) = 10.8 \times 10^{-6} K^{-1}$
$p_{12} = 0.251, p_{11} = 0.133$	$dp_{12}/dT = dp_{11}/dT = -0.134 \times 10^{-3} K^{-1}$

3.6.4 Derivation of FBG sensitivities from the first principles

Starting from the relationship between the Bragg wavelength λ_B, the glass refractive index n and the grating period Λ the sensitivities to temperature and strain will be derived.

$$\lambda_B = 2n\Lambda \ , \tag{3.28}$$

By partial differentiation with respect to strain and temperature the following relationship is found.

$$\Rightarrow \Delta\lambda_B = \left(2\frac{\partial n}{\partial \epsilon_z}\Lambda + 2n\frac{\partial \Lambda}{\partial \epsilon_z}\right)\Delta\epsilon_z + \left(2\frac{\partial n}{\partial T}\Lambda + 2n\frac{\partial \Lambda}{\partial T}\right)\Delta T \ , \tag{3.29}$$

Now taking strain and temperature separately it is possible to derive the error in the measurement due to each physical effect.

Strain

First differentiate the Bragg wavelength with respect to strain,

$$\frac{d\lambda_B}{d\epsilon_z} = 2\frac{\partial n}{\partial \epsilon_z} + 2n\frac{\partial \Lambda}{\partial \epsilon_z} \ . \tag{3.30}$$

where λ_B is the Bragg wavelength,ϵ_z is the strain applied in the z-direction (along the fibre), is the refractive index, and Λ is the grating period. Now since from before it is known that,

$$\epsilon = \frac{\Delta l}{l} = \frac{\Delta\Lambda}{\Lambda} \ , \tag{3.31}$$

and also that

$$\Lambda_new = \Lambda + \Delta\Lambda = \Lambda + \Lambda\left(\frac{\Delta\Lambda}{\Lambda}\right) = \Lambda + \Lambda\epsilon \ , \tag{3.32}$$

$$\Rightarrow \frac{\partial\Lambda}{\partial\epsilon_z} = \Lambda \ , \tag{3.33}$$

and given (derived below)

$$\partial n = \frac{-n^3}{2}\left[(P_{11} + P_{12})\epsilon_r + P_{12}\epsilon_z\right] \ . \tag{3.34}$$

Then substitute the expression for ∂n in to the original equation

$$\therefore \frac{d\lambda_B}{d\epsilon_z} = -n^3\left[P_{11} - \nu(P_{11} + P_{12})\right] \ , \tag{3.35}$$

$$\Rightarrow \frac{d\lambda_B}{d\epsilon_z} = 2n\Lambda\left[1 - \frac{n^2}{2}\left[P_{11} - \nu(P_{11} + P_{12})\right]\right] \ , \tag{3.36}$$

$$\Rightarrow \frac{d\lambda_B}{d\epsilon_z} = \lambda_B\left[1 - \frac{n^2}{2}\left[P_{11} - \nu(P_{11} + P_{12})\right]\right] \ . \tag{3.37}$$

Temperature

Separating out to find the dependence only on temperature.

$$\frac{d\lambda_B}{dT} = 2\frac{\partial n}{\partial T}\Lambda + 2n\frac{\partial\Lambda}{\partial T} \ . \tag{3.38}$$

Now it can be shown that

$$\frac{\partial\Lambda}{\partial T} = \alpha\Lambda \ . \tag{3.39}$$

Thus by substituting into the original equation the dependence of the Bragg wavelength on temperature can be found.

$$\therefore \frac{d\lambda_B}{dT} = 2\frac{\partial n}{\partial T}\Lambda + 2n\alpha\Lambda \ , \tag{3.40}$$

$$\Rightarrow \frac{d\lambda_B}{dT} = 2n\Lambda\left(\alpha + \frac{1}{n}\frac{\partial n}{\partial T}\right) \ , \tag{3.41}$$

This can be reduced further to

$$\frac{d\lambda_B}{dT} = \lambda_B(\alpha + \zeta) \ . \tag{3.42}$$

Derivation of ∂n

$$\Delta \left[\frac{1}{n^2}\right] = -\frac{2\Delta n}{n^3} \ , \tag{3.43}$$

$$\Rightarrow \Delta n = -\frac{n^3}{2}\Delta \left[\frac{1}{n^2}\right] \ . \tag{3.44}$$

Strain-optic theory predicts that

$$\Delta \left[\frac{1}{n^2}\right]_i = \beta_{ij}\epsilon_j \ , \quad i = 1, 2j = 1, 2, 3 \ , \tag{3.45}$$

where ϵ_j is the block-reduced strain tensor in the fibre, and β is the contracted strain optic tensor of the fibre with Pockel's coefficients p_{ij}, where i and j describe the coordinate axes of the fibre; $x = 1, y = 2, z = 3$. z is the direction the fibre takes (that is, it is aligned with the centroid of the fibre). And

$$\beta_{ij} = \begin{bmatrix} p_{11} & p_{12} & p_{13} \\ p_{21} & p_{22} & p_{23} \\ p_{31} & p_{32} & p_{33} \end{bmatrix} \ , \qquad \epsilon_j = \begin{bmatrix} \epsilon_x \\ \epsilon_y \\ \epsilon_z \end{bmatrix} \ . \tag{3.46}$$

For a low birefringent FBG fibre, typically used today, the strain-optical tensor is approximately isotropic $p_{11} = p_{22} = p_{33}$ and $p_{12} = p_{13} = p_{23}$.

So let $\epsilon_x = \epsilon_y = \epsilon_r$, that is use cylindrical components.

Therefore it can be shown that

$$\therefore \Delta \left[\tfrac{1}{n^2}\right]_i = \begin{bmatrix} p_{11} & p_{12} & p_{13} \\ p_{21} & p_{22} & p_{23} \\ p_{31} & p_{32} & p_{33} \end{bmatrix} \begin{bmatrix} \epsilon_x \\ \epsilon_y \\ \epsilon_z \end{bmatrix} = \begin{bmatrix} (p_{11} + p_{12})\epsilon_r + p_{12}\epsilon_z \\ (p_{11} + p_{12})\epsilon_r + p_{12}\epsilon_z \\ 2p_{12}\epsilon_r + p_{11}\epsilon_z \end{bmatrix} \ , \tag{3.47}$$

$$\text{with } i\text{=1,2: } \partial n = -\frac{n^3}{2}\left[\left(p_{11} + p_{12}\right)\epsilon_r + p_{12}\epsilon_z\right] \ , \tag{3.48}$$

where i = 1,2 determine the polarisation of the light concerned. Since the x and y planes are under identical conditions in the analysis of the fibre, it does not matter which is examined; however, looking at the z-plane would give the wrong results as the light waves do not oscillate in this direction in single mode fibre.

Temperature dependence of strain sensitivity

In this section the temperature dependence of the strain sensitivity will be derived. Starting from the equation relating Bragg wavelength changes due to strain changes (Equation 3.24).

Expanding through

$$\Rightarrow \frac{\Delta\lambda(T)}{\Delta\epsilon} = \lambda_B - \lambda_B \frac{n_0^2(T)}{2} p_{12}(T) + \lambda_B \frac{n_0^2(T)}{2} \nu(T) p_{11}(T) + \lambda_B \frac{n_0^2(T)}{2} \nu(T) p_{12}(T)\ . \tag{3.49}$$

Then differentiating by temperature

Now using $dp_{11}/dT = dp_{12}/dT = dp/dT$ and collecting the terms it can be shown that

$$\begin{aligned} \Rightarrow \frac{d\left(\frac{\Delta\lambda(T)}{\Delta\epsilon}\right)}{dT} &= \lambda_B n_0 \left(-\frac{dn_0}{dT} p_{12} - \frac{n_0}{2}\frac{dp}{dT} + \frac{dn_0}{dT} \nu p_{11}\right. \\ &\qquad \left. + \frac{n_0}{2} \nu \frac{dp}{dT} + \frac{dn_0}{dT} \nu_{12} + \frac{d\nu}{dT} p_{12} + \frac{n_0}{0} \nu \frac{p}{dT}\right) \end{aligned} \tag{3.50}$$

$$\begin{aligned} \Rightarrow \frac{d\left(\frac{\Delta\lambda(T)}{\Delta\epsilon}\right)}{dT} &= \lambda_B n_0 \left[\frac{dn_0}{dT}(-p_{12} + \nu p_{11} + \nu p_{12})\right. \\ &\qquad \left. + \frac{n_0}{2}\left(-\frac{dp}{dT} + \frac{d\nu}{dT} p_{11} + 2\nu \frac{dp}{dT} + \frac{d\nu}{dT} p_{12}\right)\right] \end{aligned} \tag{3.51}$$

$$\begin{aligned} \Rightarrow \frac{d\left(\frac{\Delta\lambda(T)}{\Delta\epsilon}\right)}{dT} &= \lambda_B n_0 \left[\frac{dn_0}{dT}(-p_{12} + \nu(p_{11} + p_{12}))\right. \\ &\qquad + \frac{n_0}{2}\left(-\frac{dp}{dT}(2\nu - 1) + \frac{d\nu}{dT}(p_{11} + p_{12})\ )]\right. \end{aligned} \tag{3.52}$$

where all the variables are given in Table 3.5

Table 3.5: Variables for the thermal dependence of the strain sensitivity [93]

Quantity	Value	Quantity	Value
ν	0.25	$d\nu/dT$	$2.5 \times 10^{-4}\% K^{-1} = 2.5 \times 10^{-6} K^{-1}$
λ_B	850nm	$d\lambda_B/dT$	7×10^{-12}m K $^{-1}$
n_{eff}	1.5	dn/dT (silica)	10.8×10^{-6} K $^{-1}$
p_{11}, p_{12}	0.133, 0.251	$dp_{11}/dT = dp_{12}/dT$	-0.134×10^{-3}K $^{-1}$

3.7 Error Analysis of simultaneous Measurement of Strain and Temperature using Dual Wavelength FBGs

The premise of this thesis is that a single sensor can be used to detect changes in both temperature and strain. A number of simultaneous measurement techniques have been outlined in Section 3.2.5; however it is necessary to give an estimate of the error coming from the measurement accuracy and noise of the proposed system. Below a generic analysis of dual measurement techniques is outlined as shown in [94].

In this analysis ϕ_1 and ϕ_2 are the parameters to be measured, these are related to the measurands, temperature and strain in this case, through a linear transform. This is represented below in matrix format,

$$\mathbf{\Phi} = K\Omega \, , \tag{3.53}$$

where

$$\mathbf{\Phi} = \begin{bmatrix} \phi_1 \\ \phi_2 \end{bmatrix} , \tag{3.54}$$

and

$$\mathbf{K} = \begin{bmatrix} K_{1T} & K_{1\epsilon} \\ K_{2T} & K_{2\epsilon} \end{bmatrix} , \tag{3.55}$$

where $\mathbf{K}$ is the characteristic matrix of the sensor, i.e. the transfer matrix from Ω to Φ. When $\Delta = K_{1T}K_{2\epsilon} - K_{2T}K_{1\epsilon}$, the determinant, of $\mathbf{K}$ is not zero then (3.53) may be inverted to calculate the changes in T and ϵ as shown below.

$$\Omega = K^{-1}\Phi \ , \tag{3.56}$$

where K^{-1} is the inverse matrix of $\mathbf{K}$ and is defined as

$$\mathbf{K}^{-1} = \frac{\mathbf{K}'}{\Delta} \ , \tag{3.57}$$

with **K'** defined by

$$\mathbf{K}' = \begin{bmatrix} K_{2\epsilon} & -K_{1\epsilon} \\ -K_{2T} & K_{1T} \end{bmatrix} \ . \tag{3.58}$$

Often the condition number of the transfer matrix is used to give a qualitative estimate of the sensor behaviour; the best sensors having a low condition number.

However using the condition number for analysing the error in a dual measurand system gives no information on how the error is distributed between the two measurands, i.e. $|\delta\Omega|$ (the error vector) gives no information on the value of $|\delta T|$ or $|\delta\epsilon|$. Thus if $|\delta\Omega|$ is 50, there is no mathematical method of knowing if this is 50°C or $50\mu\epsilon$ or more likely a proportion of both. Thus below a method is outlined to quantify the error in T and ϵ resulting from the imprecise measurement of Φ_1 and Φ_2.

3.7.1 Formula for error size

The changes in strain and temperature are,

$$\Delta\epsilon = \frac{K_{T2}\Delta\lambda_{B1} - K_{T1}\Delta\lambda_{B2}}{K_{\epsilon 1}K_{T2} - K\epsilon 2K - T1} \ , \tag{3.59}$$

$$\Delta T = \frac{-K_{\epsilon 2}\Delta\lambda_{B1} + K_{\epsilon 1}\Delta\lambda_{B2}}{K_{\epsilon 1}K_{T2} - K_{\epsilon 2}K_{T1}} \ , \tag{3.60}$$

where all symbols have been defined previously in Section 3.2.1

Define the second FBG as having the largest wavelength, that is, $\lambda_{B1} < \lambda_{B2} \implies \Delta\lambda_{B1} < \Delta\lambda_{B2}$.

Then define δ as the wavelength reading error of the interrogation stage, then it is possible to model the worst case wavelength inaccuracy (when reading error at each wavelength brings the two readings closest together) by

$$\Delta\lambda_{B1} = \Delta\lambda_{B1} + \delta \ , \tag{3.61}$$

$$\Delta\lambda_{B2} = \Delta\lambda_{B2} + \delta \ . \tag{3.62}$$

It is then possible to calculate the strain,

$$\Delta\epsilon_{with\delta} = \frac{K_{T2}(\Delta\lambda_{B1} + \delta}{-K_{T1}(\Delta\lambda_{B2} - \delta)} K_{\epsilon 1}K_{T2} - K\epsilon 2K - T1 \ , \tag{3.63}$$

$$\implies \Delta\epsilon_{with\delta} = \frac{K_{T2}\Delta\lambda_{B1} - K_{T1}\Delta\lambda_{B2} + \delta(K_{T2} + K_{T1}}{K_{\epsilon 1}K_{T2} - K_{\epsilon 2}K_{T1}} \ , \tag{3.64}$$

$$\implies \text{Strain Error } = \frac{\delta(K_{T1} + K_{T2}}{K_{\epsilon 1}K_{T2} - K_{\epsilon 2}K_{T1}} \ , \tag{3.65}$$

and similarly for the temperature error

$$\Delta T = \frac{-K_{\epsilon 2}(\Delta\lambda_{B1} + \delta) + K_{\epsilon 1}(\Delta\lambda_{B2} - \delta)}{K_{\epsilon 1}K_{T2} - K_{\epsilon 2}K_{T1}} \ . \tag{3.66}$$

3.7.2 Sensor Resolution Limited by Errors in Φ and K: General Formulation

When both ϕ and $\mathbf{K}$ have errors as,

$$\Phi = \Phi_0 + \delta\phi \ , \tag{3.67}$$

$$\mathbf{K} = K_0 + \delta K \ , \tag{3.68}$$

where Φ_0 and $\mathbf{K}_0$ represent the true values of Φ and $\mathbf{K}$, respectively. $\delta\Phi$ and $\delta\mathbf{K}$ represent the errors in Φ and $\mathbf{K}$ and can be expanded as,

$$\delta\Phi = \begin{bmatrix} \delta\phi_1 \\ \delta\phi_2 \end{bmatrix} \ , \tag{3.69}$$

and

$$\delta\mathbf{K} = \begin{bmatrix} K_{1T}\delta_{1T} & K_{1\epsilon}\delta_{1\epsilon} \\ K_{2T}\delta_{2T} & K_{2\epsilon}\delta_{2\epsilon} \end{bmatrix} \ , \tag{3.70}$$

where δ_{ij} (i = 1,2 and $j = T$ and ϵ) represents the fractional error in each element.

Thus the error in T and ϵ can be calculated by,

$$\delta\Omega = \mathbf{K}^{-1}\mathbf{\Phi} - \mathbf{K}_0^{-1}\mathbf{\Phi}_0 \ , \tag{3.71}$$

Using equation 3.57 it can be shown that

$$\delta\Omega = \frac{\mathbf{K}'\mathbf{\Omega}}{\Delta} - \frac{\mathbf{K_0'\Omega_0}}{\Delta_0} = \frac{\mathbf{K'}_0\delta\Phi\Delta_0 + \delta\mathbf{K}'\Phi_0\Delta_0 + \delta\mathbf{K}'\delta\Phi\Delta_0 - \mathbf{K'}_0\Phi_0\Delta^*}{\Delta_0(\Delta_0 + \Delta^*)} \ , \tag{3.72}$$

where

$$\delta\mathbf{K}' = \mathbf{K}' - \mathbf{K'}_0 = \begin{bmatrix} K_{2\epsilon}\delta_{2\epsilon} & -K_{1\epsilon}\delta_{1\epsilon} \\ -K_{2T}\delta_{2T} & K_{1T}\delta_{1T} \end{bmatrix} \ , \tag{3.73}$$

and

$$\Delta^* = \Delta - \Delta_0 = K_{1T}K_{2\epsilon}(\delta_{1T} + \delta_{2\epsilon} + \delta_{1T}\delta_{2\epsilon}) - K_{1\epsilon}K_{2T}(\delta_{1\epsilon} + \delta_{2T} + \delta_{1\epsilon}\delta_{2T}). \tag{3.74}$$

For the system under consideration in this thesis, and for most real-world systems, the error conditions δ_{ij} and $\delta\Phi_i$ are unknown. Only maximum possible values of $|\delta_{ij}|$ and $|\Phi_i|$ can be estimated. Thus with this information, and assuming accumulative errors, a realistic maximum error can be obtained.

3.7.3 Negligible Error in the Transfer Matrix Elements

If the errors in the transfer matrix are neglected and all errors are thus attributed to the inaccuracies in determining Φ_1 and Φ_2 the measurement error in this case is thus:

$$\delta\Omega = \frac{\mathbf{K}'\delta\mathbf{\Phi}}{\Delta} \ , \tag{3.75}$$

and expanding the matrices of equation 3.75 the maximum errors in T and ϵ are,

$$|\delta T| \leq \frac{|K_{2\epsilon}||\delta\phi_1| + |K_{1\epsilon}||\delta\phi_2|}{|\Delta|} \ , \tag{3.76}$$

$$|\delta\epsilon| \leq \frac{|K_{2T}||\delta\phi_1| + |K_{1T}||\delta\phi_2|}{|\Delta|} \ . \tag{3.77}$$

Thus the error in measuring $\phi_{1,2}$ is transferred to the measurands T and ϵ; however there is no dependence of the error magnitude on T and ϵ. In the system discussed in this thesis the error in wavelength measurement across the optical range of interest can be assumed to be the same; thus,

$$|\delta\phi_1| = |\delta\phi| = |\delta\phi_2| \; . \tag{3.78}$$

And the error in T and ϵ can be expressed as,

$$|\delta T| \leq \frac{(|K_{2\epsilon}| + |K_{1\epsilon}|)}{|\Delta|}|\delta\phi| = \beta_T|\delta\phi| \; , \tag{3.79}$$

$$|\delta\epsilon| \leq \frac{(|K_{1T}| + |K_{2T}|)}{|\Delta|} = \beta_\epsilon|\delta\phi| \; , \tag{3.80}$$

where $\beta_T = |K_{2\epsilon}| + |K_{1\epsilon}|$ and $\beta_\epsilon = |K_{1T}| + |K_{2T}|$. In Chapter 4 these equations will be applied to the system proposed in this thesis.

3.7.4 Measurement Dominated by Significant Matrix Element Error

Consider when there is negligible measurement error, then the error from 3.72 is thus

$$\delta\Omega = \frac{\left(\delta\mathbf{K}'\Delta_0 - \mathbf{K}_0'\Delta^*\right) .\Phi_0}{\Delta_0(\Delta_0 - \Delta^*)} \tag{3.81}$$

In terms of δT and $\delta\epsilon$ the above equation can be normalised to obtain the relative errors then

$$\delta T = \frac{(-K_{1T}K_{2\epsilon}\delta_{1T} + K_{1\epsilon}K_{2T}\delta_{2T})T + K_{1\epsilon}K_{2\epsilon})\delta_{2\epsilon} - \delta_{1\epsilon)\epsilon}}{(\Delta_0 + \Delta^*)} \; , \tag{3.82}$$

$$\delta\epsilon = \frac{(K_{1\epsilon}K_{2T}\delta_{1\epsilon} - K_{1T}K_{2\epsilon}\delta_{2\epsilon}\epsilon + K_{1T}K_{2T}(\delta_{1T} - \delta_{2T})T}{(\Delta_0 + \Delta^*)} \; . \tag{3.83}$$

Using the above equations it is possible to calculate the measurement error in T and ϵ at specific temperature and strain levels. It is possible to modify equations 3.82 and 3.83 to estimate the sensitivity of the strain/ temperature recovery process, that is to calculate the minimum change in strain that can be detected for a given temperature excursion.

$$\frac{\delta T}{T} = \frac{(-K_{1T}K_{2\epsilon}\delta_{1T} + K_{1\epsilon}K_{2T}\delta_{2T}) + K_{1\epsilon}K_{2\epsilon})\delta_{2\epsilon} - \delta_{1\epsilon})\epsilon/T}{(\Delta_0 + \Delta^*)} \; , \tag{3.84}$$

$$\frac{\delta\epsilon}{\epsilon} = \frac{(K_{1\epsilon}K_{2T}\delta_{1\epsilon} - K_{1T}K_{2\epsilon}\delta_{2\epsilon} + K_{1T}K_{2T}(\delta_{1T} - \delta_{2T})T/\epsilon}{(\Delta_0 + \Delta^*)} \ . \tag{3.85}$$

By substituting $|\delta_{ij}|$ into the above equations and allowing the errors to be cumulative it is possible to calculate the relative error $|\delta T/T|$ and $|\delta\epsilon/\epsilon|$ and assuming that $|\Delta^*| \ll |\Delta_0|$ it is possible to make following the approximation:

$$\left|\tfrac{\delta T}{T}\right|_{max} \approx \frac{|K_{1T}K_{2\epsilon}\delta_{1T}| + |K_{1\epsilon}K_{2T}\delta_{2T}| + |K_{1\epsilon}K_{2\epsilon}|(|\delta_{1\epsilon}| + |\delta_{2\epsilon}|)|\epsilon/T|}{|\Delta_0|} \ , \tag{3.86}$$

$$\left|\tfrac{\delta\epsilon}{\epsilon}\right|_{max} \approx \frac{|K_{1\epsilon}K_{2T}\delta_{1\epsilon}| + |K_{1T}K_{2\epsilon}\delta_{2\epsilon}| + |K_{1T}K_{2T}|(|\delta_{1T}| + |\delta_{2T}|)|T/\epsilon|}{|\Delta_0|} \ . \tag{3.87}$$

The above are valid when $1/(\Delta_0 + \Delta^*) \approx (1 - \Delta^*/\Delta_0)/\Delta_0$ and when the small terms of order $\delta_{ij}\Delta^*/\Delta_0$ are neglected. The relative error in the above approximation can be estimated to the first order as

$$\frac{|\Delta^*|}{|\Delta_0|} \ , \tag{3.88}$$

with

$$|\Delta^*| = |K_{1T}K_{2\epsilon}|(|\delta_{1T}| + |\delta_{2\epsilon}|) + |K_{1\epsilon}K_{2T}|(|\delta_{1\epsilon}| + \delta_{2T}|) \ . \tag{3.89}$$

In the system described in this thesis the maximum error in measuring the Bragg wavelength can be assumed to be the same for both peaks and equal to $|\gamma|$; then the maximum relative errors in T and ϵ can be estimated as

$$\left|\tfrac{\delta T}{T}\right|_{max} \approx \frac{|K_{1T}K_{2\epsilon}| + |K_{1\epsilon}K_{2T}| + 2|\epsilon/T||K_{1\epsilon}K_{2\epsilon}|}{|K_{1T}K_{2\epsilon} - K_{1\epsilon}K_{2T}|}|\gamma| \ , \tag{3.90}$$

$$\left|\tfrac{\delta\epsilon}{\epsilon}\right|_{max} \approx \frac{|K_{1\epsilon}K_{2T}| + |K_{1T}K_{2\epsilon}| + 2|T/\epsilon||K_{1T}K_{2T}|}{|K_{1T}K_{2\epsilon} - K_{1\epsilon}K_{2T}|}|\gamma| \ . \tag{3.91}$$

These equations above are used to estimate the maximum error of the system due to significant error in the transfer matrix (i.e. the error in the coefficients relating strain and temperature to change in wavelength.)

The test cases considered are when the error in the matrix coefficients is 0.5% and 1%. The strain bias is $1000\mu\epsilon$ and the temperature bias 100°C.

3.8 Metal Coating

A metal coating on the fibre is desirable for two reasons; firstly the coating increases the strength of the fibre and thus decreases the chance of it being damaged, secondly under neutron bombardment it does not cause extra damage to the fibre unlike acrylate and polyamide coatings, see for example damage due 14MeV neutrons and Co-60 gamma rays caused to acrylate coated fibres [67] and the effects of gamma radiation on polyamide and aluminium coated fibres [95].

3.8.1 Background

A number of types of metal and metal alloys have been successfully deposited on optical fibre. Pure metals include aluminium, copper, gold, nickel [96] and silver; alloys include CuBall (from Oxford Electronics) [97] and a copper alloy (from IVG Fibre) [98]. There are a number of methods to coat the fibres, they come under two main categories; electrolytic deposition and non-electrolytic deposition. Electrolytic deposition is the process by which the fibre becomes the cathode in a metal salt solution containing ions of the metal that is desired to be deposited. The metal ions (positively charged) are attracted to the electro-negative fibre and undergo an oxidation reaction and gain electrons before being deposited on the fibre. To maintain charge balance within the solution metal ions must be added from a sacrificial piece of metal that is connected to the anode of the current source.

Non-electrolytic methods can include chemical deposition, for this method the fibre is dipped in a bath of chemicals and metal ions are oxidised onto the surface; another method is to use vapour deposition whereby the metal is heated into a vapour and on contact with the fibre cools and sticks to the fibre. With both of these non-electrolytic techniques the thickness of deposited layers is quite small; however the CuBall and IVG Fibre both have created a solution whereby a thick layer of copper is applied on top of a thin layer of carbon. To deposit electrolytically it is necessary to first deposit a thin conductive layer onto the fibre using either of the non-electrolytic techniques.

In [99] FBGs are coated in zinc and copper for an application to cryogenic environments. The coating enhances their temperature sensitivity and along with their inherent EMI resistance are perfect for temperature measurements in very low temperatures. Here vapour deposition of aluminium is used to create a base layer for the electro-plating of copper or zinc. They show that the optical properties of the grating reflection are affect by both the deposition the metals. The aluminium affecting both the peak width and peak position, with zinc deposition shifting the peak position and a copper coating enlarging the peak width.

[100] here the work of [99] is extended for further tests; however the copper coating of the sensor is performed differently, only the of the fibre containing the sensor is coated and this is done by dipping the fibre sensor is melted zinc and pulling free. The more standard technique of electrodeposition is used for the copper (the melting point of copper being 1356 K). They demonstrate that at low temperatures zinc exhibits the better temperature sensitivity (as compared to copper coated and bare sensors).

3.8.2 Effects on FBG sensitivity

There are three useful parts to [101] (a further development of their previous paper [102]), first it describes a set of thermal-strain models for metal coated fibres, second it describes a set of metal coating methods, and thirdly it describes a method for embedding an FBG in type No. 45 matrix steel.

Using the thickness of the different coating layers as variables they were able to calculate likely thermal stress coefficient. From their calculations there is an inflection point around about which it is possible to see the changes effect of differences in the thickness of the coatings. When the second layer is thinner than the first layer the thermal stress coefficient increases, when the second layer is thicker than the first then the thermal coefficient decreases. For each first layer thickness there is a point beyond which a thicker second layer has little effect.

Although this paper gives a good description of the chemicals required to perform the various types of plating it does not specify the cleaning and fibre surface activation technique employed. From experience this process is critical to the successful plating of the first and subsequent metal coatings. Detailed descriptions for the chemical methods for electroless copper coating and electroplating of nickel are given. However the physical set-up of how this is performed is not given and from the given figures it would appear that only a short section of fibre is coated in metal with the FBG some where towards the end of this. This means that each FBG would need to be coupled separately onto a main fibre if multiplexing was to be implemented. It is not desirable to have couplers within the radiation zone of a fusion reactor as they degrade with exposure.

The method of embedding requires there to be a bottom to the hole drilled in the metal piece. This means that metal piece which is then filled with a brazing filler, melted then the fibre sensor is inserted. This technique is not useful for the proposed application in this thesis, but could have application to other parts of the nuclear fusion reactor if a suitable FBG is used.

The thermal performance of an FBG coated in lead solder is demonstrated in [103]. Here the fibre was placed in a u-shaped aluminium trench and then filled with lead solder; this created a cylinder of lead 4mm in diameter around the FBG. On testing it was found that the temperature sensitivity of the grating had increased by 4.8 times. This method is completely unsuitable for the proposed application in this thesis due to the low melting point of lead solder ∼183°C [104].

A further method using sputtering and electroplating to coat the fibre is demonstrated in [105]. Here a thin layer of titanium is sputtered onto the bare fibre with a further thin layer of nickel sputtered on top of this. The fibre is then bathed in a nickel sulphamate bath where a thicker layer of nickel is electroplated on top of the thin layers. This sensor is then embedded into stainless steel using a laser assisted metal deposition. This method is a suitable option, however the expensive equipment required was beyond the available funding.

3.9 Metal embedding of optical sensor

The nuclear vacuum environment for this proposed sensor requires that the sensor be adequately protected from being damaged by physical shocks or human/robotic contact during installation and testing. One method of achieving this is to embed the sensor within a metal slab using a metal solder/braze.

3.9.1 Background on metal embedding

The encasing of optical fibres into concrete structures for long term strain monitoring has been one of the major themes of optical fibre sensor research. This has led to the investigation of embedding sensors in other materials including (but not exhaustive), carbon fibre composites, layered materials and metals (base and alloy [96].

The embedding of fibres in metal leads to exciting new applications of the sensors to places previously too chemically harsh or mechanically rough for exposed sensors to operate in. Metal embedded sensors are also more versatile as it will be possible to weld the metal encasement to all manner of metal structures. The main challenges to embedding optical fibres in any material is their fragility, small size and dielectric nature.

Fibres have previously been embedded using a variety of methods, including uncoated bare fibre, strain relieving tube, laser deposition, and metal coated fibre. The bare fibre case is only possible for low melting temperature metals such as aluminium as the fibre is not too highly strained at the melting point temperature and therefore does not break. The strain relieving tube technique involves placing the fibre to be embedded in a thin metal tube of the same or similar metal to the substrate, this tube prevents excessive strain being placed on the fibre as it is being heated and embedded [103].

Laser ablation is a useful technique for embedding the fibre in steel alloys which do not have a suitable brazing material available. In this technique a fibre is layed in a groove of the steel piece then metal is ablated from above using a high power laser. This metal solidifies on top of the metal coated fibre sealing it in position and thus embedding it [105].

Direct embedding of a metal coated fibre is very useful as the metal coating itself assists in the embedding process in two main ways by providing strain relief to the fibre during the heating/ cooling phases, it also gives better adhesion between the fibre faces and the metal surface.

Before metal embedding of fibre optical sensors was fully realised various innovate packages were created to protect the sensors and allow them to be integrated within environments they would otherwise have to avoid. An example of this is shown in [106] where the sensor is encased in epoxy within a PTFE tube all enclosed by a steel tube. This is not suitable for the proposed environment because the plastic and epoxy will degrade with radiation exposure, releasing carbon compounds into the atmosphere; such compounds could interfere with the reactor operation. A better solution is to use a sensor embedded only in metal alloys. These will be discussed below.

The basis for using silver as a base metal for the embedding work comes from [87] that is based on [96]. In this article *Sandlin et al* outline a method for embedding a FBG within Inconel 600 successfully. The detail of this work is found in [107], here a silver based brazing paste is used to embed the sensor. A vacuum furnace is used and the process takes a long time ~ 1 day to complete. They also describe the wavelength shifts that occur when a sensor is embedded due to the strain induced on the fibre as the metal surrounding it cools. This is an important consideration when considering a full system design and the desired operating wavelengths.

In [108] a FBG is embedded within a metal structure with a vacuum sputtered titanium as the base metal on the fibre and a thicker layer of nickel electro-deposited on top. They demonstrate that a 100% increase in the temperature sensitivity of the FBG is realised after embedding. This is because the fibre's coefficient of thermal expansion is far exceeded by the metal's and thus, with good surface adhesion, the FBG responds with the metal to temperature changes. The drawback for this technique is, however, that the thermal inertia of the surrounding metal prevents the embedded sensor responding as quickly as a surface mounted FBG would.

In [99] FBGs are coated in zinc and copper for application to cryogenic environments. The coating enhances their temperature sensitivity and along with their inherent EMI resistance are perfect for temperature measurements in very low temperatures. Here vapour deposition of aluminium is used to create a base layer for the electro-plating of copper or zinc. They show that the optical properties of the grating reflection are affect by both the deposition the metals. The aluminium affecting both the peak width and peak position, with zinc deposition shifting the peak position and a copper coating enlarging the peak width.

[100] here the work of [99] is extended for further tests; however the copper coating of the sensor is performed differently, only the of the fibre containing the sensor is coated and this is done by dipping the fibre sensor is melted zinc and pulling free. The more standard technique of electrodeposition is used for the copper (the melting point of copper being 1356 K). They demonstrate that at low temperatures zinc exhibits the better temperature sensitivity (as compared to copper coated and bare sensors).

A super-structured FBG is proposed and demonstrated in [109]. This grating has a periodically varying coating of silver applied by laser-assisted maskless microdeposition (LAMM) a variation on the laser direct write (LDW) method. Silver nano-particles are deposited layer on layer, after the sputtering of a layer it is sintered in a microfurnace or by using a high power laser. These super-structure FBGs are based around extra long gratings and as such are not suitable for embedding in the method suggested in this thesis.

In [110] a dual temperature-strain sensor is proposed and demonstrated. This sensor is based on a superstructure FBG; in this set-up the fibre containing the FBG is coated periodically in nickel, this builds up a cladding based FBG. Although this is an interesting technique the length of the sensing elements mean it will be difficult to make a point measurement using this package. If there is temperature gradient across the length of the sensor then it will not give an accurate point measurement. This paper also describes a method for calibrating the sensors using a micrometer stage, force sensor and high temperature air. This allows the simultaneous controlled application of strain and temperature to the sensor package for calibration purposes.

A copper/nickel coated FBG sensor is developed in [102]. Here copper was deposited electrolessly allowing nickel to be deposited using electroplating; however nickel coating requires the solution to be kept at a constant temperature of ∼55°C which complicates the process and requires careful control throughout the coating process. The paper also compares a nickel only sensor created using an electroless nickel deposition process before thickening the coating using electro-plating. The sensors were tested between 30°C and 100°C. It was found that the Cu-Ni fibre sensor gained a higher temperature sensitivity as compared to the Ni coated sensor (18.56 pm/°C against 18.15 pm/°C). Further the Cu-Ni sensor had better repeatability of calibration.

3.9.2 Theory

The metal components of the sensor package have very different thermal properties as compared to those of silica. For example the thermal expansion coefficient of steel is around $17.3 \times 10^{-6}{}^{\circ}\mathrm{C}^{-1}$ whereas silica has one around $0.55 \times 10^{-6}{}^{\circ}\mathrm{C}^{-1}$ depending on the precise composition The process of heating up and cooling down means that at the start of the process the fibre is in thermally, but not mechanically coupled to the surrounding metal; however once the solder has reached it solidus point at around 650°C then the fibre and solder are in mechanical contact and the larger thermal expansion coefficient of the solder will dominate. To calculate the wavelength of the grating after the heating, cooling and embedding process it is necessary to first calculate the wavelength (free space) at 650°C,

$$\lambda_{B1} = \lambda_{B0}[1 + (\alpha_f + \xi)\Delta T] \ , \tag{3.92}$$

where λ_{B1} is the Bragg wavelength at 650°C, λ_{B0} is the Bragg wavelength at the reference temperature (in this case 20°C), α_f is the linear thermal expansion coefficient of the fibre, ξ is the thermo-optic coefficient of the silica and ΔT is the change in temperature (Kelvin or degrees centigrade.)

Using the result from Equation 3.92 , the thermal expansion coefficient of the solder, other data, it is possible to calculate the Bragg wavelength at 20°C after the embedding process,

$$\lambda'_{B0} = \lambda_{B1} + \lambda_{B0}[\alpha_f + \xi + (1 - p_\alpha)(\alpha_L - \alpha_f)]\Delta T \ , \tag{3.93}$$

where $\lambda_{B1}, \lambda_{B0}, \alpha_f$ are as before, λ'_{B0} is the embedded wavelength at 20°C, α_L is the linear thermal expansion of the surrounding metal, p_alpha is part of the strain-optic tensor of the fibre. Then inserting equation 3.92 into equation 3.93 and given that ΔT in 3.92 is equal to $-\Delta T$ in 3.93, then the equation relating the embedded wavelength λ'_{B0} to the original Bragg wavelength λ_{B0} is

$$\lambda'_{B0} = \lambda_{B0}[1 - \Delta T(1 - p_\alpha)(\alpha_L - \alpha_f)] \ . \tag{3.94}$$

Using 3.94 it is possible to calculate the embedded Bragg wavelengths without an intermediate step.

3.9.3 Possible methods

Open air furnace heating

Initially open furnaces of the design pictured in Figure 3.12 were considered for the manufacture of the sensor package. However initial tests using CuBall coated fibre with a silver solder test embedded in mild steel showed that there were a number of problems with this approach.

Figure 3.12: Picture of furnace (closed) capable of operation to 1200°C

Firstly the fibre was significantly oxidised in the high temperatures by the ambient air; secondly the mild steel was oxidised significantly even after only approximately 30 seconds of exposure to the high temperature atmosphere; thirdly the positioning and restraint of the fibre during the heating operation was difficult and would not be improved without significant engineering effort and material expense. Thus the heating system must satisfy the following criteria:

- atmosphere must be inert or a vacuum
- it must be possible to monitor the transmission characteristic of the fibre during the embedding process
- heating must be rapid and temperature reached in short time
- positioning and restraint of the fibre within the groove of the metal piece must be easily attained

Inert gas furnace heating

A possible system that satisfies the first two criteria expressed in 3.9.3 is a tube furnace with a sealed stainless steel retort containing the workpiece lying on a ceramic shelf. The retort would have an inlet to allow inert argon gas to pass over the workpiece during the heating process, and an outlet to expel the air inside to start with. This design is shown in Figure 3.13. This method is not considered further due to foreseen difficulties with securing the fibre, sensor, metal slab and solder in an accurate and repeatable manner during the heating process.

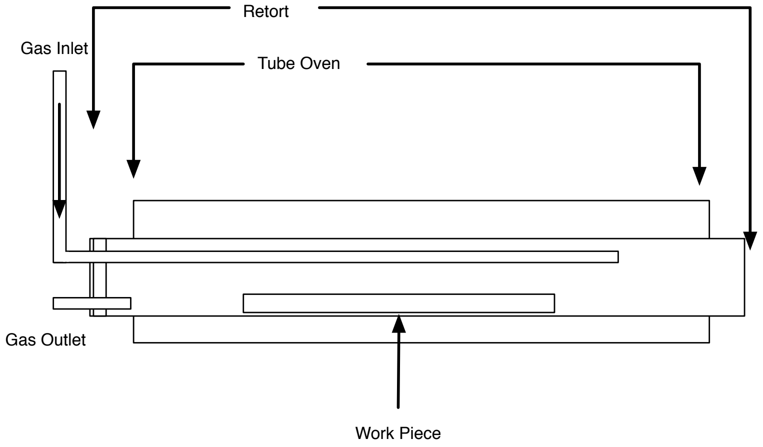

Figure 3.13: Illustrated diagram of a tube furnace with enclosed retort

Induction heating technique

This heating method uses electromagnetic waves in the RF part of the frequency spectrum that are transmitted from a coil surrounding the piece to be heated which induces eddy currents on the surface of ferrous metals.

Physics of Induction Heating When a ferrous metal piece is subjected to a varying electromagnetic field produced by an induction coil the piece heats up due to eddy currents induced on the surface of the piece [111]; this is known as inductive heating and has many applications in industry [112]. The system of equations used to relate induced heating with current and frequency is give by,

$$\omega\sigma(T)\mathbf{A} + \nabla \times (\mu^{-1}\nabla\mathbf{A}) \, , \tag{3.95}$$

$$\rho C_p \frac{\partial T}{\partial t} - \nabla \cdot k\nabla T = Q(T, \mathbf{A}) \, , \tag{3.96}$$

where ρ is the density, C_p is the specific heat capacity, k is the thermal conductivity, Q is the inductive heating, T is the temperature, t is time, (A) is the electromagnetic field, k is the heat conductivity, and ω is the frequency of the current, ∇ is the three dimensional vector of partial derivatives, and μ is the magnetic permeability of the material.

Induction coils can be designed in many different ways; from a traditional coil to a single loop that encloses the whole work piece at once, see Figure 3.14.

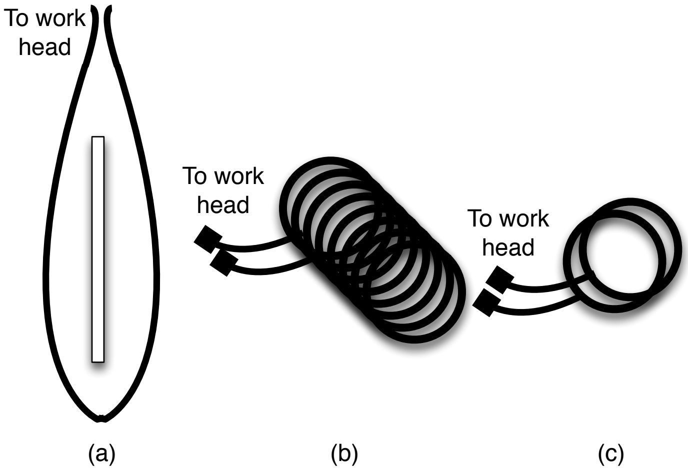

Figure 3.14: Example coil designs; (a) flat single loop design, connection at one end, (b) multiple turns coil with connection in middle, (c) single loop design perpendicular to the material being heated

Although simulations of the multi-turn coil indicated that the stresses on the fibre during the heating and cooling phases of the manufacturing process indicated that the fibre would survive. However, after a number of initial trials using the multi-turn coil it was found that this was not the case and that the fibre was prone to snapping or bending during the heating and cooling process. Hence the single loop design was trialled and was found to be much more successful. It is the experiments performed with this coil that are considered further in this thesis.

3.10 Summary

This chapter has described

- the operating characteristics of FBGs;
- the effects of elevated temperatures and ionising radiation on FBGs;

- that chemical composition gratings should be able to survive within an ionising radiation environment;
- the benefits of metal coating and embedding;
- an error analysis of simultaneous measurement of strain and temperature using dual wavelength gratings;
- possible operational scenarios for FBGs within the nuclear power plant environment;
- possible methods for metal coating the FBGs;
- possible methods for imparting multiple metal coatings onto the FBGs;
- possible methods for embedding the optical fibre sensor within a solder;
- reasons for selecting induction heating as the method of embedding the fibre.

- The fibre Bragg grating should be metal coated to protect the FBG both from physical shocks and from degrading quickly due to diffusion.
  - A number of methods for metal coating were described. The method whereby the fibre is coated whilst being drawn during manufacture is the one which leads to the most strength being retained
  - Metallised fibre made in the above method is available with a copper coating. This exhibits reasonable transmission properties and is compatible with the silver solder used in the embedding.
  - To put the FBG in the metal coated fibre, the fibre must be stripped bare, the FBG written and then recoated using silver deposition with a copper over layer.
- The metallised FBG should be embedded in a metal piece to allow welding to the device being monitored
  - A number of methods of attaching an FBG to a piece of metal and then covering the FBG were described

  - Vapour deposition of steel on top of fibre sitting on a piece of steel
  - Vacuum brazing of the solder/ fibre/ steel combination
  - Furnace heating of the solder/ fibre/ steel combination
  - Heating inside a retort filled with a Noble gas
  - Induction heating of the solder/ fibre/ steel combination

The operating characteristics of the sensor will be used to create a measurement system that can take the wavelengths of the two peaks and calculate the change in strain and temperature.

This chapter has shown that the effect of elevated temperatures and ionising radiation on the FBGs, specifically of the CCG type, and associated changes in peak can be calculated and used to correct the temperature and strain measurements.

This chapter has outlined how the CCG or a regenerated FBG sensor can survive ionising radiation long-term and can be used in the hostile environment of a nuclear fusion reactor's support structure.

Metal coating and embedding have been shown to increase the temperature sensitivity of the CCG and make it more resilient to breaking.

The error analysis of the dual-wavelength measurements has shown that the peak wavelength measurement system must be accurate to at least 1 pm and this will be the specification for the design of the spectrometer part of the system.

Chapter 4

System Design

This chapter describes in technical detail the components required for the development of the specific wideband fibre Bragg grating based sensor system. Furthermore an analysis of the errors from each component will be presented.

4.1 Introduction

A fibre Bragg grating sensor system requires the following major components: an optical source, wavelength discriminating component, sensors, detection system (including software), and a wavelength compensation system this is summarised in Figure 4.1. Each of these components and their subsystems are described below. The choice of each component is made by taking into account accuracy, reliability and cost.

4.2 Optical Source

For this work a super-luminescent diode (SLD) [113] was chosen as the light source. This source was chosen as it combines the benefits of a light emitting diode (LED)

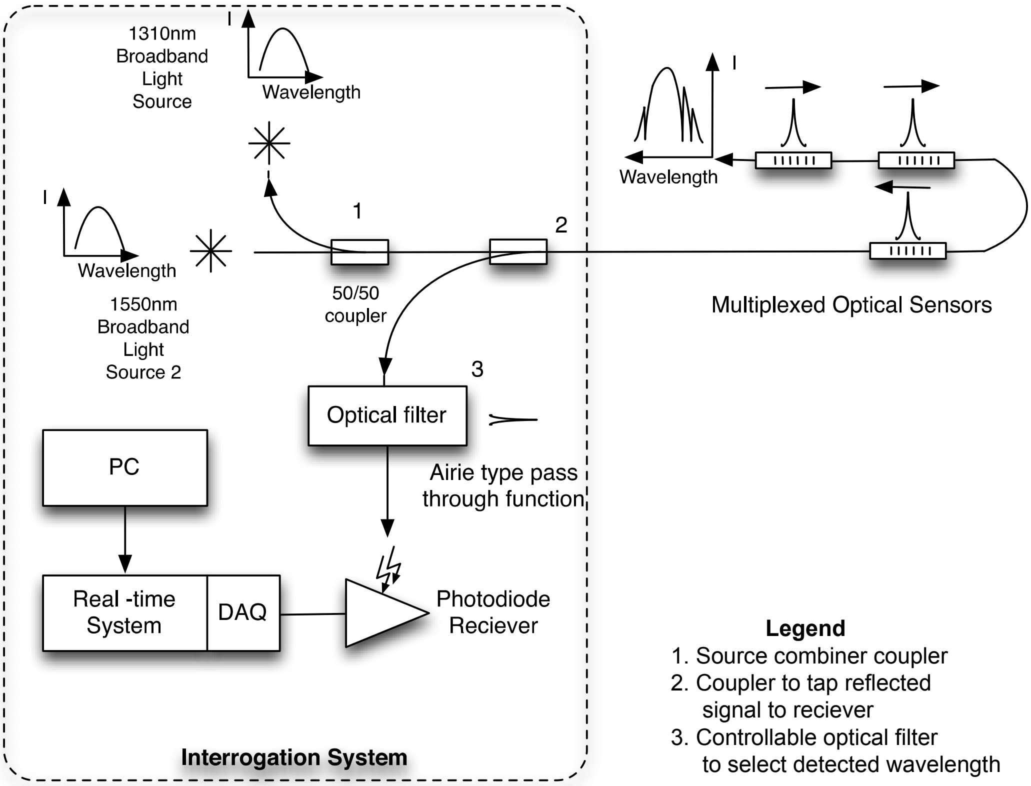

Figure 4.1: Basic operation of a multiplexed fibre Bragg grating sensor system.

with its wide optical bandwidth and the high power of a laser diode [114]. They are also consume low levels of power and can be flexibly controlled in terms of power output by adjusting the electrical current supplied to them.

These SLDs provide a bandwidth of around 40-60nm depending on the optical band and power selected and they are available in a selection of wavelengths including the 1550nm and 1310nm bands.

In Figure 4.2 and Figure 4.3 the transmission of the SLDs used in this particular system can be seen. The SLDs are being supplied with their maximum rated current of 250 mA giving a nominal optical power output of 5 mW.

An SLD is an edge-emitting semiconductor light-source as it generates light along the plane of the diode junction. Superluminescence is also known as amplified spontaneous emission (ASE) [115]. ASE based systems have low temporal coherence, i.e. they have short coherence times and lengths; however for this application, with measurements being dependent on wavelength only, the coherence length is of little significance.

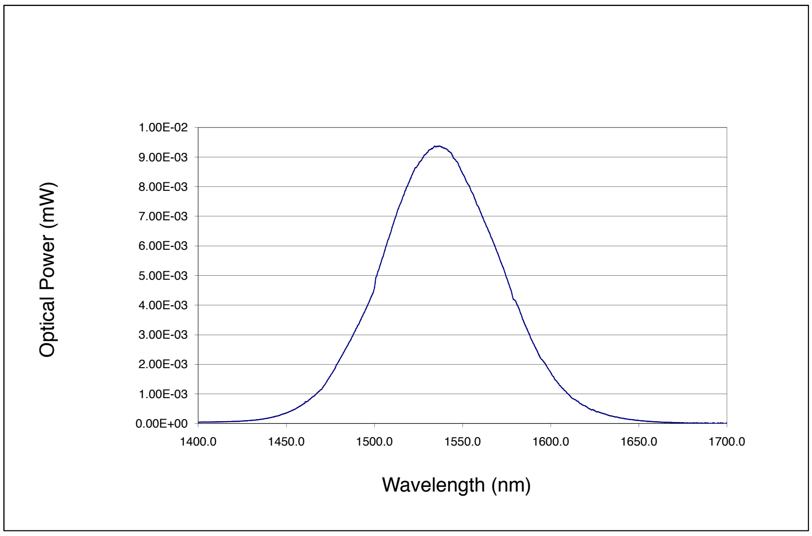

Figure 4.2: Plot of full power optical output from 1550 nm SLD with input current of 205mA measured using optical spectrum analyser (blue line)

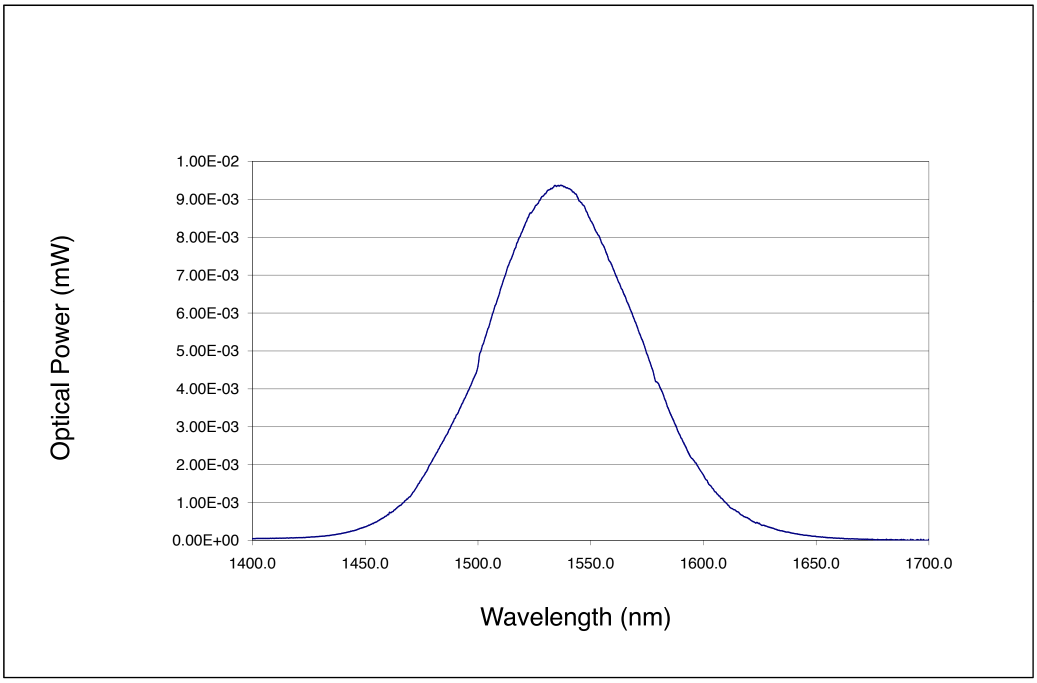

Figure 4.3: Plot of full power optical output from 1310 nm SLD with input current of 205mA measured using optical spectrum analyser (blue line)

4.2.1 Modelling Optical Sources

It is obvious from Figures 4.2 and 4.3 that the optical power output of an SLD can be modelled as a Gaussian form,

$$P_o = a_f exp - \frac{(x - b_f)^2}{2c_f^2} \tag{4.1}$$

where

$$\begin{aligned} a_f &= \frac{1}{F_w}\sqrt{\frac{-2ln(0.5)}{\pi}}\ , & (4.2)\\ b_f &= \mu\ , & (4.3)\\ c_f &= \frac{-F_w^2}{2ln(0.5)}\ , & (4.4) \end{aligned}$$

where F_w is the full width at half maximum (FWHM) and μ is the peak wavelength.

The 1310 nm SLD can be described by,

$$P_{1310} = 0.02388 \exp\left(-\left(\frac{\lambda - 1312}{31.48}\right)^2\right)\ , \tag{4.5}$$

and the 1550 SLD can be described by,

$$P_{1550} = 9.266 \times 10^{-3} \exp\left(-\left(\frac{\lambda - 1537}{46.94}\right)^2\right)\ , \tag{4.6}$$

where P is the optical power in milliwatt and λ is the wavelength in nanometres. Figure 4.4 shows the optical output of the SLD against wavelength as measured by an optical spectrum analyser (OSA) and also as calculated by Equation 4.5. To check the fit of the model to the data a calculation of the absolute and relative residuals was performed and the results are shown in Figure 4.5. This shows that the model is a good fit in the part of most interest (above the half maximum power) and is not useful towards the edges of the data. This model therefore is useful for work concerning the sensor system as the edges are of no concern and can be ignored as they contain no useful optical power. Further no optical sensors will be constructed to operate in the edge domains.

Thus for any modelling of the sensor system it is appropriate to use a Gaussian model to represent the SLD sources.

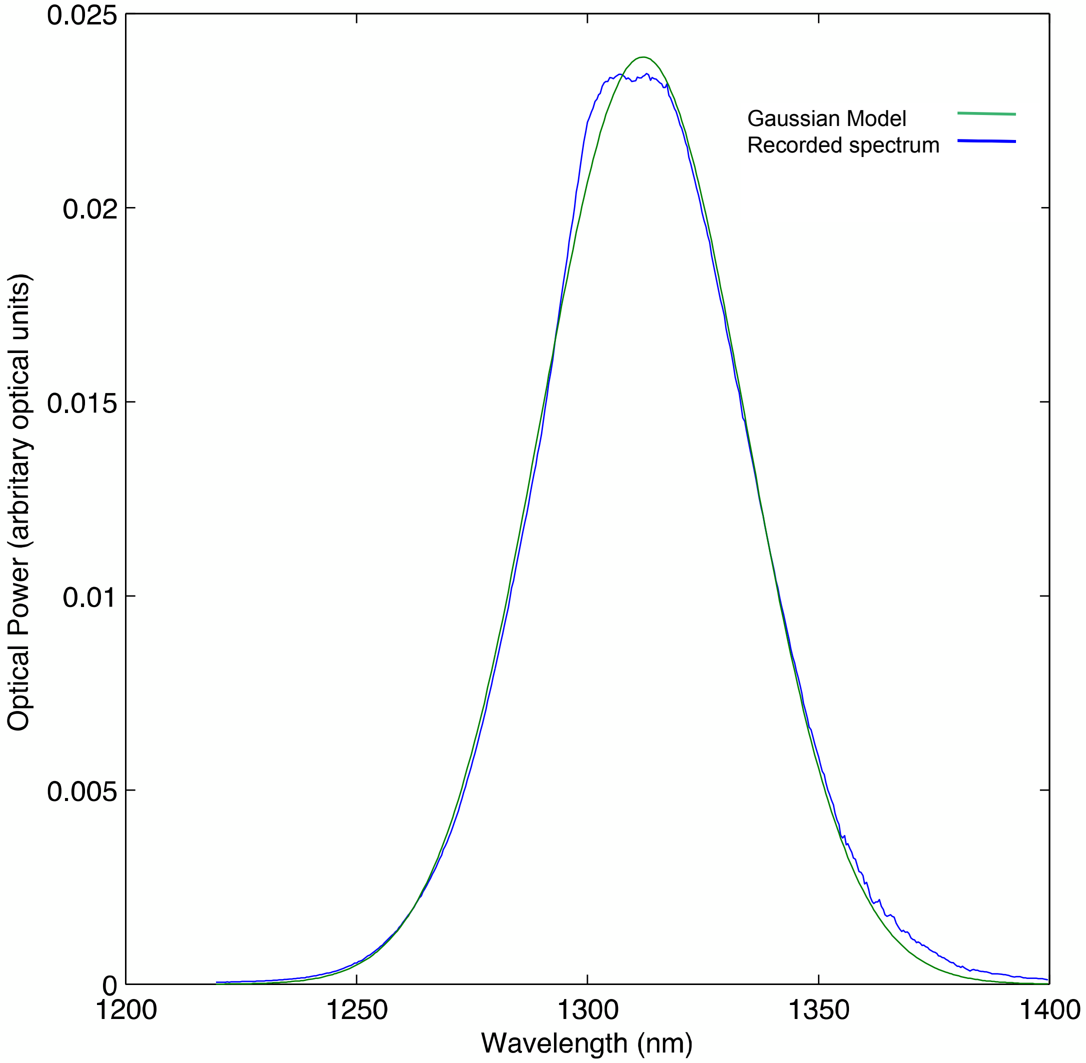

Figure 4.4: Plot of full power optical output from 1310 nm SLD (blue line) with Gaussian model superimposed (green line)

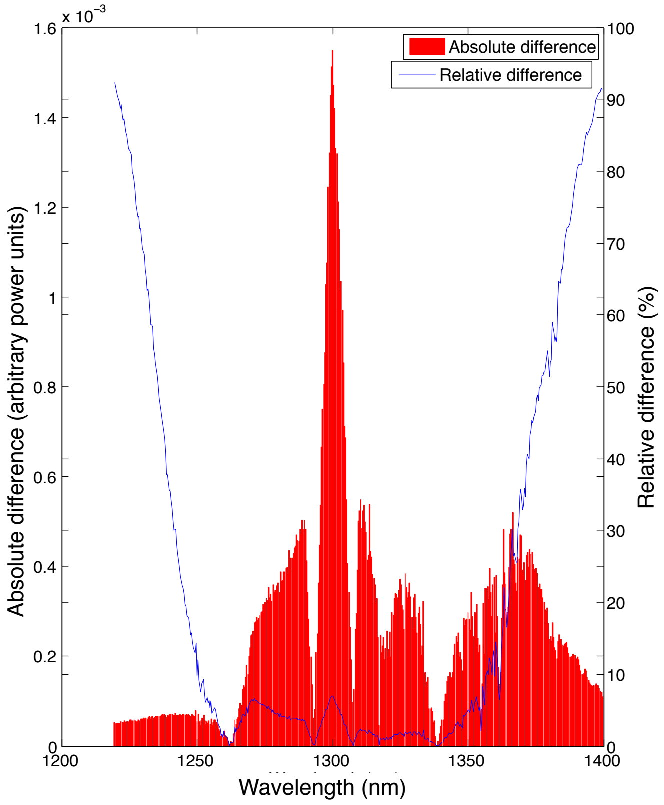

Figure 4.5: Absolute differences between model and data of 1310nm SLD and line plot showing the relative differences.

4.2.2 Data Acquisition Card

The deployed data acquisition (DAQ) board was a PXI-6259 (National Instruments) [116]. The PXI-6259 is a 16-bit DAQ card having 16 analogue inputs with a sampling frequency of 1 MS/s (megasamples per second), split between all inputs and not simultaneous, and 4 analogue outputs (2.8 MS/s). The card has 48 digital I/O lines (5V TTL/CMOS) and two 32-bit, 80 MHz counter/timers. The card also offers analogue or digital triggering. There are 7 programmable input ranges (±100mV to ±10V) per channel.

The card has an analogue input absolute accuracy of 1.920 mV with an analogue output absolute accuracy of 2.080mV. The PXI-6259 bandwidth for small signals (-3dB) is 1.7MHz.

±10V (20V) voltage range of the card was selected as the photodetector offset can be positive or negative. From Section B.2 the following card performance parameters were estimated.

The interval between quantisation levels,

$$q = \frac{20V}{2^{16}} = 305\,\mu V\ . \tag{4.7}$$

The maximum quantisation error,

$$e_{max} = \pm\frac{305\mu V}{2} = \pm 153\,\mu V\ . \tag{4.8}$$

The quantisation noise power,

$$\sigma_e^2 = \frac{(305\mu V)^2}{12} = 93\,nV^2\ . \tag{4.9}$$

The rms value of the quantisation noise is then,

$$\sigma_e = \frac{305\,\mu V}{2\sqrt{3}} = 88.0\,\mu V\ . \tag{4.10}$$

4.3 The Fabry-Perot Interferometer as a Tuneable Filter

A device created from two parallel plates of partially reflecting material and illuminated at near normal incidence is termed a Fabry-Perot Interferometer [90]. The free space optical device consists of two parallel glass or quartz plates separated by a small distance D. The plates are coated on the inner surfaces with a partially reflective coating. When used as a tuneable optical filter the transmitted intensity can be expressed by,

$$I_t(\delta) = \frac{I_i}{1 + \dfrac{4R_m}{(1-R_m^2)}\sin^2\left(\dfrac{\delta}{2}\right)} = \frac{I_i}{1 + F_e \sin^2\left(\dfrac{\delta_e}{2}\right)} , \tag{4.11}$$

where R_m is the fractional reflectance of the mirrors, I_i is the incident intensity, F_e is the finesse of the etalon and δ_e is the optical phase shift and is given by,

$$\delta_e = \frac{4\pi}{\lambda} n_{FP} d_{FP} \cos\Theta_{FP} , \tag{4.12}$$

where n_{FP} is the cavity's refractive index, d_{FP} is the separation of the mirrors and Θ_{FP} is the angle of the transmitted beams with respect to the normal.

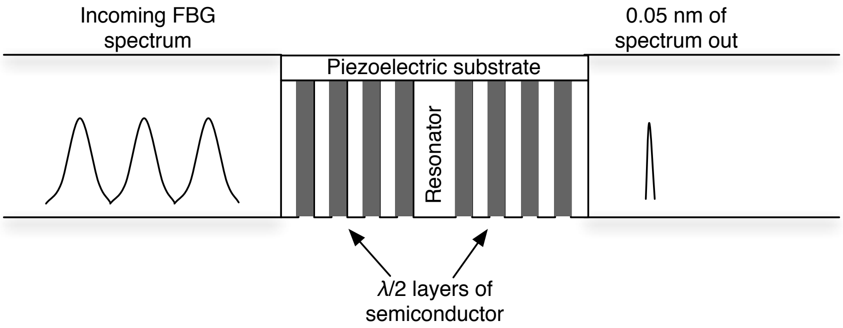

Figure 4.6: Generic layout of an in-fibre Fabry-Pérot filter. Based on the structure shown in [117]

For a single mode fibre based Fabry-Perot sensor $\Theta_{FP} = 0$ and thus is at the maximum order for any wavelength. For a single mode fibre based solution, such as the MicronOptics TF2-FP-9000, a piezo electric substrate with multiple layers of semiconductor is used instead of traditional glass mirrors. This structure is shown in Figure 4.6.

4.3.1 Initial studies of optical filter

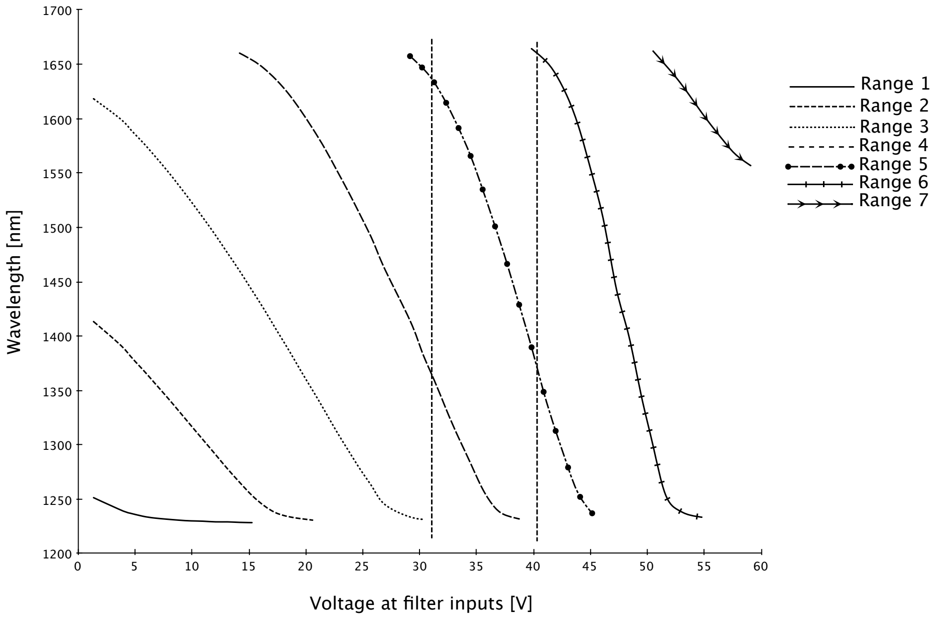

Figure 4.7: Static characterisation of wavelength dependence on voltage input

The filter used in this work was subject to a number of tests and calibrations before being integrated within the interrogation system. The static wavelength response of the filter was measured using the PXI system and filter driver amplifier (described below). 0.33 V steps were used in the characterisation. The results of this work are shown in Figure 4.7.

This characterisation confirmed that the usable range of the filter was from 1280 nm to 1600 nm and that the voltage change required to cover the entire range was <10 V in the static measurements.

Initial experiments with the filter indicated that the wavelength of the peak transmitted drifted with time when a constant voltage was applied. To demonstrate this 30V was applied to the filter and the 1550nm SLD was used as a broadband light source. The transmitted peak was measured using the optical spectrum analyser at different times; the time and position were recorded and plotted in Figure 4.8. The time was recorded manually using the computer clock, this is only accurate to 1s (max) and so the results can only be discussed qualitatively.

In Figure 4.8 it can be seen that there is an initial rapid drift to lower wavelength followed by a much smaller randomly varying drift (10^2 times smaller) that does not vary in magnitude by more than a factor of 2 over the period of the experiment; this is shown more clearly in the zoomed in Figure 4.9. A drift compensation system must be developed for using this filter.

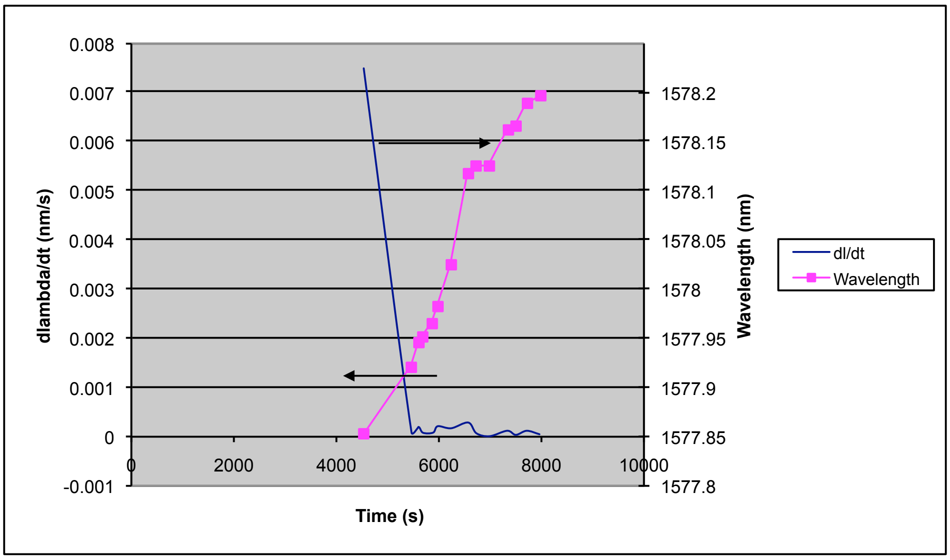

Figure 4.8: Static characterisation of wavelength drift with time

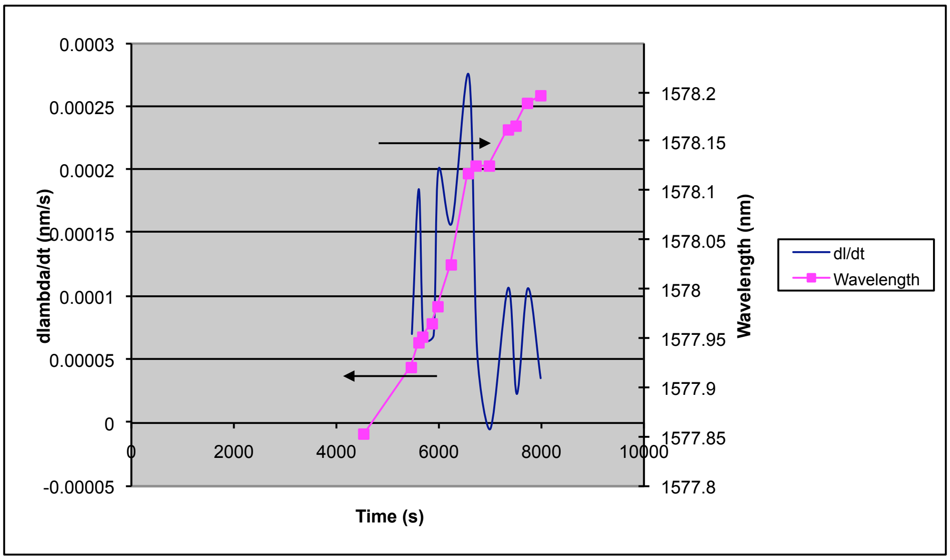

Figure 4.9: Static characterisation of wavelength drift with time looking at the smaller variations

4.3.2 Filter Driver Amplifier

To control the filter a voltage is applied across the input ports of the filter. This voltage is generated by taking an input analogue voltage from the digital to analogue output of a PXI-6059 card (AO1), this is passed through an OP-27 to provide high impedance input to the main amplifier. This is a specialist amplifier sought after discussions with Micronoptics. It operates over an input range of -10V to +10V and can output a voltage in the range 1 to 58V in this application, the amplifier has a slew rate of $5\,V/\mu s$ more information on the high voltage amplifier can be found in citeHighVamps. A wavelength range is given as an initial guess for the system. This defines the mode of operation of the etalon and also the voltage range that is to be used. It is only with the reference gratings that it is possible to actually calculate the true wavelength of the reflected peaks. This uses a pair of linear empirical formulae calculated from a large set of measurements analysed in MATLAB.

4.4 Photodetector Design

The function of a photo-diode in an optoelectronic system is to transform optical power levels into electrical signals. The performance of the photo-diode subsystem is critical to making accurate measurements. The light is received by a photo-diode which acts as a current source by converting the incoming photons into electrons. It is unusual to perform a current waveform to digital waveform transform directly and more usual to convert the current waveform to a voltage waveform that can be sampled by an analogue to digital converter (ADC) more easily.

4.4.1 Design Criteria

Optical signals attenuate over large distances; therefore signal loss compensation is required. Compensation is performed electrically by using a high-gain photodetector circuit. Due to the number of sensors, and the large optical bandwidths, in this system a high sensitivity detector with wide-band operation is required for accurate and fast measurements. Therefore the following properties are required to be exhibited by the photodetector circuit:

- satisfactory gain and high dc stability,
- linear response combined with a relatively high bandwidth,
- low noise and adequate sensitivity.

4.4.2 Photodiode Operation

A PIN (P-type, Intrinsic, N-type of semiconductor doping) diode is a semiconductor device that responds to incident light by producing a current if operated in reverse-bias mode or a voltage if operated in forward bias mode. The physics of the operation of a PIN diode will not be discussed here but can be found elsewhere [118].

To meet the design criteria in 4.4.1 the ETX100 photodiode was selected. This has the following properties:

- Typical responsivity of 0.75 A/W,
- Typical dark current of 0.3nA,
- Capacitance of 1.1pF - giving low noise,
- Typical bandwidth of 1.5 GHz,
- Typical rise time of 250 ps which is sufficient for this speed of interrogation.

Although it has a non-flat response to light input at different frequencies this is of no concern as the sensor is based on wavelength changes rather than intensity changes.

4.4.3 Photodiode amplifier circuit design

Photodiode output signals can be monitored as either a voltage or a current. Better linearity, offset and bandwidth performance is offered by current monitoring [118]. Choosing a photodiode connected to a current-to-voltage (I-to-V) converter based on a transimpedance amplifier configuration allows voltage measurements to be made which are directly proportional to the generated current in the photodiode:

$$E_o = I_p R_f, \tag{4.13}$$

where E_o is the voltage output from the transimpedance amplifier, R_f is the feedback resistor of the amplifier and I_p is the photodiode current related to the optical power by:

$$I_p = \Phi_{pp} R_p \tag{4.14}$$

where Φ_{pp} is the incident optical power and R_p is the responsivity of the photodiode.

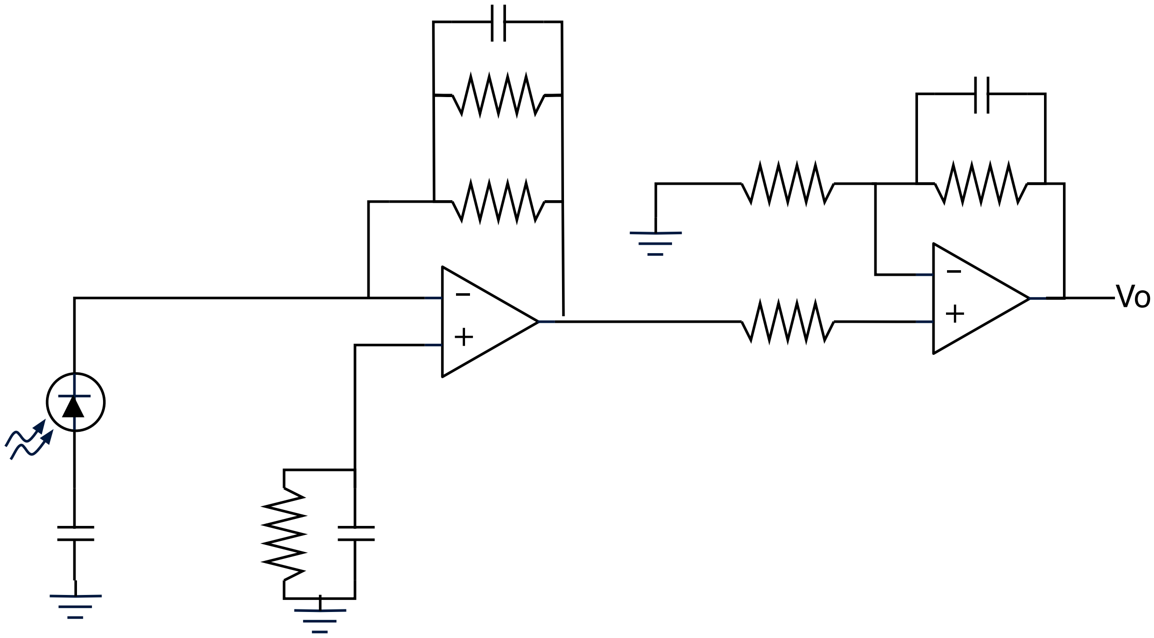

Figure 4.10: Outline circuit diagram of a transimpedance two step current to voltage amplifier

4.4.4 Noise mechanisms in an optical receiver

For a receiver system as shown in 4.10 there are three main noise sources, the shot noise of the photodiode, thermal noise and quantisation noise from the ADC (described above). If a low noise pre-amplifier used has low amplifier current noise (of the order fA) and low amplifier voltage noise (of the order 15 nV/ $\sqrt{\text{Hz}}$, f=1 kHz, shunt resistance = 100 Ω, then the effect of amplifier noise can be neglected.

Noise occurs due to the conversion of photon to charge carriers being a random process inside a photodiode; this noise is called shot noise and is associated with current flow. Thus it is normally modelled as a current source in parallel with the photodiode, with the mean square value given by,

$$I_{sh}^2 = 2eI_{ph}B_{ph} \ , \tag{4.15}$$

where I_{ph} is the average current generated by photons flowing through the photodiode, B_{ph} is the post-conversion electrical bandwidth of the system and e is the elementary charge.

In the system the photodiode is used together with a trans-impedance pre-amplifier, so the shot noise produced in the photodiode is amplified along with the original signal. If A_{sig} is the amplification factor of the pre-amp, then the rms shot noise voltage will be,

$$e_{sh} = \sqrt{2eI_{ph}B_{ph}}A_{sig} \ , \tag{4.16}$$

The thermal noise in the circuit is due to thermally induced charge carriers being created in an electrical resistance element at random. This is due to charge carriers being in a random motion in all resistances at a temperature higher than absolute zero. The amount of motion is a direct function of the absolute temperature of the resistance. It was shown by Nyquist that the circuit rms voltage produced by a resistance R is given by,

$$e_{th} = \sqrt{4K_BTR_fB_{ph}}, \tag{4.17}$$

where K_B is the Boltzmann's constant, T is the absolute temperature in Kelvin and

B_{ph} is the the electrical system bandwidth. In this case the main source of thermal noise is the feedback resistor R_f of the transimpedance amplifier.

4.5 Optical Coupling

If the system suggested by this thesis were to be deployed within a real nuclear fusion reactor then it will be necessary to multiplex the sensors and sensor lines within the reactor environment; this will increase the redundancy of the network [119], minimising down-time and the number of repairs required during operation. The three methods, currently, of multiplexing are,1) the use of an optical switch, or 2) the use of a coarse arrayed waveguide system, with one input and multiple outputs or 3) the use of a wave division mixing system based on fused optical couplers, with one to many (1 x N) or many to many (N x N) options.

Option 1) is unlikely to be used as an optical switch requires a power supply and is relatively bulky; however it could be used at the transceiver of the optical circuit as it offers the best optical power budget. Option 2) requires the use of systems that have yet to be tested in an ionising radiation environment . Therefore option 3) is the most likely to be deployed at this time. In [120] [121] [122] the response of optical couplers that have been exposed to varying types of radiation and doses is reported. [120] covers all the components necessary to build an optical sensor system and considers the effects of radiation exposure when in space and what steps must be taken to mitigate the effects of them, including radiation hardening. The effect of only Co-60 radiation on a variety of single- and multi-mode fused optical couplers was studied in [121]. The couplers were exposed to a total dose of 100kGy demonstrating a range of losses between 0.01 dB and 50 dB. Both extremes of loss were recorded at 850 nm, a wavelength that is not used in the system described in this thesis. Reasonable losses for 1550 nm and 1310 nm were recorded. In [122] various fusion spliced couplers were exposed to gamma and beta radiation from a Co-60 source and the isolation between the channels shown to change by no more than 5.6 dB at the maximum dose of 10 kGy(SiO_2). On the basis of the literature it is possible to infer that the WDM system would work within the nuclear environment of the ITER reactor.

A full working wave division multiplexing (WDM) system is considered and tested under gamma radiation to 100 MGy in [123].

4.6 Optical Power Budget

After outlining the design of an optical fibre system it is necessary to calculate the optical power budget of the system to examine the viability of the suggested system. This is done by adding the losses on entry into components and reflection from interfaces in the system. For example, at each FC/APC connection 0.1dB is lost due to reflections from the interface and also due to coupling into other unsupported modes. Loss values for most components can be gleaned from technical specification documents and are usually given in dB, for discrete components, which is known as the insertion loss for that component and dB/km for the optical fibre itself, referred to as the attenuation of a fibre type.

4.6.1 Losses from the components and connections

The components outlined above all have an associated loss as shown in Table 4.1

Table 4.1: The loss caused by each component in dB[1]

Optical Component	Insertion Loss (dB)
50/50 Coupler	3.01
FC/APC Connection	0.3
Splice Loss	0.2
Tuneable filter FFP-TF2	3.0

---

[1] Losses measured multiple times using an optical spectrum analysers

4.6.2 Losses from transmission fibres

The losses due to transmission through optical fibre of different types is shown in Table 4.2 below.

Table 4.2: Optical power round trip loss from fibre

Optical Fibre	Loss ($\text{dB}\cdot\text{km}^{-1}$)	Length (m)	Total Loss (dB)	
			1550nm	1310nm
SMF 28e at Fibre 1550nm[2]	0.2	200	0.04	-
SMF 28e Fibre at 1310nm[3]	0.35	200	-	0.07
CuBall at Fibre 1550nm[4]	5	50	0.25	-
CuBall Fibre at 1310nm[5]	5	50	-	0.25
CCG fibre at 1550nm[6]	2.7	10	0.027	-
CCG fibre at 1330nm[7]	4	10	-	0.04
Total round trip loss	-	260	0.634	0.72

4.6.3 Optical Power Reflected from CCGs

Using the model equations of the optical sources [113] and that the resolution of the system is nominally 0.1nm then the power reflected in one step from the peaks can be calculated by integrating over 0.1nm as shown below. The correction factor to give the output in mW has been multiplied in and also the 10% reflectance of the grating is accounted for,

$$P_{optical}^{1310} = 0.1 \int_{1309.95}^{1310.05} 0.0896185. * \exp\left(- \left(\frac{(\lambda - 1312)}{31.48} \right)^2 \right) d\lambda \times \, , \tag{4.18}$$

$$= 8.9257 \times 10^{-4}\, mW \tag{4.19}$$

---

[7] [124]

[7] [124]

[7] [97]

[7] [97]

[7] [58]

[7] [58]

$$P_{optical}^{1550} = 0.1 \int_{1549.95}^{1550.05} 0.0604201. * \exp\left(-\left(\frac{(\lambda - 1537)}{46.94}\right)^2\right) d\lambda \; . \tag{4.20}$$

$$= 5.5959 \times 10^{-4}\, mW \; , \tag{4.21}$$

Thus the reflected power from the 1550 nm peak is 893 nW and from the 1310 nm peak is 560 nW.

4.6.4 Total loss and effect

Using the values given in Equations 4.19 and 4.21 it is then possible to calculate the value of the optical power received at the photodiode receiver modules. This needs to be calculated for both the 1310nm band and the 1550nm band as the attenuation of these bands in optical components is different due to the differences in refractive index's dependence on wavelength [48].

This calculation assumes that the worst values for losses are valid from Tables 4.1 and 4.2. For the 1310nm peak the total power received at the photodiode is −84.33 dBm and for the 1550nm peak is −88.92 dBm. This analysis shows that the optical power in both bands will be greater than that required to be detected by the photodiode module.

4.7 Software Design

The control system for the interrogation of the optical signals was created using the Labview software package. The control signal is a sawtooth wave that has a range of approximately 3 V in the PXI domain. The electrical signal from the photodiode must be recorded simultaneously with the control signal step, otherwise there will be a phase difference and this would complicate the recovery of the spectrum. A screen shot showing the layout of front-end of the software is shown in Figure 4.11

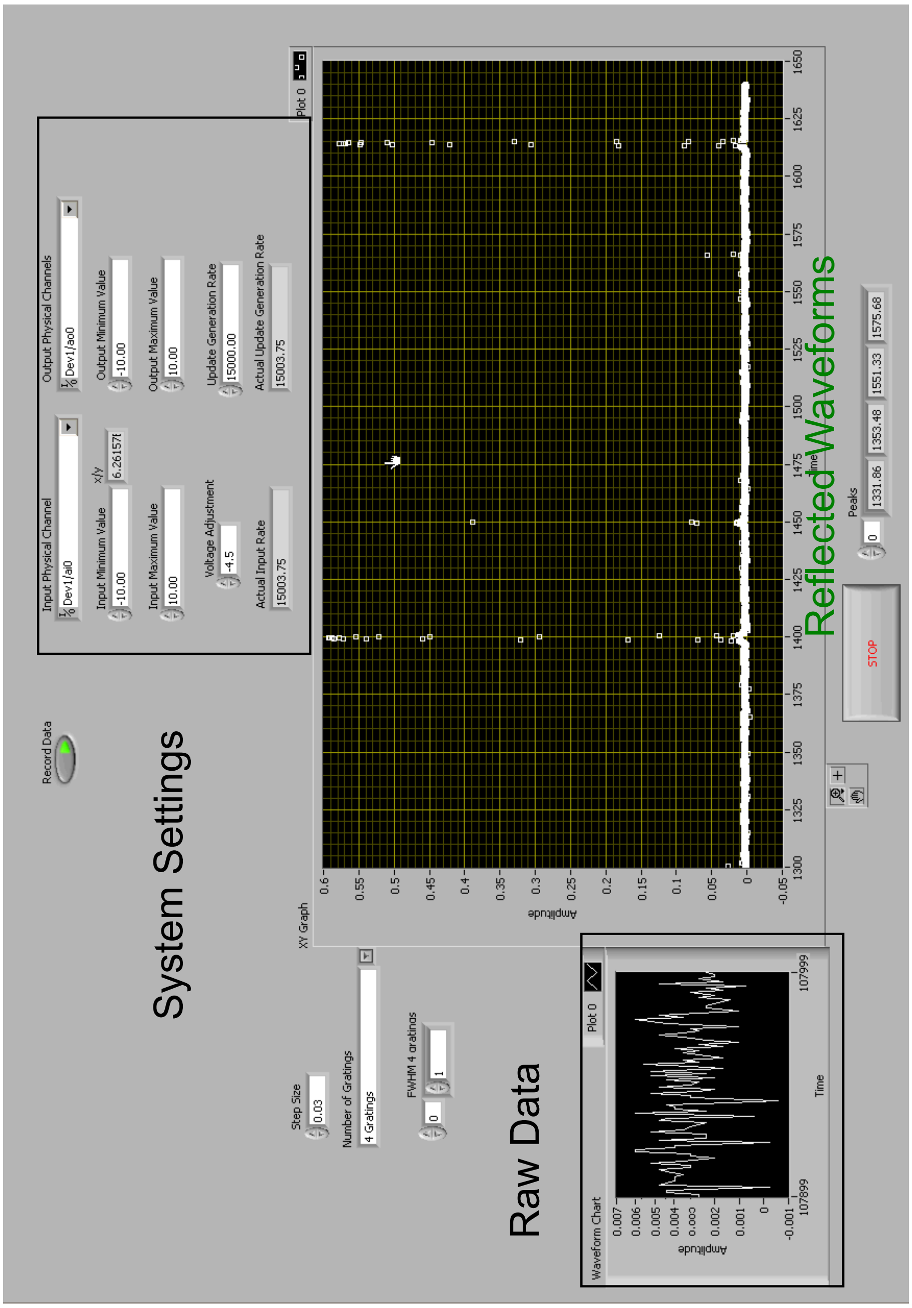

Input Physical Channel: Dev1/ai0

Output Physical Channels: Dev1/ao0

Input Minimum Value: -10.00

X/Y: 6.261571

Output Minimum Value: -10.00

Input Maximum Value: 10.00

Output Maximum Value: 10.00

Voltage Adjustment: -4.5

Update Generation Rate: 15000.00

Actual Input Rate: 15003.75

Actual Update Generation Rate: 15003.75

Step Size: 0.03

Number of Gratings: 4 Gratings

FWHM 4 gratings: 0 | 1

Peaks: 0 | 1331.86 | 1353.48 | 1551.33 | 1575.68

Figure 4.11: Screen shot of the front end for the fibre interrogation system. This shows the different parts of raw data, settings, normalised spectrum of reflected waveforms

4.7.1 Control Signal Generation

The control wave is generated in such a way so to maximise the number of data samples in the wavelength ranges of interest (1280-1340nm and 1525-1580nm approximately); the space between these ranges is of no interest as there is no light being transmitted in this range.

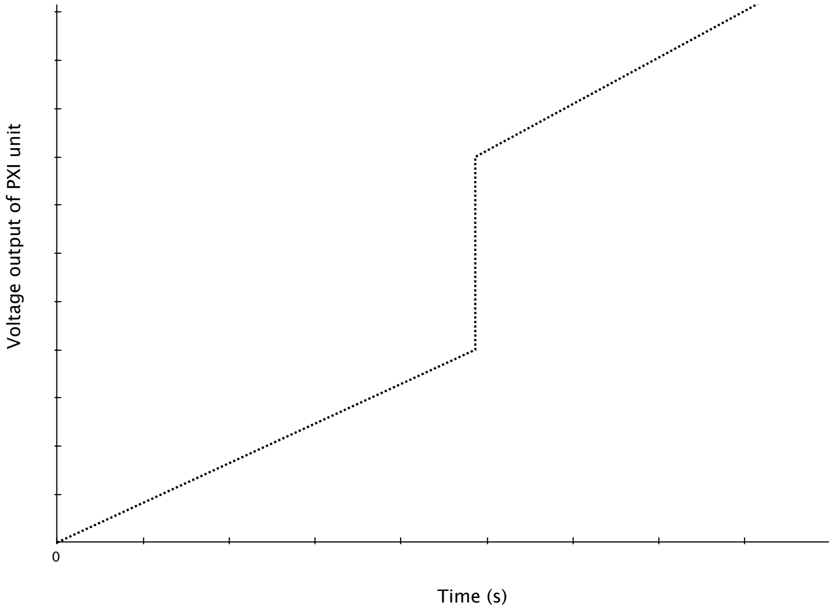

Figure 4.12: Example signal for the control of the optical filter

The control signal formula was found empirically by analysing the results of the static tests of the filter and then some adjustment was performed to correct for the dynamic use of the filter.

The equation that relates the voltage of the filter to the optical wavelength (before correcting for drift) is,

$$\lambda_f = 0.436x^3 - 3.6504x^2 + 77.722x + 1161.7 \ , \tag{4.22}$$

where x is the voltage across the filter input pins and λ_f is the peak wavelength passed through the filter. This was found empirically using the data plotted in Figure 4.7.

The particular data set is that between the two vertical black lines between approximately 33V and 36V in Figure 4.8. The wavelength vs voltage function is plotted in Figure 4.13 and one period of the voltage function is plotted versus time in Figure 4.14. The voltage vs time plot shows where some of the wavelength range is missed out, this is because it lies in the 1400 to 1500nm range, silica has a large absorption band in this wavelength range and thus it is not worth trying to measure any reflected wavelengths in this range.

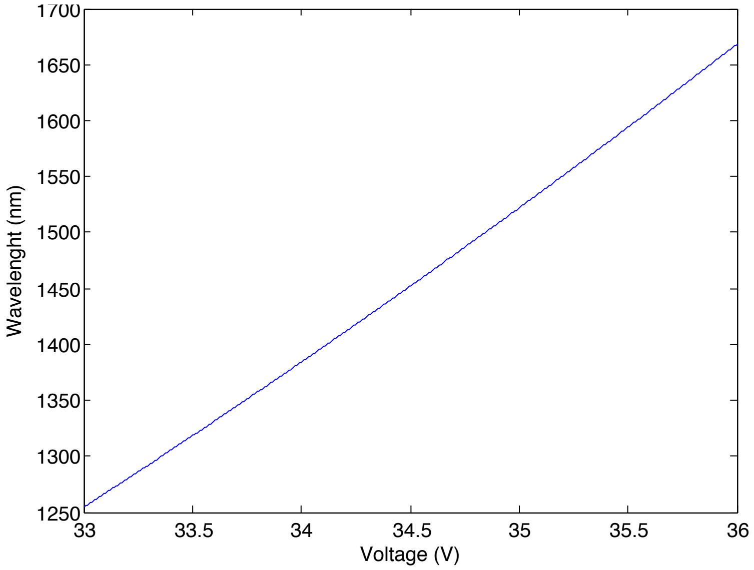

Figure 4.13: Optical filter pass wavelength versus voltage at filter terminals

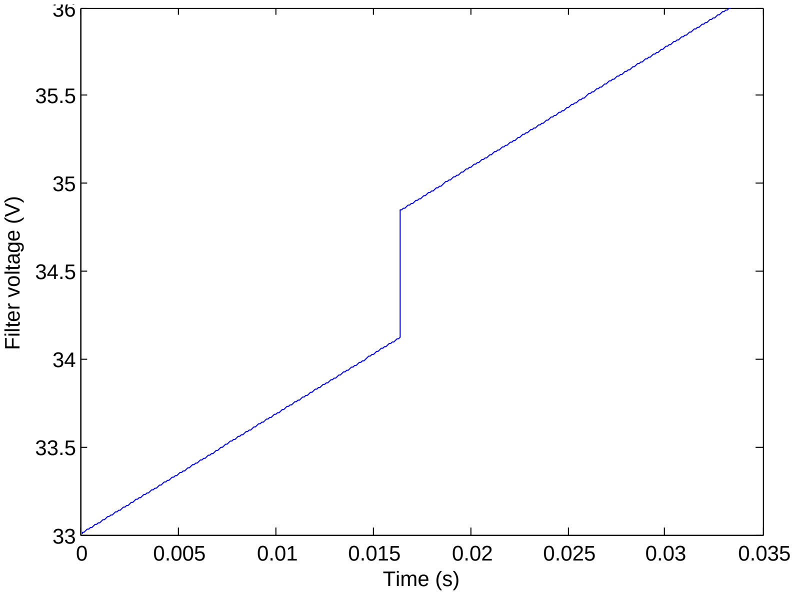

Figure 4.14: One period of the voltage at the filter's terminals against time at 30Hz

The average static drift of the filter is 0.00015 nm s^{-1} so the error per second in the measurement of temperature and strain (due only to drift) at 250°C and under $800\mu\epsilon$ would be (using Equations 3.90 and 3.91)

$$\left|\frac{\delta T}{250}\right|_{max} \approx \frac{|K_{1T}K_{2\epsilon}| + |K_{1\epsilon}K_{2T}| + 2|\epsilon/T||K_{1\epsilon}K_{2\epsilon}|}{|K_{1T}K_{2\epsilon} - K_{1\epsilon}K_{2T}|}|0.00015| \ , \tag{4.23}$$

$$\approx \frac{|10 * 1.2| + |1 * 13| + 2|800/250||1 * 1.2|}{|10 * 1.2 - 1 * 13|}|0.00015| \ , \tag{4.24}$$

$$|\delta T|_{max}^{250°C} \approx 1.2°C \ . \tag{4.25}$$

Thus the maximum temperature error at 250°C is 1.2°C. For the maximum error of the strain a similar procedure is followed with the result being an error of $12.75\mu\epsilon$.

4.7.2 Peak Detection

Two main methods can be used for the detection of reflected FBG peaks, the thresholding method [125] and the double line method [126] . On the basis that the system is similar to that in [126]then the double line method of peak analysis was chosen as it offers a higher accuracy. This method will be explained below. The data is read by a threshold peak detector (built-in to LabVIEW) this identifies the approximate positions of peaks using a preset threshold level. The level is set at approximately the level of the FWHM and can be absolute or normalised. Using these approximate positions two sets of data are extracted for each peak; from these sets the point just above the FWHM level and just below the FWHM level are extracted. A straight line is fitted between these two points and the point where this line crosses the FWHM is determined. This crossing point, λ_1, is averaged with λ_2 to find the peak position. This process is described graphically in Figure 4.15 with a zoomed in look at the straight line fitting shown in Figure 4.16. This method assumes that the peak is perfectly symmetrical, at the level of resolution used in this system this can be taken as true.

This can be expressed mathematically as follows, y_1 and y_2 are the powers of the left and right lines respectively in Figure 4.16,

$$yy_1 = mm_1\lambda + cc_1 \ , \tag{4.26}$$

$$yy_2 = mm_2\lambda + cc_2 \ , \tag{4.27}$$

$$mm_1 = \frac{PP_2 - PP_1}{\lambda_2 - \lambda_1} \ , \tag{4.28}$$

$$mm_1 = \frac{PP_4 - PP_3}{\lambda_4 - \lambda_3} \ , \tag{4.29}$$

$$cc_1 = PP_1 - mm_1\lambda_1 \ , \tag{4.30}$$

$$cc_2 = PP_3 - mm_2\lambda_3 \ . \tag{4.31}$$

Using Equations 4.26 to 4.31 the estimated FWHM value is then inserted into Equations 4.32 and 4.33 to find the λ values for each line at the FWHM. The two resultant wavelengths are then averaged to give the peak wavelength in Equation 4.34.

$$\lambda_1(FWHM) = \frac{P_{1FWHM} - c_1}{m_1} \ , \tag{4.32}$$

$$\lambda_2(FWHM) = \frac{P_{2FWHM} - c_2}{m_2} \ , \tag{4.33}$$

$$\lambda_B = \frac{\lambda_{2FWHM} - \lambda_{1FWHM}}{2} \tag{4.34}$$

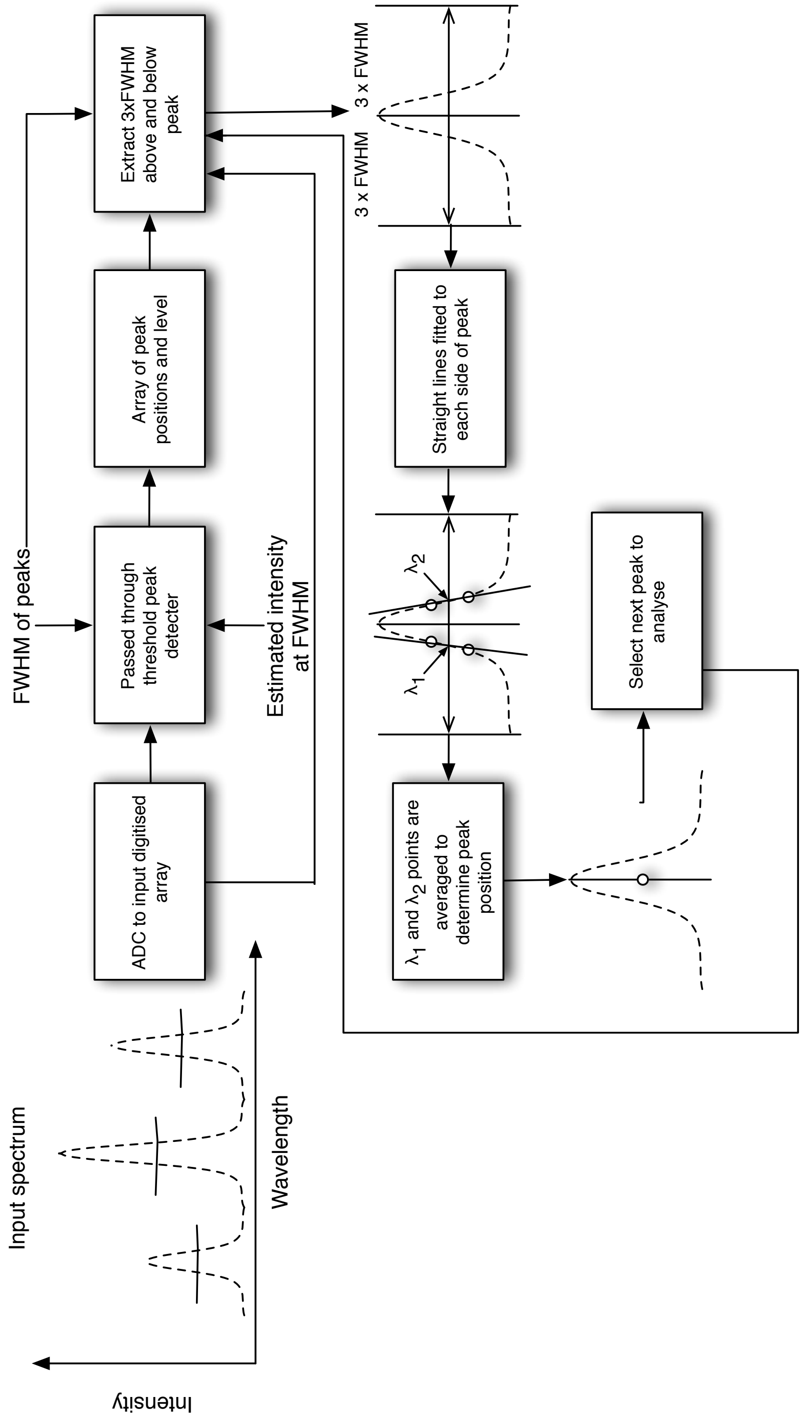

Figure 4.15: Flow diagram of the procedure for peak detection using the double line method.

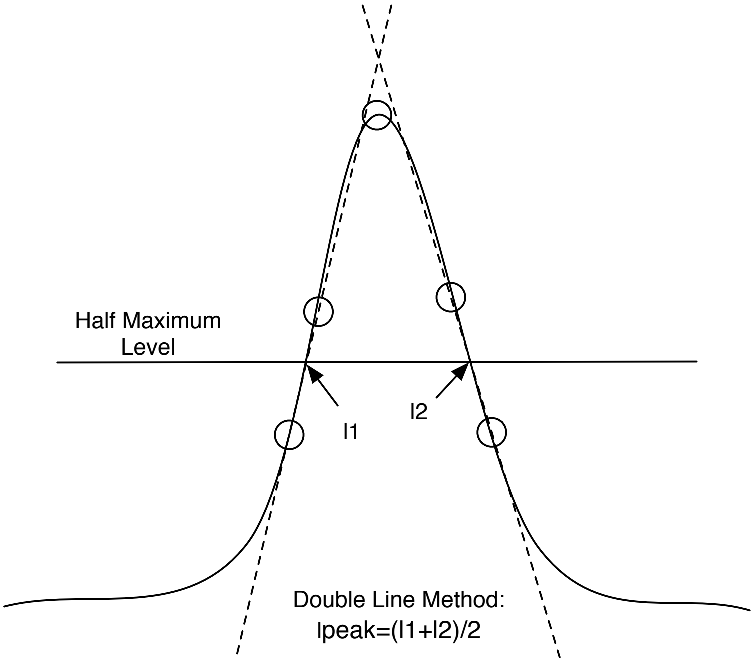

Figure 4.16: Zoomed in view of the fitting of straight lines to the sides of the FBG peak

4.8 Summary

In this chapter the components and design of the fibre optic sensor system used in this research were described.

The following aspects were covered:

- Optical source choices
- Wavelength selection method choice
- Wavelength selection operation
- Optical power budget
- Software design for controlling interrogator and detecting peaks

The system described in this chapter must be calibrated by experimental methods as there are too many unknown variables (filter dynamic response for example) to be determined theoretically.

This calibration is covered in Chapter 6, with Chapter 5 considering the design and construction of the sensor that the described interrogation system will operate with.

Chapter 5

Sensor Construction

5.1 Introduction

In this chapter a detailed description of the sensor package design and manufacture is presented. Firstly the design requirements of the sensor will be outlined and then an initial proposed solution will be specified. The construction process will then be explained in technical detail. In Chapter 3 the temperature and strain characteristics of fibre Bragg gratings along with the reasons why chemical composition gratings were chosen for this particular application; in this chapter the design for the sensor package will be described and analysed in detail in conjunction with the manufacturing process.

5.2 Sensor Package Specification

The sensor design was finalised using an iterative process that took into account the desired operational characteristics and fusion reactor acceptable material properties.

The operational characteristics that must be considered are

- Thermal cycling between room temperature and the maximum of 400°C
- Vacuum atmosphere
- High levels of ionising radiation
- Mechanical vibration

Further only specific materials are allowed inside the blanket of the vessel mainly due to some potential transmuted products from certain elements [29]. E.g., Hydrogen can be produced via nuclear interactions with AISI 316L steel [127]. The hydrogen could build up into an explosive mix, change the plasma properties or cause expansion of pieces of the steel frame if not monitored, these will all cause dangerous operating conditions within the reactor. This is why the designers of ITER must be careful to exclude certain materials from being exposed to ionising radiation.

The sensor must also have no moving parts as it will not be possible to adjust them once it has been put in position within the reactor due to the high levels of radiation. It must also be possible to perform online calibration. This leads to constraints on the type and design of a sensor and its associated packaging.

Previously in Chapter 2 the case for not choosing an electrical or electronic one was presented and that an alternative solution should be sought. It was highlighted in Chapter 3 that an FBG based solution could be used; however, it must be suitably protected for the environment that it is being placed in. For the environment inside an ITER port plug it is envisaged that a weldable steel package containing the fibre sensor connected to armoured optical fibre cables would provide suitable physical protection

The weldable package must either increase or at least maintain the sensitivity of the FBG to temperature and strain changes. A possible package that satisfies all the thermomechanical cycling effects uses ceramic fillers in combination with an epoxy binder to attach the FBG to a metal shim that is then spot welded to a larger piece of steel [128]. This technique would allow the use of different types of metal depending on the application of the sensor (with suitable calibration for each type of metal); however epoxies and fillers have been shown to degrade and change under ionising radiation[28]. This means that the sensor package must not use epoxies to be able and thus the package created in [128] cannot be used in nuclear facilities.

5.3 Experiments

5.3.1 Experimental set-up

The use of the small coil necessitates a change in the set-up of the fibre/metal position equipment. For this method the steel piece was placed a top a piece of alumina on two aluminium legs. This raised the steel/solder combination to approximately the height of a pair of three dimension adjustable micrometer positioners. The copper coated fibre was laid in the groove of the steel piece then into the machine grooves of the positioners and powerful magnets applied over the fibre on top of the positioners to maintain their position. By careful adjustment the bottom of the grooves of the positioners were aligned with the bottom of the groove machined into the steel piece. This means the fibre is under no downward or upward tension decreasing the likelihood of a fibre breakage. A side on over view of the set-up can be seen in Figure 5.1 with a close up view shown in Figure 5.2. The different elements are described in detail below and shown diagrammatically in Figure 5.3.

In this set-up the silver solder rod pieces (from [129] and meeting BS EN 1044-1999 [130]) were approximately 5mm in length with a diameter of 1.5mm. The high temperature flux is also supplied by the same company as the solder and comes as a powder.The flux is made into a paste by mixing with a small amount of water and adding one drop of normal washing up liquid. This is then applied to the surface of the steel piece where the solder piece is and 20mm either side. By applying sufficient flux it is not necessary to stream an inert gas during the heating process as the flux will prevent oxidation.

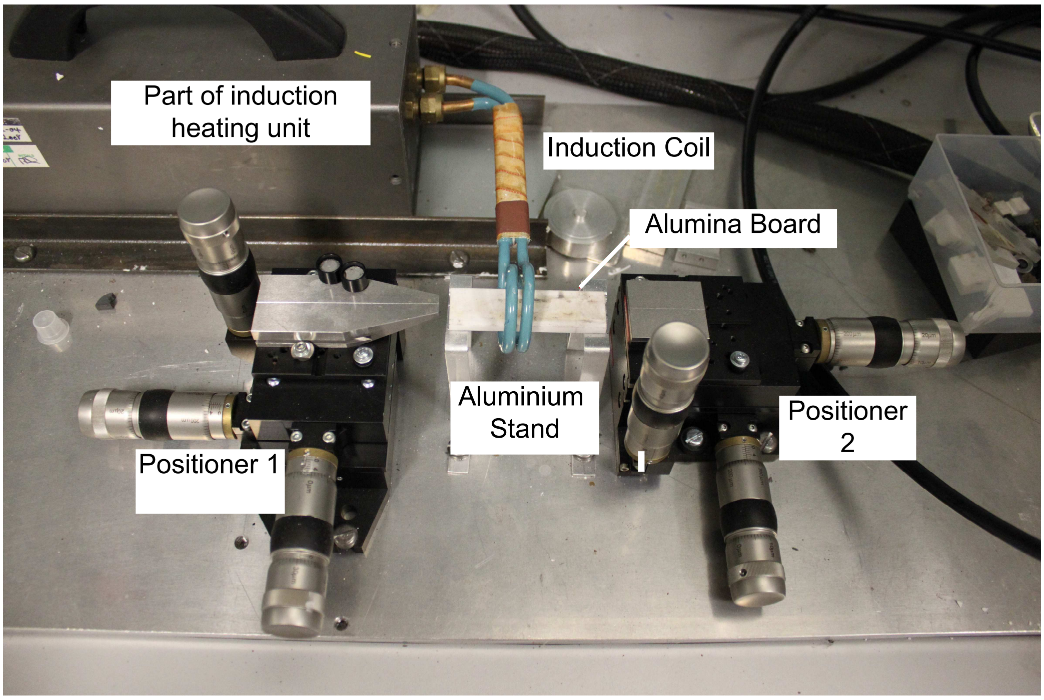

Figure 5.1: The overall set-up for embedding the fibre sensor using an induction heater. On the left and right are the 3-dimensional μm positioners, in the middle is a raised area with a slab of aluminium oxide to hold the steel slab. On top of the positioners are magnets to hold the fibre sensor in position during the heating process; the blue object is the heating coil and is connected to the RF power unit (not shown)

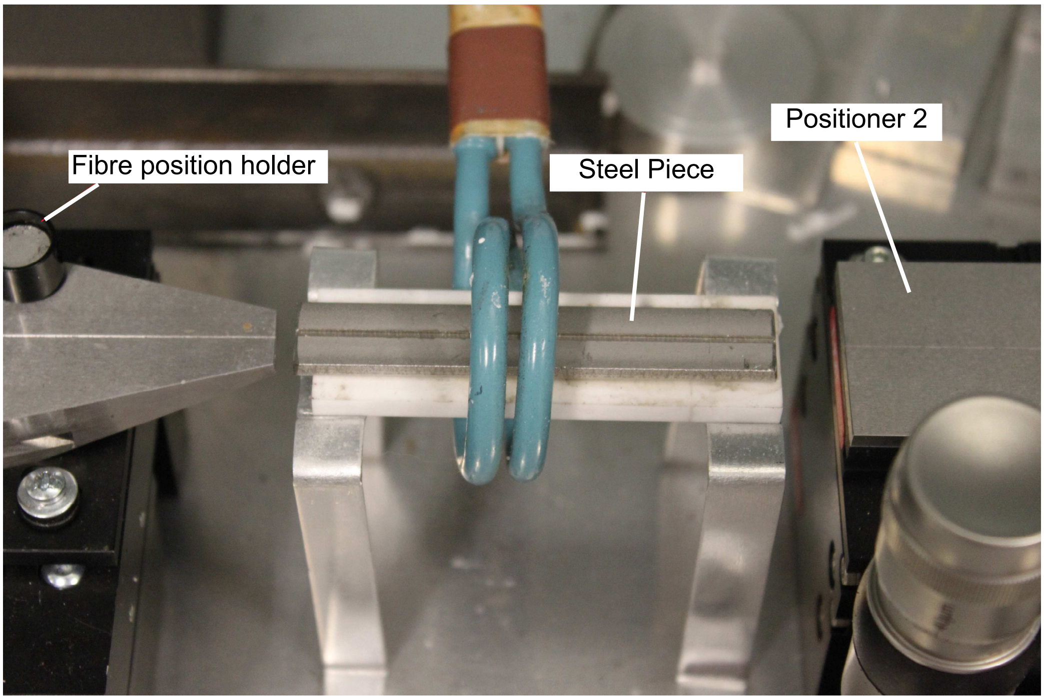

Figure 5.2: A close up of the small induction coil used to heat the silver solder up to its meltus temperature in the 600-660°C range.

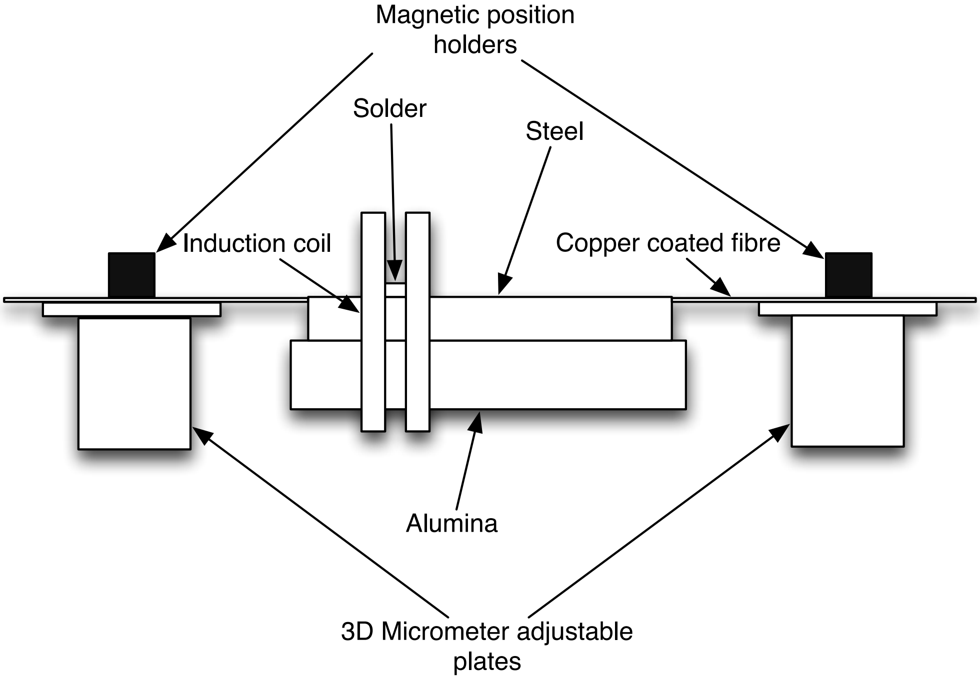

Figure 5.3: A diagrammatic representation of the elements shown in Figures 5.1 and 5.2

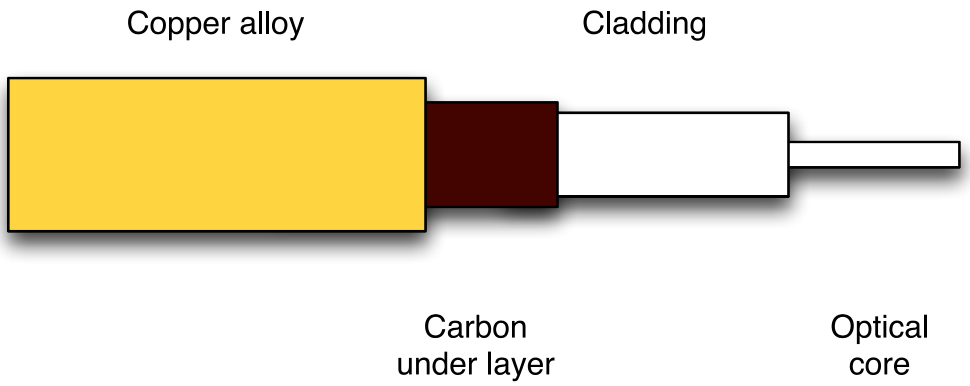

Figure 5.4: Diagrammatic figure of the different layers of the Cu-ball coated fibre

The optical fibre is that supplied by Oxford Electronics, it has a copper alloy coating with an under layer of carbon, this is shown diagrammatically in Figure 5.4. For splicing purposes the copper alloy is stripped off by dipping in 60% nitric acid for approximately 5 minutes. The carbon under layer is removed by the cleaning process of the splicing cycle in the arc fusion fibre splicer. When splicing with a standard single mode 50/125 fibre pigtail the standard single mode (SM) splicing process is used. Each splice was reinforced using a splice protector applied by the standard heating process available on the fusion splicer unit.

The steel piece measured 12mmx50mmx3mm and is made of stainless steel SS617. The machined groove was 1mmx50mmx1.5mm.

The alumina piece is there to insulate the aluminium stands (melting temperature 600°C) from the heated steel piece. Care must be taken with the alumina as is if there is too great a heat difference across the piece it will crack and possibly fall apart.

5.3.2 Trial embedding experiments

A number of trial embeddings were performed to find a good set of heating sequence characteristics. Only short lengths of the Cu-ball fibre were used to begin with.

Steel piece #1

The first trial had an induction current of 200A for 40 seconds. However the solder did not quite melt fully and only once all of the flux had boiled off. It is necessary for good adhesion of the solder to the melt for some flux to still be there when the solder is in its meltus state. For the second piece of solder heating the current was increased to 230A still for 40 seconds. Here however the solder did not quite get into the flow state after 40s and a further 15 seconds of heating was applied to allow the solder to flow in the groove and surround the optical fibre. Thus a total of 55 seconds of heating at 230A was required to heat the solder above its melting point and allow it to flow into the groove whilst still retaining some of the flux. A third trial with the same steel piece (once cooled down) was performed with the current set to 230A for 55s. This was a successful embedding with only one run of the induction heater. After this set of tests the metal fibre now embedded in the silver solder/ steel composition was connectorised using the procedure described above in Section 5.3.1. A broadband light source with a reference peak at 1561nm was then connected to one end with the other connected to a optical spectrum analyser. The resulting spectrum was recorded. This spectrum was then recorded approximately 72 hours later to observe if there had been any changes.

Steel piece #2

In this set of trials the same set-up was used as described above, however instead of allowing the metal/ fibre/ solder to cool back to room temperature a second short piece of solder was applied quickly after the first one had melted (at 55 seconds with 230A), the induction coil repositioned over the new piece of solder and heat applied for approximately 30s. This reduction in time is possible as at the second heating it is not necessary to re-heat the entire piece of steel from room temperature to 600°C. The steel will have retained enough heat and remained close to 600°C within the small time frame between the heating being switched off and then put back on. A third piece of solder was similarly melted and attached as the second.

Again the fibre was connectorised with SM pigtails and attached to the same source as above and the transmission spectrum recorded.

Steel piece #3

This was created similarly as to piece #2.

5.3.3 Results of short piece embedding

Here are given the transmission spectra for each of the trials. For steel pieces #1 and #2 only the transmission spectrums immediately after embedding and 72 hours later are given in Figures 5.5 and 5.6. For steel piece #3 the spectra before, during and after embedding are given Figure 5.7.

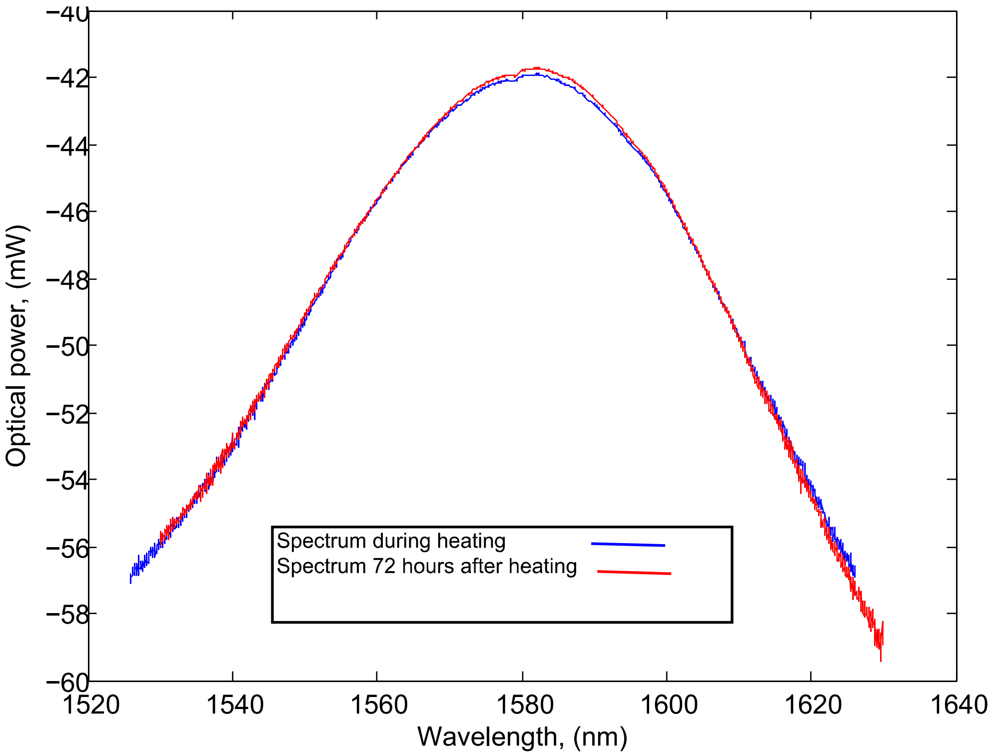

Figure 5.5: The transmission spectra for the fibre embedded in piece 1. The spectrum immediately after the embedding and 72 hours later are shown

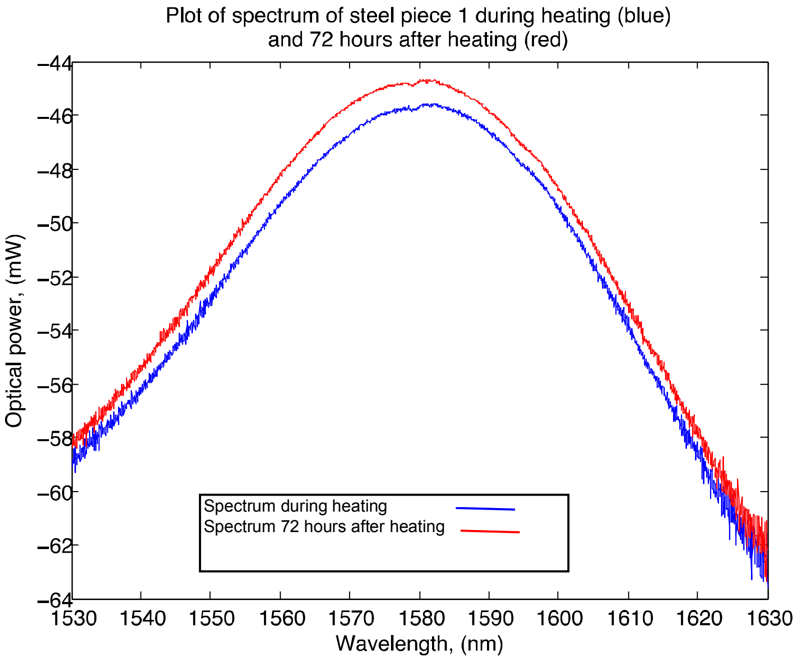

Figure 5.6: The transmission spectra for the fibre embedded in piece 2. The spectrum immediately after the embedding and 72 hours later are shown

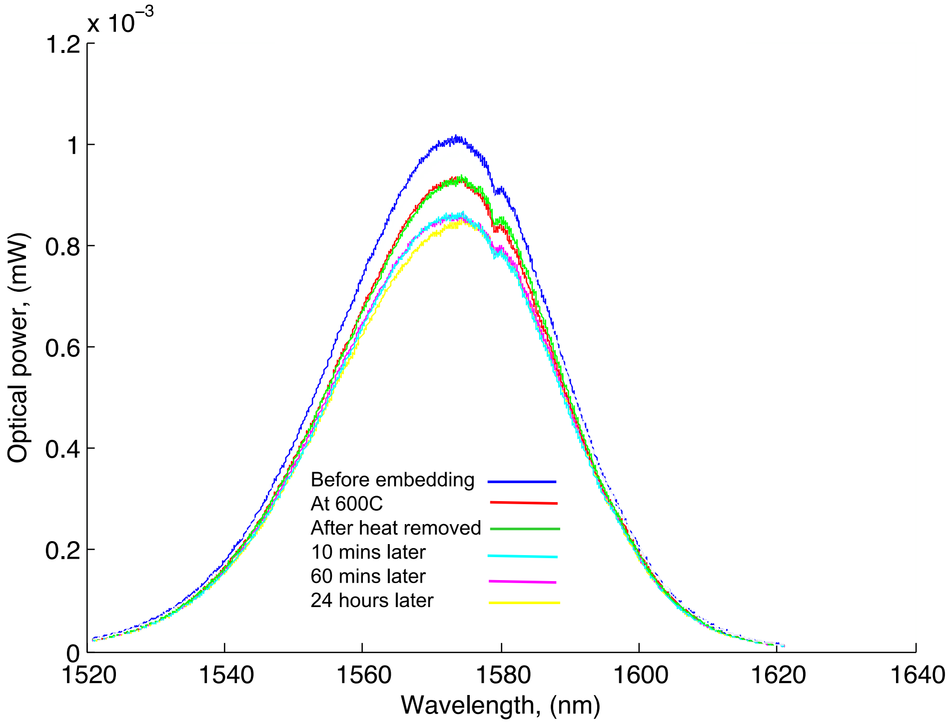

Figure 5.7: Transmission spectra of Cu-ball coated fibre, in steel piece 3, as it is heated and cooled during the embedding process. The peak power increases as the solder cools around the solder, reaching a maximum once it is back to room temperature (dark blue is the spectrum once the metal and fibre have completely cooled, yellow is the pre-embedding spectrum and the other lines are intermediate measurements made in the cooling stage

In Figure 5.7 the transmission spectra of Cu-ball coated optical fibre as it goes through the embedding process can be seen. It can be seen that as the fibre goes from the free un-embedded state through 600°C to a solidified embedded state at room temperature (7 minutes later) the optical power transfer through the fibre actually increases.

It can also be seen that there is a slight increase in the peak wavelength transmission. The increase in optical transmission through the fibre is possibly due to the dissolving of the copper coating into the surrounding silver solder thus changing the optical absorption of the outer layer.

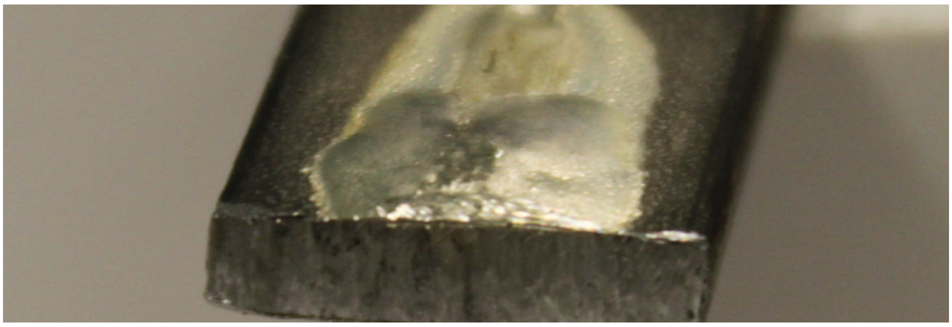

Figure 5.8: The image of the metal/solder/fibre interface. It can be observed that the solder has completely surrounded the fibre with no voids at this point.

Figure 5.9 shows the limited flow when two pieces of solder are melted. The first piece was applied at room temperature and the metal heated beyond the meltus temperature; the second piece was applied when the metal has only cooled to approximately 400°C and then reheated beyond the meltus temperature.

In the manufacture of the piece shown in Figure 5.10 three pieces of solder were melted over the fibre. It can be observed that there is some solder flow in the channel of the metal piece; this is due to good placement of high temperature flux.

In Figure 5.11 a picture of a piece of steel is shown, for this test three pieces of solder have been applied, however due to flux flowing out of the channel, the solder has flowed to the side of the channel and not along it. In Figure 5.12 is a cut-through image of the middle piece of solder of Figure 5.11 this shows the fibre

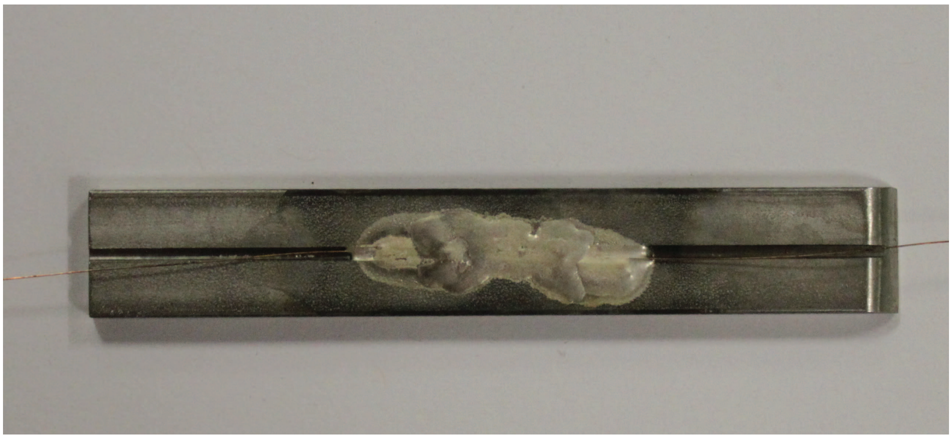

Figure 5.9: This shows the limited flow when two pieces of solder are melted. The one from room temperature and the second when the metal has only cooled to approximately 400°C

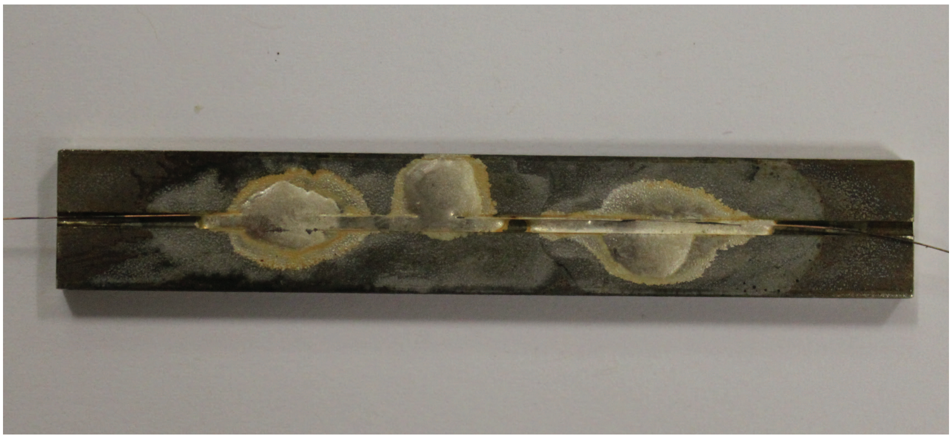

Figure 5.10: In this picture three pieces of solder were melted over the fibre. It can be observed that there is some flow in the channel of the solder. This is due to good placement of high temperature flux.

Figure 5.11: In this three pieces of solder have been applied, however due to flux flowing out of the channel, the solder has flowed to the side of the channel and not along it.

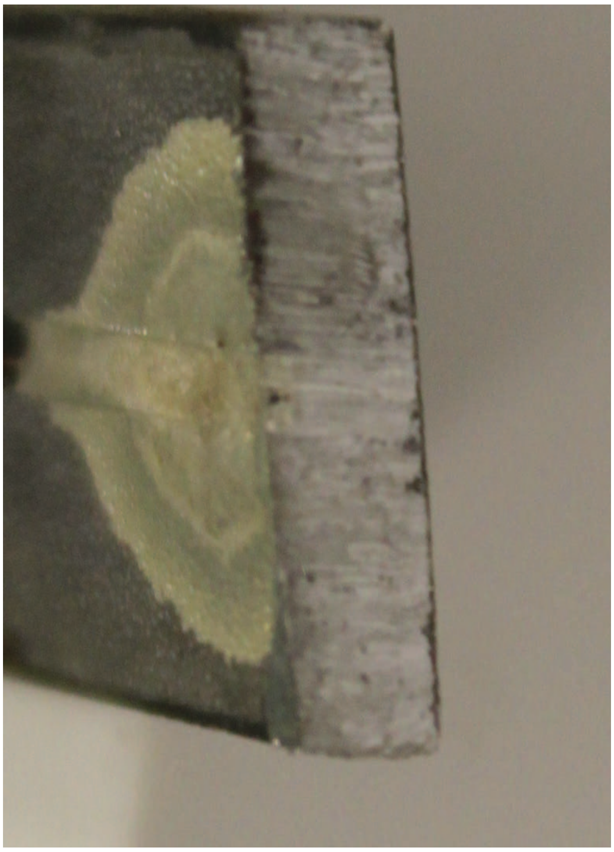

Figure 5.12: Cut-through image of the middle piece of solder of Figure 5.11 this shows the fibre in the very middle of the channel has floated up from the bottom of the channel, it is however fully encased in the solder

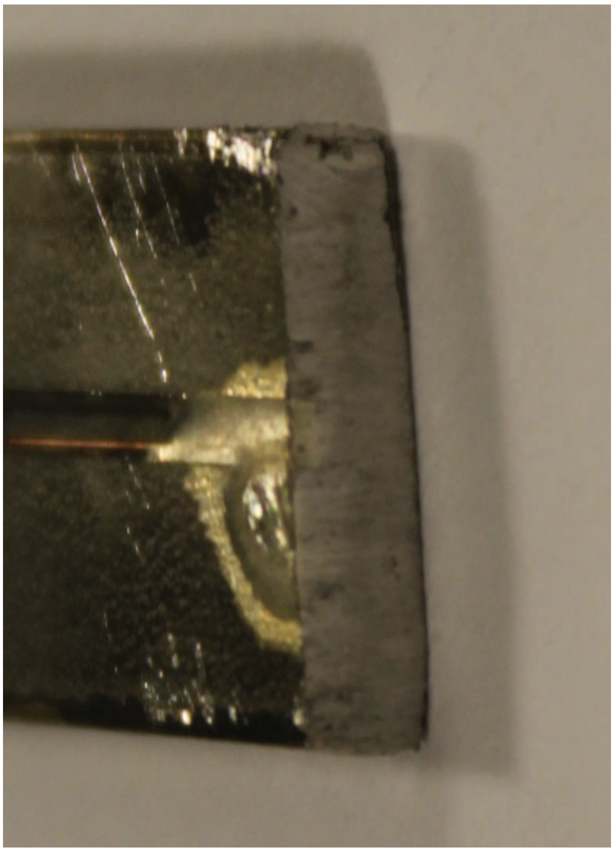

Figure 5.13: This is a face on cut-through image of the bottom piece of solder of Figure 5.11. The solder has some flow in the channel, but mostly over the side. The fibre is encased in the solder and has floated within the liquid solder.

in the very middle of the channel has floated up from the bottom of the channel, it is however fully encased in the solder in Figure 5.13 is shown a face on cut-through image of the bottom piece of solder of Figure 5.11. The solder has some flow in the channel, but mostly over the side. The fibre is encased in the solder and has floated within the liquid solder.

Recommendations for the embedding of fibre sensor with silver solder on steel slab

The following are recommendations from the work performed in embedding the fibre:

- The steel should be well cleaned
- The fibre should be positioned with some tension provided. It should be possible for the fibre to move slightly with the increase in temperature
- The high temperature flux should be paste like and applied only where it is desired for there to be solder
- The induction heater should be moved to heat up the channel to force flow of the solder along the channel

5.3.4 Suggested further development

From the results of the above experiments it has been shown that it is possible to embed the fibre within the silver solder if a small step process is used. To achieve good repeatable results using such a method it is suggested here that an automatic process is developed to move the induction coil along the length of the metal piece. This would deliver a consistent heating of the metal/fibre/solder combination. By doing this the metal piece could be kept at temperature and not be cycled through a series of heating/cooling peaks/troughs.

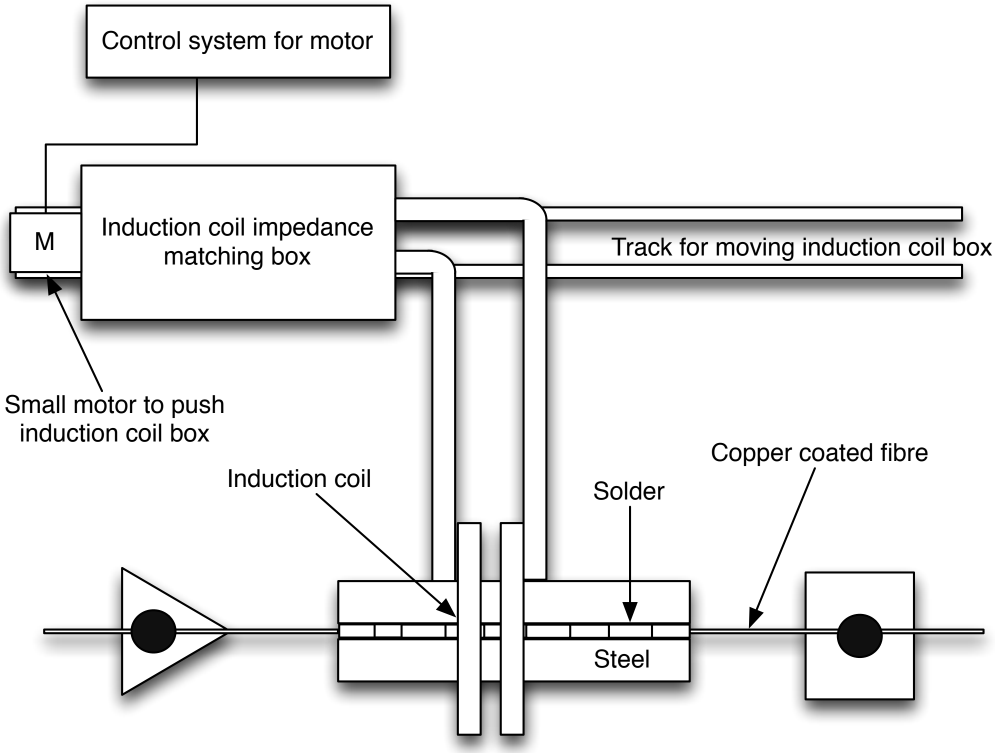

Figure 5.14: Possible set-up for future automated embedding of the fibre along the length of a steel piece using silver solder

It is proposed that the fibre would be laid in the trench and held just as in the manual experiments of the above section, the entire fibre and metal piece would be covered in layer of high temperature flux and the solder would be laid on top along the length of the trench/fibre in small 5mm pieces separated by an amount determined by experiment. This set up is shown in Figure 5.14.

To enable this manufacturing process to be completed the timing of the heater, the timing of the steps, the initial time at the first piece, the current level of the heater, the distance between the pieces of solder, and the trench dimensions would all need to be optimised.

5.4 Summary

In this chapter the construction of a metal sensor package manufacturing process has been described. The following has been discussed in this chapter.

- The fibre Bragg grating should be metal coated to protect the FBG both from physical shocks and from degrading quickly due to diffusion.
  - A number of methods for metal coating were described. The method whereby the fibre is coated whilst being drawn during manufacture is the one which leads to the most strength being retained
  - Metallised fibre made in the above method is available with a copper coating. This exhibits reasonable transmission properties and is compatible with the silver solder used in the embedding.
  - To put the FBG in the metal coated fibre, the fibre must be stripped bare, the FBG written and then recoated using silver deposition with a copper over layer.
- The metallised FBG should be embedded in a metal piece to allow welding to the device being monitored

- A number of methods of attaching an FBG to a piece of metal and then covering the FBG were described
- Vapour deposition of steel on top of fibre sitting on a piece of steel
- Vacuum brazing of the solder/ fibre/ steel combination
- Furnace heating of the solder/ fibre/ steel combination
- Heating inside a retort filled with a Noble gas
- Induction heating of the solder/ fibre/ steel combination

Chapter 6

System Calibration and Testing

This chapter will describe the methods for calibrating the dual wavelength sensor, the challenges and the errors associated with it.

6.1 Introduction

For different gratings, even of the same wavelength, there is likely to be some variation in the strain and temperature sensitivities - both of which must be accurately known in order to produce accurate results for simultaneous strain and temperature measurement. There are two methods of finding these sensitivities, the first by calculation using material properties and the second through experimental testing of an embedded fibre. The first is the problematic option since many of the variables are not commonly or easily known, for instance the precise value of the thermo-optic coefficient. If we assume these values cannot be readily found that only leaves finding the sensitivities experimentally. In principle, only three points per fibre are required to calibrate the system:

(i) The Bragg wavelengths at initial conditions (zero strain point, room temperature)

(ii) Both wavelength shifts at a known strain

(iii) Both wavelength shifts at a known temperature

For best practice, many more readings would be taken to ensure random errors are minimised [131].

- Linearity or otherwise of the results
- Reduce experimental error by use of best fit lines
- Take readings when system is under both strain and temperature changes, allowing validation of the matrix formulae's ability to separate the two terms.

Taking readings for a known temperature is reasonably straightforward; the test piece can be placed in an oven heated to the correct temperature, which can be accurately measured with a thermocouple or other device of known accuracy. The measurement of a test strain is more complicated. It is inconvenient and wasteful to attach an electric strain gauge adjacent to the optical sensor as this cannot be removed and reused, and will likely be destroyed by the conditions within the oven.

To overcome the difficulties and expense of using an electrical strain gauge a method for strain calibration based on models and calculation is proposed.

6.2 Temperature Calibration

To calibrate the temperature response of the sensor system, the simplest way is to place the sensor within an oven and cycle the oven over a range of temperatures. Of course the system must be allowed to reach thermal equilibrium with the oven temperature before the reading is used. The time for this equilibrium to occur can be calculated using finite element (FEM) analysis.

The metal work piece can be approximated by a steel cuboid of dimensions $80 \times 12 \times 6\,\mathrm{mm}$ of density, ρ, $7850\,\mathrm{kg\,m^{-3}}$ and heat capacity, C_p, $475\,\mathrm{J\,kg^{-1}\,K^{-1}}$. Thus the energy required to heat this piece to 150°C is,

$$E_H = \Delta T C_p \rho_d lwh\ , \tag{6.1}$$

$$E_H = 150 \times 475 \times 7850 \times 0.08 \times 0.012 \times 0.006\,J = 3220\,J\ .$$

To calculate the time taken to reach a particular temperature it is possible to use finite element analysis; however it is possible to give an initial first order estimate of the time to come to thermal equilibrium using Newton's heating law [132]

$$T(t) = T_s - (T_s - T_0)e^{-\alpha_N t} \tag{6.2}$$

where α is a constant related to the physical set-up, it is 0.024 for this simulation, T_s is the surrounding temperature, and $T(t)$ is the temperature at time t.

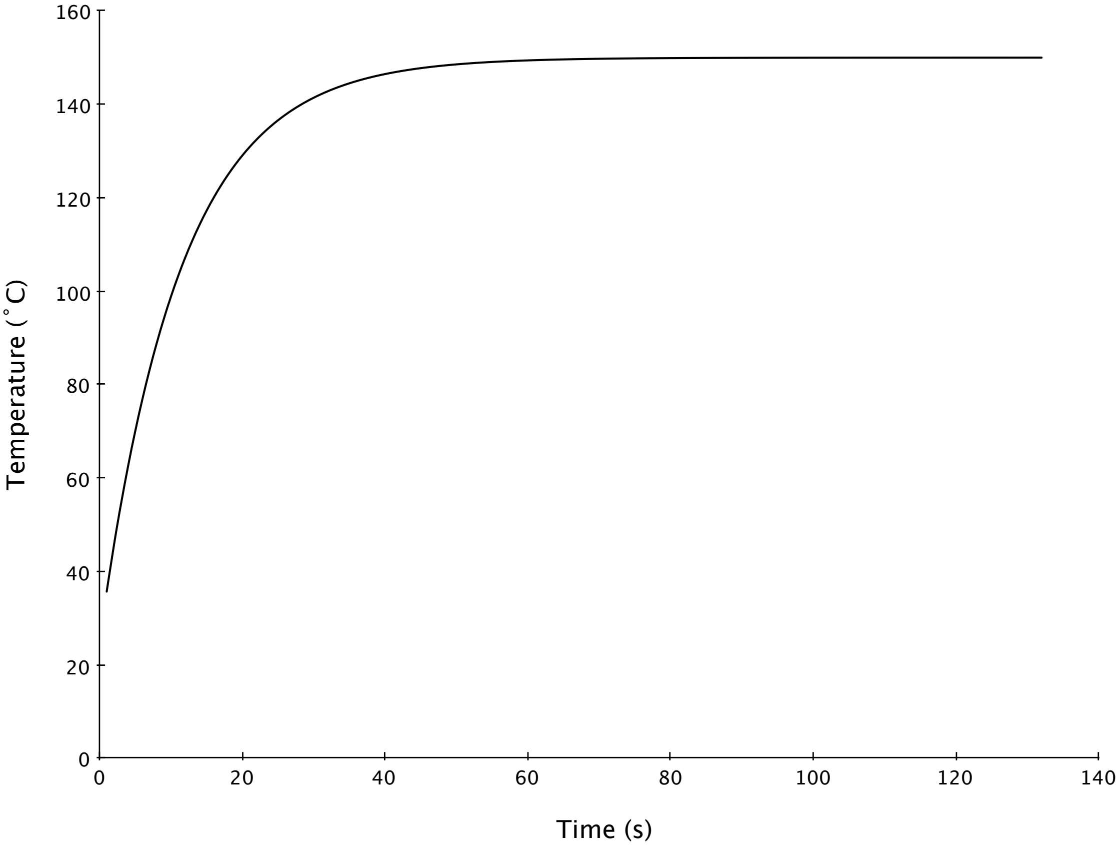

Figure 6.1: Heating of steel piece in an oven at 150°C

From the plot shown in Figure 6.1 it can be observed that the steel reaches equilibrium after 50s. However when doing the testing steps of 10°C from room temperature to 200°C are used. At each step the sensor is left for some time to reach temperature equilibrium with the oven before a measurement of the wavelength is made.

6.2.1 Temperature sensitivity of the metallised FBG before embedding

Before the metallised FBG is embedded on the steel piece with silver solder is necessary to characterise its temperature sensitivity. This was done with the procedure outlined above; however due to the FBG's small thermal mass, the time to reach equilibrium is very short.

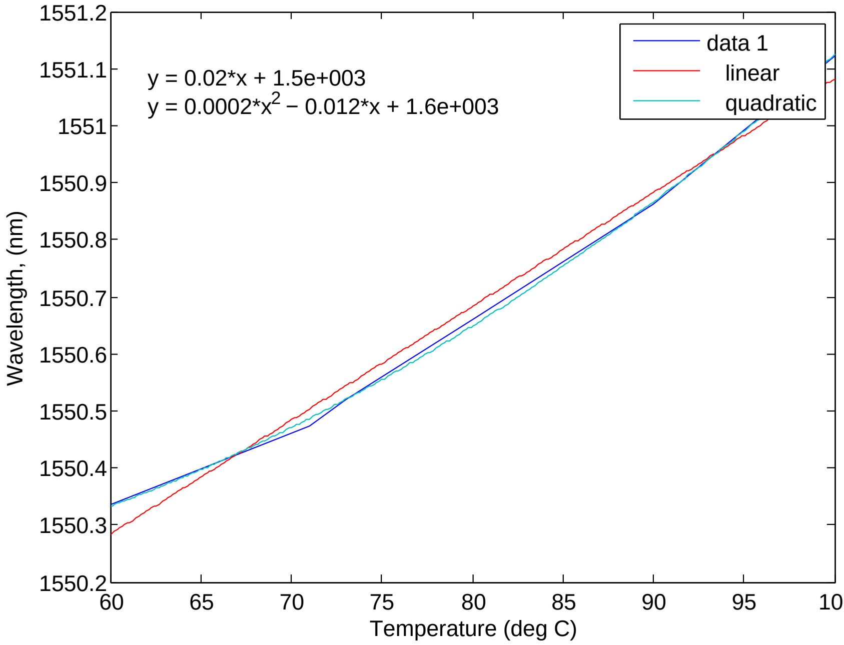

Figure 6.2: Wavelength of metallised FBG (not embedded) with temperature from 60°C to 100°C showing linear and quadratic fitting equations.

The results of heating the un-embedded metallised FBG are shown in Figure 6.2, the FBG was heated up over a period of 35 minutes with readings taken of the temperature and matched to the time elapsed. This FBG exhibits a temperature dependence of 0.02nm per °C if the sensor is considered linear.

6.3 Strain Calibration

There are two main methods of inducing tensioning strain in a beam; 1) by using a pair of clamps each attached to a common screw and then extend the distance between the clamps using the screw to apply a linear strain along the beam [133]; or 2) by supporting the beam at one end and applying mass to the far end thus forming a cantilever beam. With the equipment and knowledge available to the author the latter option was chosen.

To perform a strain calibration the beam will be held in a cantilever geometry as shown in Figure 6.3.

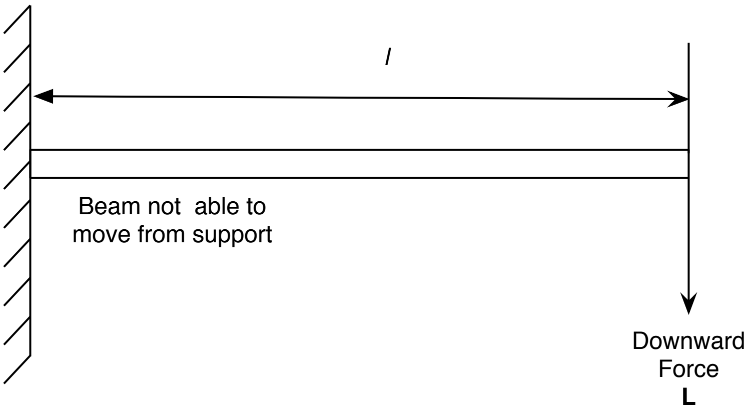

Figure 6.3: Cantilever of length l with a load L at its far end.

A small hole was drilled in the beam at the position shown in Figure 6.4 below. A hole is used to tie the length of uninsulated metal wire to the beam as the beam will be tested at a temperature in excess of 200°C where normal tin-lead solder would melt. At the end of the metal wire a series of metal blocks were placed, each having mass of approximately 50g (accurately measured using balances accurate to ±0.001g. The set of six metal blocks were designed and built in-house and are of the shape shown in Figure 6.5.

The beam in this set-up is the piece of metal into which the FBG sensor has been embedded. The embedded sensor experiences a different strain magnitude to that on the surface of the metal length as the beam is under a tangential force rather

Table 6.1: Masses of blocks used for strain calibration.

block No.	mass (g)
1	49.998
2	50.001
3	50.002
4	50.000
5	49.997
6	49.999

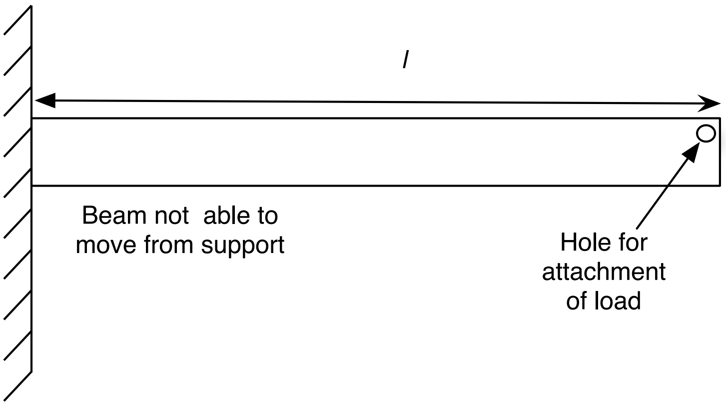

Figure 6.4: Cantilever of length l with position of hole for attachment of load shown.

than a longitudinal force. To enable the calculation of the force on the sensor under force a model must be created of the experiment.

6.3.1 Modelling the Strain at the Sensor

There are a number of ways to model the strain at the embedded sensor's position. These range from basic analytic techniques to finite element analysis. Analytic techniques are useful for giving the first order calculation of the strain, however for more accuracy a finite element method is preferred.

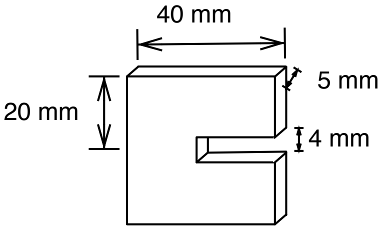

Figure 6.5: Drawing of one of the metal blocks used to apply force at the end of the cantilever beam detailed schematics are shown in the appendix; material, mild steel

Analytic Technique for Strain Calculation

This technique finds the strain from the cantilever's geometry. This method can be used when prototyping the sensor package in the laboratory, however it is unsuitable for calibrating once the sensor is attached to a structure.

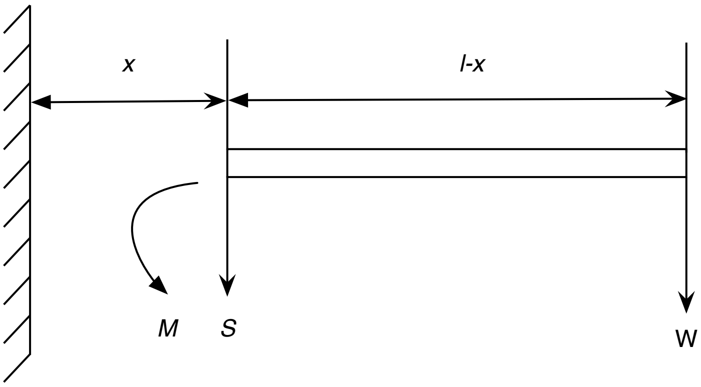

Figure 6.6: Drawing of selection of cross section of beam distance x from supporting wall

Imagine the cantilever described above of length l with a weight W attached at its far end (as shown in Figure 6.6. Assume that the deflections of the beam are negligible in comparison to the leading dimensions. Take a cross section at a distance x from the supporting wall.

Therefore shear force is given by

$$S = -W \; , \tag{6.3}$$

and the moment, M, is given by,

$$M = (L - x)W \; . \tag{6.4}$$

For beam analysis,

$$\frac{\sigma}{y} = \frac{M}{I} \,, \tag{6.5}$$

where σ is the stress given by $E\epsilon$, y is the distance from the central axis and I is the second moment of area[1] and E is Young's Modulus.

Combining the formulae for I, and σ it is possible to get a formula for the strain in terms of known or measurable quantities,

$$\begin{aligned} \sigma &= \frac{My}{I} \,, && (6.6)\\ \Rightarrow \epsilon &= \frac{My}{EI} \,, && (6.7)\\ \Rightarrow \epsilon &= \frac{(L-x)W\frac{d}{2}}{E\frac{bd^3}{12}} \,, && (6.8)\\ \Rightarrow \epsilon &= \frac{(L-x)mg}{Ebd^2} \,. && (6.9) \end{aligned}$$

The accuracy with which strain can be calculated in this manner depends on the accuracy with which the component variables can be determined. These are discussed below.

Measurement Inaccuracies

For each variable in Equation 6.9 the best possible error using standard available equipment is given.

- L and x would be measured by ruler, giving an accuracy of ±0.5 mm.
- b and d would be best measured by a Vernier micrometer[2] giving an accuracy of ±0.0005 mm/
- m would be measured by a balance giving an accuracy of ±0.001 kg, or ±0.0001 kg on the best equipment.

---

[1] See Appendix for full definition of I

[2] The use of a Vernier micrometer rather than a standard micrometer is crucial since it permits measurements to 0.001 mm rather than 0.01 mm; this degree of accuracy is necessary to give satisfactory results

- The accuracy of E will be discussed in detail below.

A fair example for the system under consideration is shown in Table 6.2.

Table 6.2: A set of typical values for strain calculation

Variable	Value
L	235 mm
x	120 mm
b	10 mm
d	3 mm
E	200 GPa

Then if the applied mass is 1 kg, then the strain applied to the sensor's centre is $376\mu\epsilon$.

Table 6.3: A set of worst error case values

Variable	Value
L	234.5 mm
x	120.5 mm
b	10.0005 mm
d	3.0005 mm
m	0.999kg
E	200 GPa

When the maximum error conditions are considered then the strain applied to the sensor's centre is $372\mu\epsilon$ a difference of -$4\mu\epsilon$ compared to the original value. Thus the error given a constant E is -$4\mu\epsilon$.

Thermal Inaccuracies

With stainless steel being used as the metal substrate there is an expansion of the steel as the temperature of the oven increases, this will lead to an overall increase in the length of the steel piece. At a room temperature of 20°C the thermal expansion coefficient of steel is, $\alpha = 17 \times 10^{-6} K^{-1}$, if the oven temperature is increased to 420°C then there is an overall temperature increase of 400°C. The increase in length is then,

$$\Delta L = L_0 \alpha \Delta T \ , \tag{6.10}$$

where L_0 is the measured length of the dimension at 20°C.

Thus the expected new dimensions of the piece at 420°C will be

Table 6.4: Dimensions of the steel piece at 420°C

Variable	Value
L	237 mm
b	10.1 mm
d	3.02 mm

Finite Element Analysis for Strain Calculation

To enable to the calibration of the system's response to strain it is necessary to calculate the strain developed in the beam due to the masses being added to the end of the beam. In modelling this set-up it is assumed that the strain applied to Bragg gratings is equivalent to that on the surface of the metal beam. This is because the glue used has good adhesion between the beam and fibre; therefore coupling the FBGs fully to the beam.

The most accurate method available is to create a 3D finite element model of the set-up this model is shown in Figure 6.7.

The strain profile for each of the weights can be seen in Figures 6.8, 6.9, and 6.10

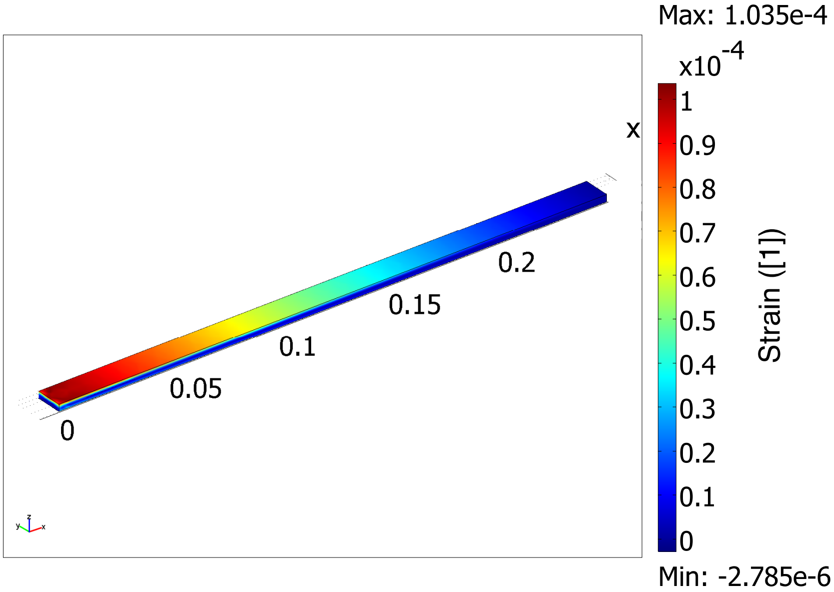

Figure 6.7: Example of the 3d model created and simulation performed to calculate the surface strain of a cantilever beam as used in the experiment

From these calculations it is clear that the strain is highest closest to the fulcrum point (the end of the beam attached to the straining rig.) This system of weights will only allow a maximum of $112\mu\epsilon$ of strain to be applied. However this is enough to prove the concept of using this type of sensor calibration set-up. To increase the strain either larger weights should be used or a longer beam should be attached to the test piece to extend the leverage of the weights already described.

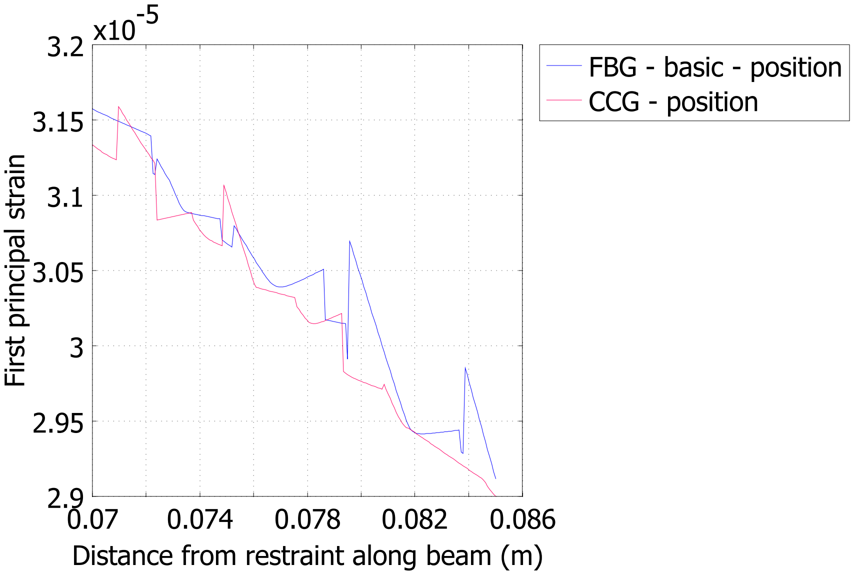

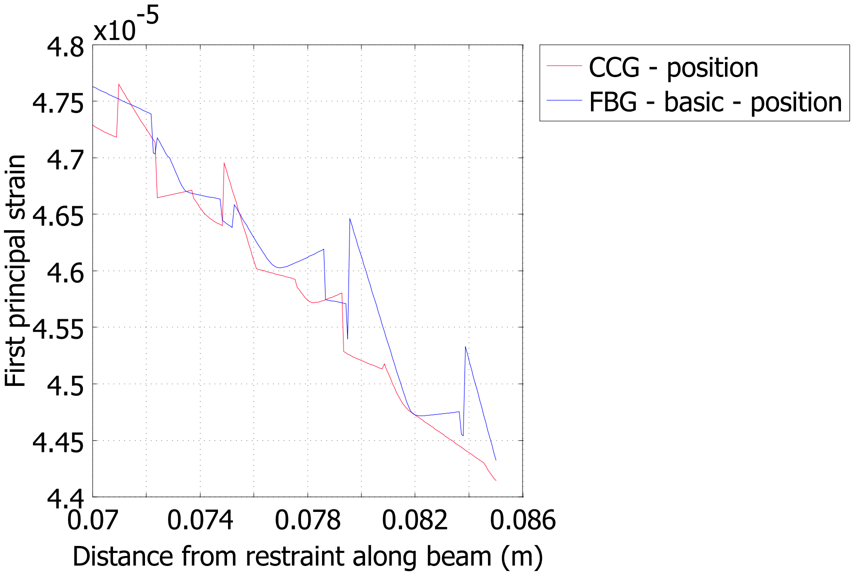

(b)

Figure 6.8: First Principal Strain on the FBGs and CCGs glued on to the cantilever beam with(a) 1 weight attached, (b) 2 weights attached

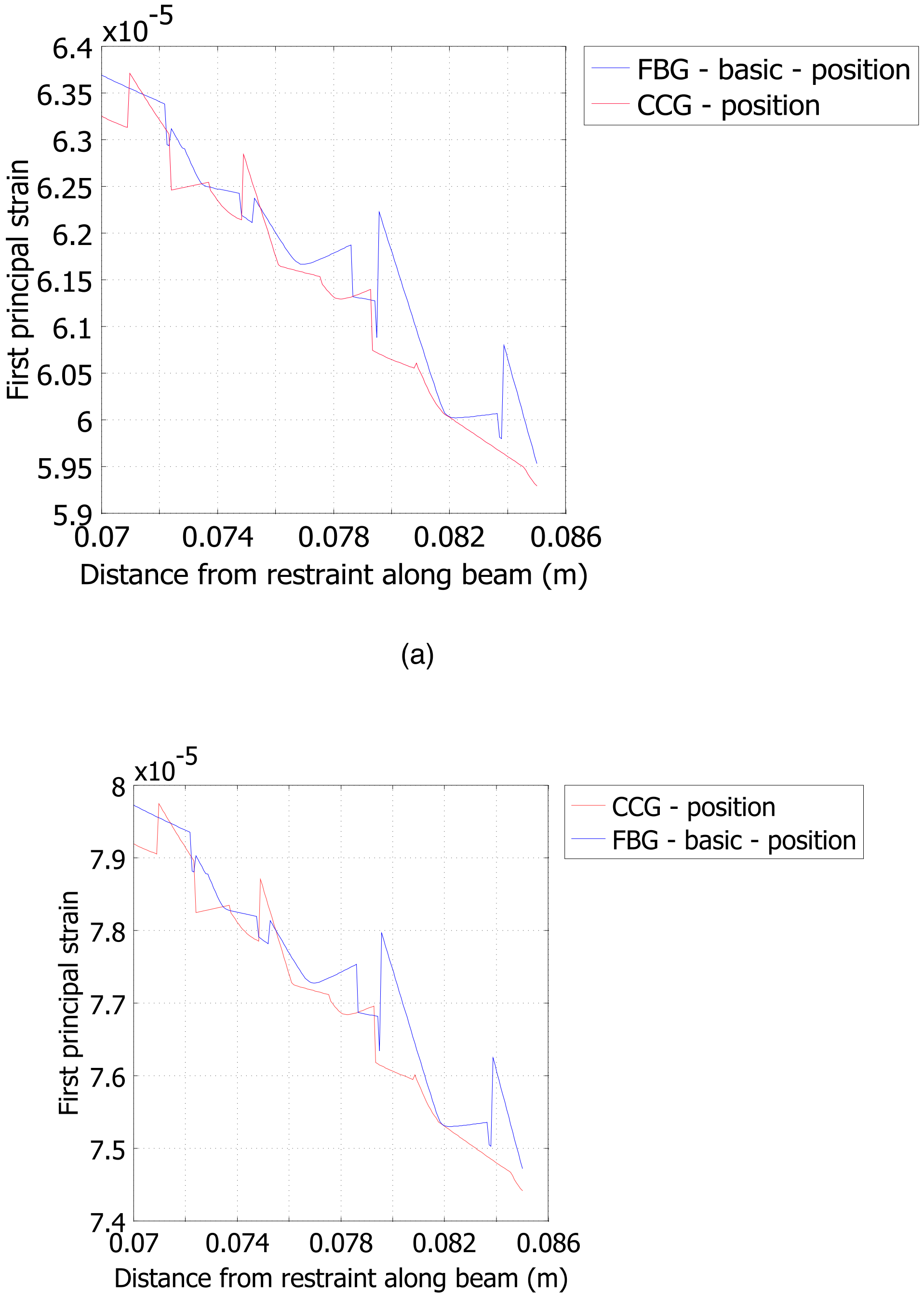

(a)

(b)

Figure 6.9: First Principal Strain on the FBGs and CCGs glued on to the cantilever beam with(a) 3 weights attached, (b) 4 weights attached

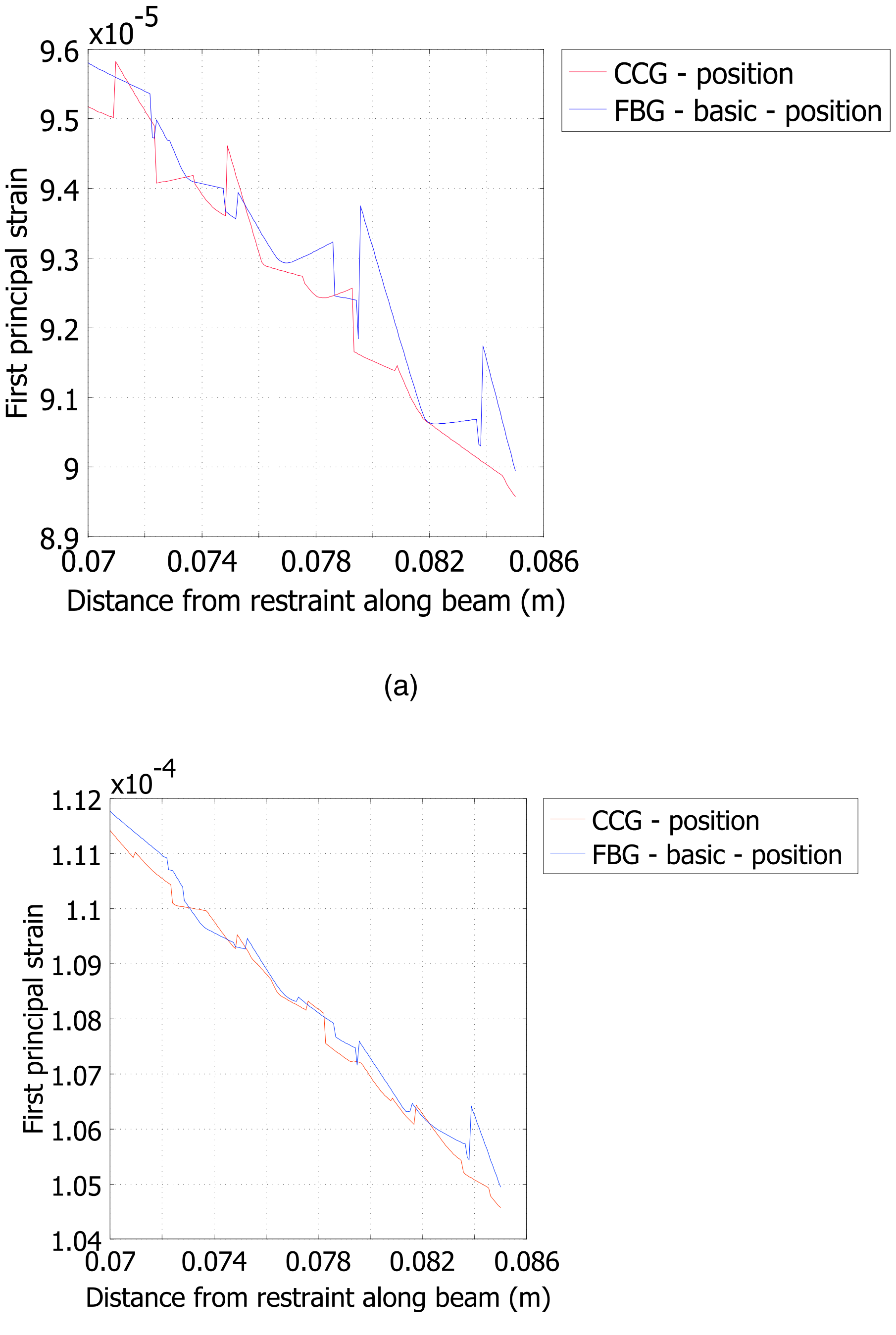

(a)

(b)

Figure 6.10: First Principal Strain on the FBGs and CCGs glued on to the cantilever beam with (a) 5 weights attached, (b) 6 weights attached

6.3.2 System Strain Calibration

The interrogation system was initially calibrated using one of the CCG's glued to the top surface of a cantilever beam. In this section the results of these tests will be presented along with an analysis of these results.

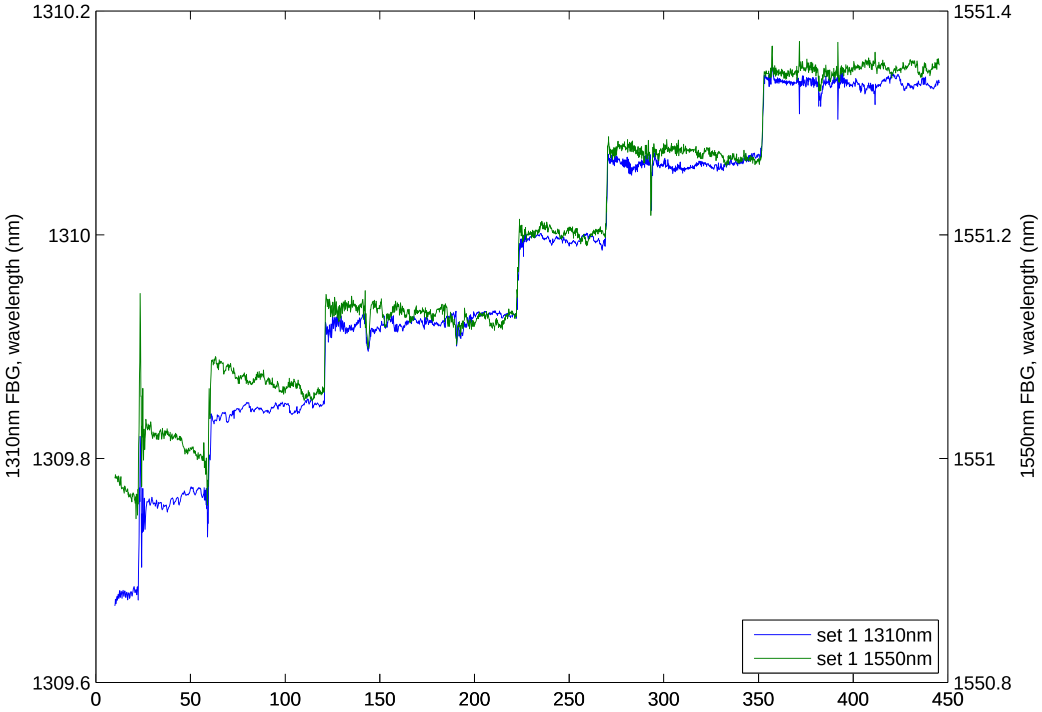

Figure 6.11: The first set of data captured using the system developed in this thesis.

In Figures 6.11, 6.12, 6.13, 6.14 the step changes in strain can easily be seen within the data. However there is a some noise within the system. This was identified as originating from the software system running slowly due to too many calculation processes taking place in the same loop as the data capture process. In Figure 6.15 it can be seen that there is a non-linear relationship between the change in wavelength of the 1310nm and 1550nm grating. This means that there is a difference in the stain-optic coefficient of the gratings.

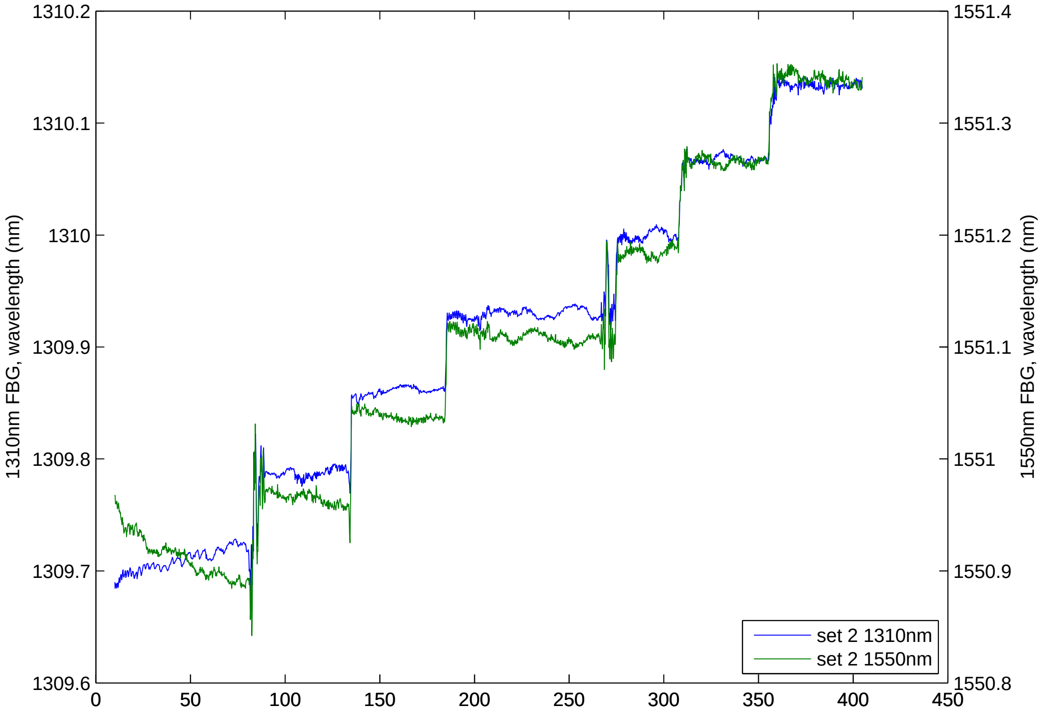

Figure 6.12: The second set of data captured using the system developed in this thesis.

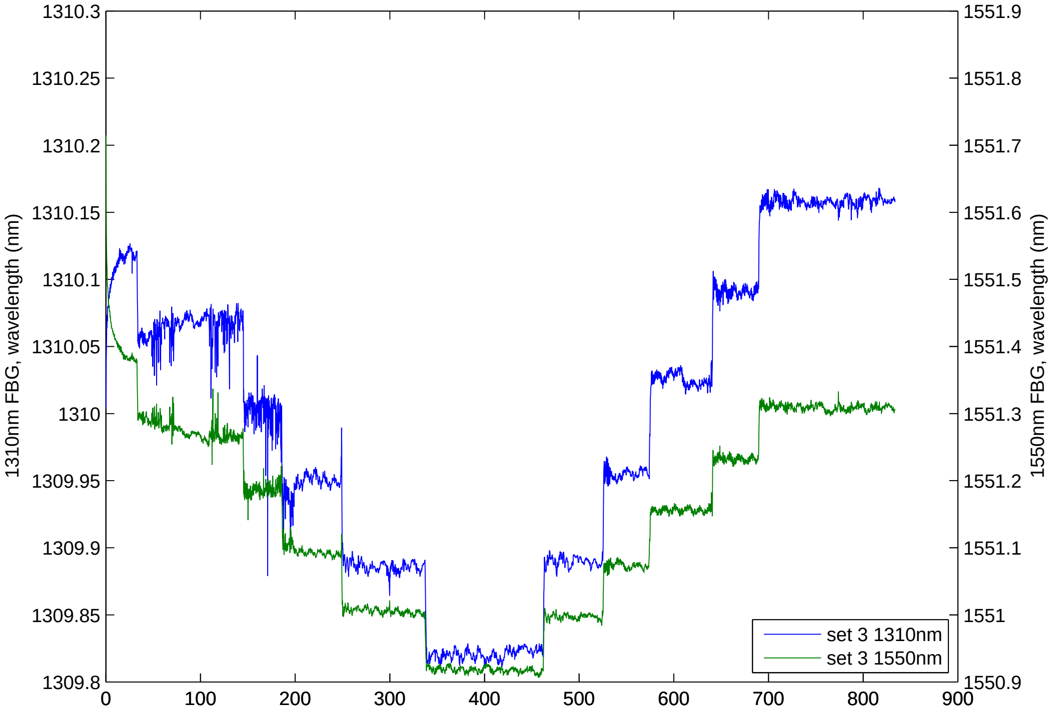

Figure 6.13: The third set of data captured using the system developed in this thesis.

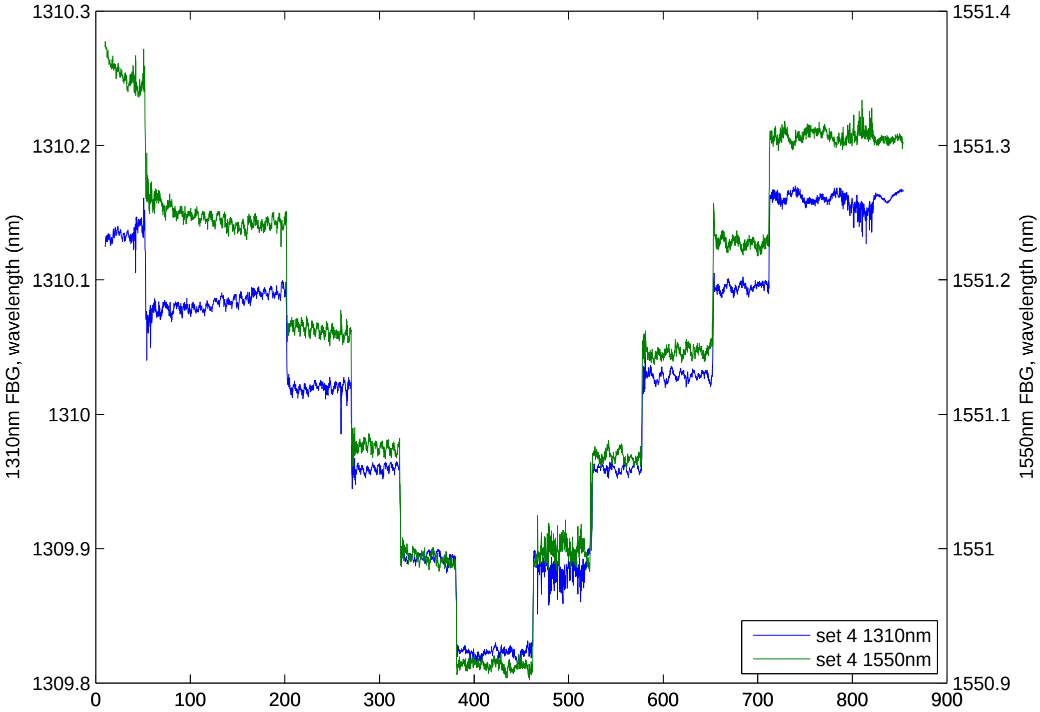

Figure 6.14: The fourth set of data captured using the system developed in this thesis.

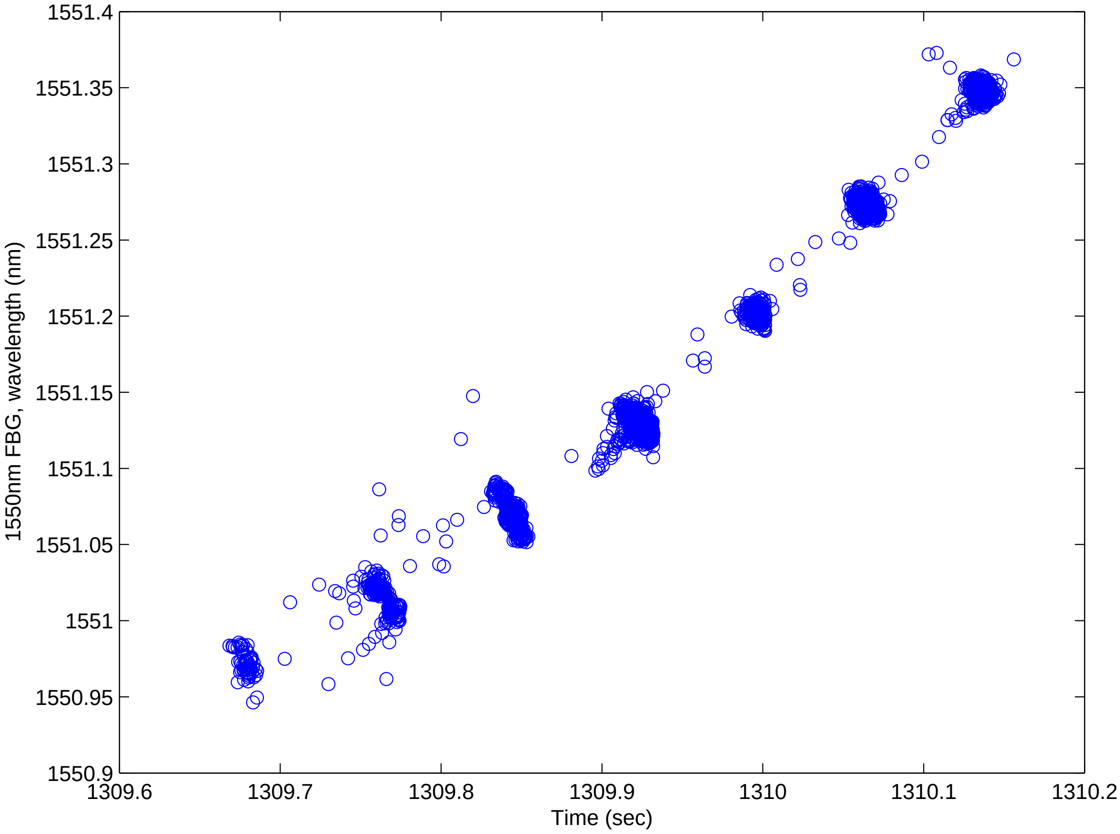

Figure 6.15: Plot of wavelength of 1550nm peak against 1310nm peak

6.4 Summary

In this chapter,a number of procedures are considered for the calibration of the instrumentation system along with some initial results of the calibrations performed.

This chapter identifies the issues surrounding calibration of a dual measurement system, including the dual effect of temperature changes on the wavelength due to the strain induced by the surrounding material and the effect of the surrounding material on the sensitivity of the sensor.

This chapter sets out methods by which the sensor could be calibrated, explaining in detail the benefits and drawbacks of each one. Also presented is an example set of results for a series of strain only calibrations.

Chapter 7

Conclusions and Future Work

7.1 Conclusions

Monitoring of the temperature and structural integrity of a nuclear fusion reactor port plug involves the creation of a measurement system that can survive and operate in the harsh nuclear and thermal environment of a port plug for the duration of the port plug's lifetime. Present thermal electrical sensors are able, to some extent, operate within this environment, however strain gauges are not commonly found for such applications; however they require multiple devices to measure temperature and strain at a single point. Further as more sensors are added the placement of wiring and connections through the radiation shield will increase, thus decreasing the effectiveness of the shield. Electrical sensors are also not individually identifiable by their output. As such a system based on non-electrical systems and with position related outputs are to be desired.

The object of this thesis has been to prove the concept of using passive optical fibre sensors - which have an excellent record of high performance in adverse conditions - to measure temperature and strain within an ITER port plug. It was firstly established that there exists no off the shelf system capable of interrogating broadband fibre Bragg grating reflections (greater than 100nm difference), although there did exist fibre Bragg gratings with two wavelengths in different optical bands.

For the objective of measuring point strain and temperature simultaneously using one sensor a fibre Bragg grating with two wavelengths in different bands was selected, with one grating is written on top of the other. This was because each wavelength exhibits a different strain and temperature sensitivity. This difference can be used to calculate the strain and temperature that the sensor is exposed to. The particular implementation of the grating (chemical composition) was chosen as it has been shown to have high temperature and radiation stability.

As the sensors are very fragile it is necessary to package them in some manner. First the sensor must be coated in a layer of metal (copper in this thesis) and then embedded into a piece of steel. A novel method of induction heating with silver solder was selected to embed the sensor. This method provided good coupling at the fibre/ solder interface that then provides strong transfer of temperature and strain changes into the FBG.

To interrogate the dual wavelength FBGs in different bands many different solutions were possible; however only with one solution is it possible to monitor both wavelengths with one optical filter system. The selected optical filter exhibits high finesse, low attenuation and fast interrogation, this is based on an all fibre construction of the actual filter with a piezoelectric element to select the wavelength. When combined with a real-time data capture and analysis system then a high resolution FBG interrogation system is created.

This interrogation system has been demonstrated as operating at scan frequencies of 30Hz with 2 sensor FBGs and two fixed and temperature stabilised FBGs providing the top and bottom of the range for system calibration.

7.2 Summary of thesis

It was identified that there was a need for the measurement of temperature and strain within the highly radioactive, high-temperature, and high pressure environment of a nuclear fusion reactor port plug. It was desired that the measurement of temperature and strain was performed simultaneously at each point of sensing; this is so that the data can be used within engineering models to check the condition of the port plug during operation and start-up/shutdown.

With this set of criteria a study of the available technologies was undertaken. The main aspects of consideration for this analysis were the sensors' sensitivity, accuracy, repeatability, and hardness to radiation effects. This included examining traditional methods for the detection of temperature and strain variations based on electrical sensors (strain gauge and thermocouple) along with a number of optical sensor technologies/ techniques. The electrical sensors or transducers were shown to be unsuitable for application within a nuclear fusion reactor port plug due to a number of reasons, including radiation induced E.M.F., and long-term and position specific drift due to radiation impact. From this analysis it became clear that an optical technology solution will be best suited to creating a long-term solution for the monitoring of strain and temperature within the specified environmental conditions.

Deeper study of available optical sensor technologies/ techniques was then performed to identify suitable sensors that with further research could meet the required sensing criteria by integration of multiple technologies and/ or adjustments to existing sensors. The studied technologies included fibre Bragg gratings (including specific derivatives), and Fabry-Pérot interferometers. It was then identified that a dual wavelength chemical composition grating (CCG) was the most suitable available sensor to be used as a basis for the construction of a multi-variable sensing element. This was because the grating is sensitive to both strain and temperature sensitivity, has high resistance to high energy neutrons, and is suitable for the high-temperature environment found in a nuclear fusion reactor's port plugs.

However, after significant modelling of the dual-wavelength sensor and performing an error analysis of the same, it was realised that there was a need to increase the strain sensitivity of the device as this was quite small in terms of Bragg peak movement. To increase this sensitivity methods of coupling the grating with materials with larger coefficients of thermal expansion were considered. These methods included epoxy bonding of the sensor to a metal shim (not radiation proof), embedding the sensor in aluminium (not temperature resilient enough) and coating the sensor in a metal before embedding this in a steel piece using a high-temperature solder (most suitable for this application.) The selected method applies copper to a silver substrate to the optical fibre sensor using an electroplating process for copper application and a silver oxidation process to apply the silver to the activated optical fibre surface. This metal coating provides some mechanical protection to the optical fibre whilst embedding the sensor in a stainless steel piece using a high temperature silver solder provides a higher strain response. An induction heating process was chosen to melt the silver solder around the fibre sensor.

It is necessary to provide a method for the measurement of the peak wavelengths reflected from the Bragg gratings. This method must accurately measure the reflected wavelengths from both peaks of the dual wavelength sensor; these wavelengths can be separated by up to 140nm which is a challenging optical range. Most solutions such as the Mach-Zehender interferometer and arrayed waveguides would require multiple detectors, such a set-up would require a more complicated signal processing solution as the detectors would be required to be completely synchronised in time to allow the simultaneous calculation of strain and temperature. Thus a piezoelectric, tuneable waveguide was chosen as it can cover the required optical range, has a high finesse, and can easily be integrated with the fibre optic cabling, and controlled by the electronic systems present. A real-time control system was built around a National Instruments' PXI real-time computer, this included a transimpedance amplifier to change the output of a photodetector from a current to a voltage, a pair of temperature compensated fibre Bragg gratings were used to calibrate the system by providing upper and lower limits of optical bandwidth to be analysed. This system analyses the Bragg peak wavelengths in real-time and calculates the strain and temperature being measured by the sensor package.

The software on the real-time computer was custom built for this application this included a multi-peak analysis algorithm was created specifically for this system based on a double line analysis method (not used anywhere else previously for multi-peak analysis). This double peak method was chosen as it performs better than thresholding peak detection methods as these can be easily upset by noise in the system. Using the double peak method with an accurate calibration procedure it is possible to get very high resolution measurements of the peak wavelength (to the 13th decimal place), however the accuracy is lower for this system due to noise errors introduced by the light detector circuit and the pressure sensitivity of the temperature corrected fibre Bragg gratings used for calibration purposes.

7.3 Research Outcomes

The overall research output of this thesis work has been the development of a dual waveband optical interrogation system, identification of a process for the embedding of optical fibre sensors within a stainless steel surround.

- Identification of a new method for the embedding of optical fibre sensors in stainless steel. This method involving the melting of a silver solder over the optical fibre sensor has not been previously proposed. This method allows exact placement of the fibre sensor within the package using off-the-shelf materials.
- Designed a system for embedding optical fibre sensors in a stainless steel using a silver solder as the coupling material. This use of an induction heater to heat the steel shim which then heats the solder is a unique technique in sensor packaging.
- Models of the induction heating process of the sensor package have been produced, showing that a suitably coated optical fibre can survive the heating and cooling sequence during the embedding process.
- The creation of a customised control programme for the control of a piezo-electric wide-band optical filter. This is the first application of a dual-band

optical fibre filter for a sensing application, especially one for fusion reactors.

- Linearization of the output of the optical filter, this has not been performed before for such a wide band filter. This simplifies the signal processing algorithm by using linear equations to translate the measured power spectrum into a wavelength.
- Development of a real-time signal processing platform allowing for the implementation of innovative software solutions to improve the accuracy and interrogation speed of spectrally encoded sensors. This is the integration of a number of hardware (real-time processor, real-time operating system, optical filter, and optical convertors), with a number of pieces of software (voltage measurement, peak detection, signal shape extractor, peak calculation, and drift offset calculator). This set of devices has not been previously put together before.
- Modelling of the use of a dual-wavelength sensor to make accurate, simultaneous, measurements of strain and temperature. This is the first time that 1310nm and 1550nm gratings have been suggested as a sensor for the measurement of temperature and strain simultaneously. Previous work with FBGs have used only FBGs separated by a few nanometers.

7.4 Future Work

The aims of any future work in this area would be to further develop more accurate methods for the coating of the fibre, being able to accurately control fibre thickness would be a definite benefit to this work.

7.4.1 Metal-glass Interface Theory

There is a need to more fully understand the coupling at the metal-glass interface and between the metal-metal interface(s). This will need to consider what the best surface shape of the glass molecules should be, and what size and shape of metal crystal structure would fit best with them, these can be adjusted by doping of the glass or alloying the metal and heating/ cooling to different temperatures. This will lead to the discovery of new alloys that will fit with the underlying glass structure. A detailed understanding of the glass structure when different doping elements and concentrations are present would give a possibility of the creation of a general theory of glass-metal interfaces in the presence of dopants.

7.4.2 Application of metal layers

The extension of the metal-glass interface work would be to then study methods of applying the different metals to the surface of the glass fibre, examining electroplating, laser ablation, chemical reduction of the metal on the surface, and future novel deposition methods. This is because the different methods of application will cause different types of metal structures to form on the glass surface. It will also be necessary to analyse the glass surface preparation methods, e.g. using hydrofluoric acid to activate the surface of the glass or using a strong alcohol to remove impurities from the surface of the glass. This work will realise stronger and more adhesive coatings that will enable the glass fibre to survive higher temperatures and strains.

7.4.3 Development of a new embedding alloy

Although the work on metal-glass interfaces is critical to the future development of the work presented in this thesis, it is also key that a suitable embedding alloy be found that has all the desired technical qualities for coupling the coated optical fibre to a metal substrate for further installation within the fusion reactor's port plugs. This study would focus on the removal of silver from the alloy, the effects that ionising radiation has on the alloy and the changes that are observed, and a detailed understanding of the temperature effect on the coefficient of thermal expansion. By doing this a viable embedding material could be found that would be very effective in coupling and attaching the fibre to the metal substrate.

7.4.4 Automatic embedding process

The development of an automatic embedding process would increase the precision and repeatability of the embedding of the fibre sensor within the metal substrate, which is difficult in a manual process. It was found in this thesis that manual handling and placing of the fibre, solder, and heater was very difficult.

Also the further development of a rig to hold the fibre/ metal package in position during the embedding process would allow the more accurate positioning of the optical sensor.

7.4.5 Increase the speed of the sensor measurements

The measurement and analysis of the Bragg wavelength has been limited to 30Hz in this work. To increase this speed one requirement is to develop a faster algorithm for analysing the peaks; a further research area is the development of faster calibration algorithms for the optical filter driver as the faster the filter is driven, the faster the filter will de-calibrate.

Appendix A

Summary of Electrical Sensor Errors

A.1 Summary of Electrical Sensor Errors

In this section tables of the induced voltages for sensors placed on different panels and under different temperatures are summarised.

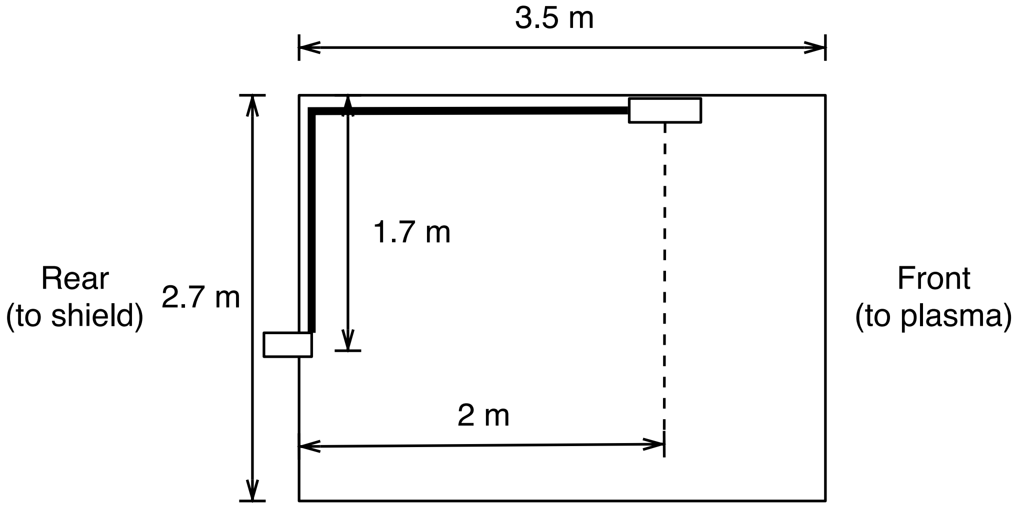

Figure A.1: Side view of port plug ceiling sensor (strain gauge or thermocouple)

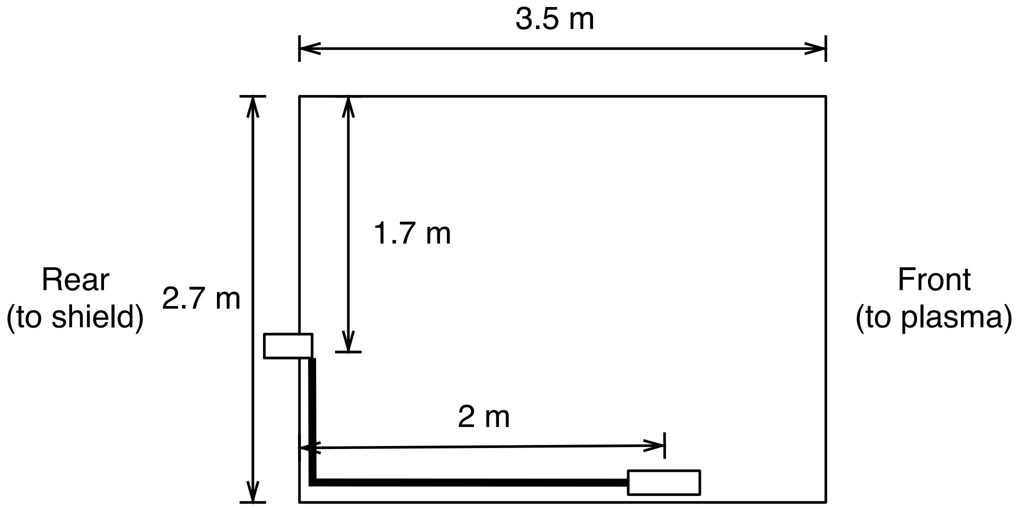

Figure A.2: Side view of port plug floor sensor

In Figures 2.10 to A.4 the layouts for sensors on each panel are presented. Table A.1 displays the % error in thermocouple measurements for K and N type thermocouples during a VDE (EMI only). Table A.5 displays the % error resulting during a VDE resulting from EMI for different strains.

Table A.3 displays the percentage error in the signal resulting from radiation and temperature induced e.m.fs. Table A.4 shows the percentage error in thermocouple signals resulting from the RIEMF/TIEMF plus the transmutation of the thermocouple.

Table A.1: Summary of the % errors for different panels in port plug for thermocouples at different temperatures under magnetic flux changes during a VDE

Panel	Induced V	% Error			
		K-type		N-type	
	μV	100°C	220°C	100°C	220°C
Rear	130	3.2	1.5	4.7	2.0
Top	331	8.1	3.7	12	5.0
Bottom	361	8.8	4.0	13	5.5
Front	465	12	5.2	17	7.1
Side	514	13	5.8	19	8.0

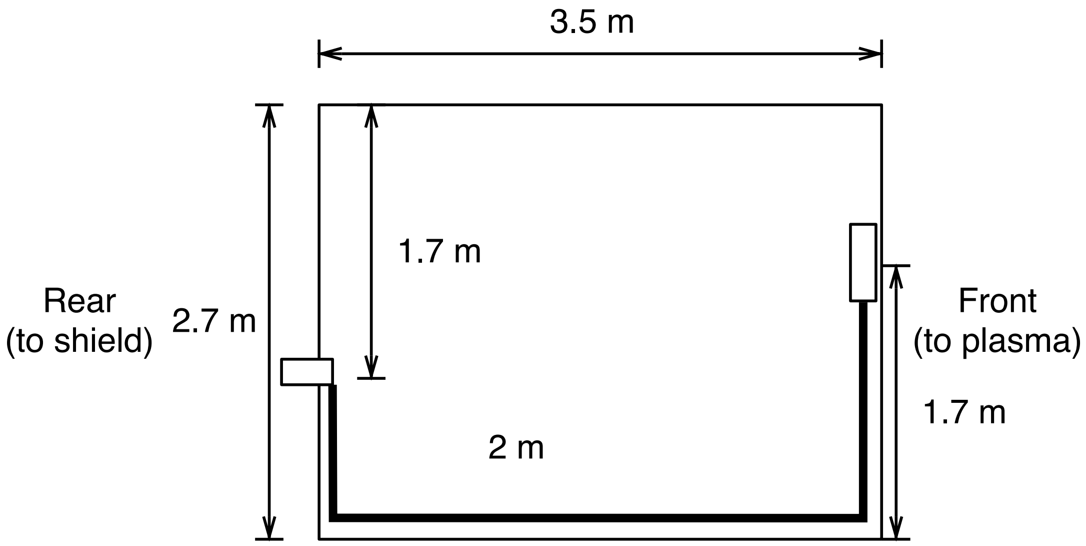

Figure A.3: Side view of port plug front face sensor

Table A.2: Summary of the maximum expected % errors for different panels in port plug for thermocouples at different temperatures under magnetic flux changes and including transmutation of thermocouple

Panel	Induced V	% Error			
		K-type		N-type	
	μV	100°C	220°C	100°C	220°C
Rear	130	4.2	2.5	5.7	3.0
Top	331	9.1	4.7	13	6.0
Bottom	361	9.8	5.0	14	6.5
Front	465	12.0	6.2	18	8.1
Side	514	14	6.8	20	8.8

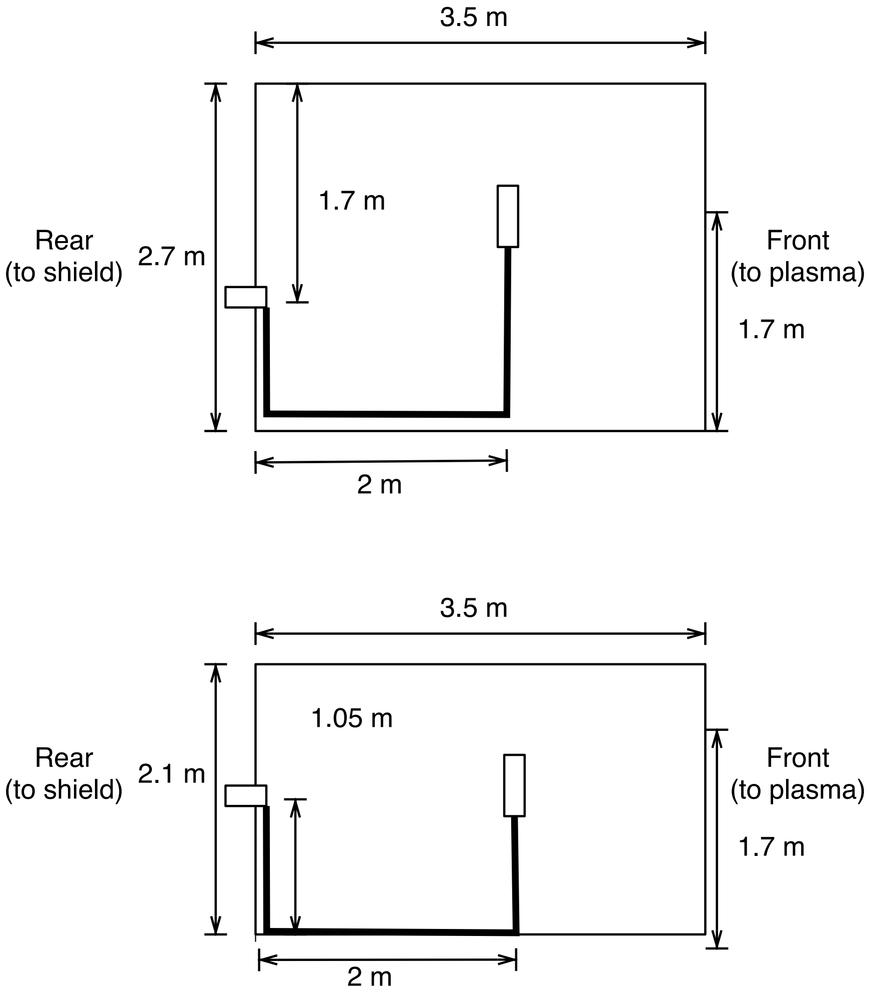

Figure A.4: Side view of port plug side sensor (top). Top view of port plug side sensor (bottom).

Table A.3: Estimated TIEMF/ RIEMF induced % error

Panel	RIEMF/ TIEMF	% Error			
		K-type		N-type	
	μV	100°C	220°C	100°C	220°C
Rear	10	0.24	0.11	0.36	0.15
Top	20	0.49	0.22	0.72	0.30
Bottom	20	0.49	0.22	0.72	0.30
Front	30	0.73	0.34	1.08	0.46
Side	40	0.98	0.45	1.44	0.61

Table A.4: Estimated maximum TIEMF/ RIEMF + 1%Transmutation error (during normal operation)

Panel	RIEMF/ TIEMF	% Error			
		K-type		N-type	
	μV	100°C	220°C	100°C	220°C
Rear	10	1.24	1.11	1.36	1.15
Top	20	1.49	1.22	1.72	1.30
Bottom	20	1.49	1.22	1.72	1.30
Front	30	1.73	1.34	2.08	1.46
Side	40	1.98	1.45	2.44	1.61

Table A.5: Summary of the errors for different panels in port plug for strain gauges under different strains during a VDE

	Induced V	% Error	
Panel	μV	100$\mu\varepsilon$	1000 $\mu\varepsilon$
Rear	130	31	3.1
Top	331	80	8.0
Bottom	361	87	8.7
Front	465	110	11
Side	514	125	12

Appendix B

2nd Moment of Inertia

B.1 Definition of the Second Moment of Area

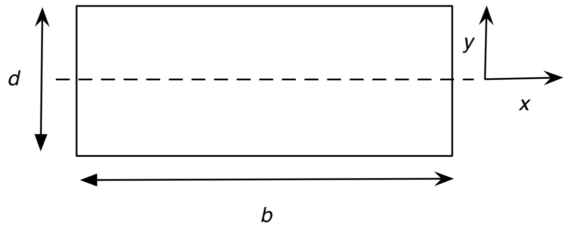

Figure B.1: Diagram of beam cross-section, d being the thickness of the beam and b being the width of the beam.

The second moment of area is written as I_{XX} and is defined as

$$I_{XX} = \int_A y^2 dA \tag{B.1}$$

for a rectangular cross-section as shown below in Figure B.1

For a beam as defined in Figure B.1 the second moment of inertia is calculated as below.

$$\begin{aligned} I_{XX} &= \int_{-d/2}^{d/2} y^2 dA && \text{(B.2)} \\ dA &= b\,dy && \text{(B.3)} \\ \Rightarrow I_{XX} &= \int_{-d/2}^{d/2} y^2 b dy && \text{(B.4)} \\ \Rightarrow I_{XX} &= \left[\frac{by^3}{3}\right] && \text{(B.5)} \\ \Rightarrow I_{XX} &= \frac{bd^3}{12} && \text{(B.6)} \end{aligned}$$

B.2 Quantisation error

The maximum quantisation error of a sampled measurement signal, for the acse where the values are rounded up or down is

$$e_{max} = \pm\frac{q}{2} \tag{B.7}$$

where q is the interval between quantisation levels and can be expressed by

$$q = \frac{V_{fs}}{2^N - 1} \approx \frac{V_{fs}}{2^N} \tag{B.8}$$

where V_{fs} is the full-scale input voltage of the N-bit resolution A/D convertor.

The quantisation error for each sample, e, is typically assumed to be random and normally distributed in the interval ± q/2 with zero mean. Under these conditions, the quantisation noise power, or variance, is expressed by

$$\sigma_e^2 = \int_{-q/2}^{q/2} e^2 P(e)\, de = \frac{1}{q}\int_{-q/2}^{q/2} e^2\, de = \frac{q^2}{12} \tag{B.9}$$

where $P(e)$ is the probability of value e occurring for each sample [5].

Appendix C

Metal Coating Process

Fibre Preparation Process

1 Cut two lengths of CuBall coated fibre 20cm each (fibres 1 & 2)

2 Remove CuBall coating from all four ends of lengths using nitric acid.

3 Rinse ends of stripped fibre in water to remove acid. Clean with ethanol.

4 Cleave ends of stripped fibres 1 & 2 leaving 10 mm of bare fibre with cleaved end

5 Cut length, ≈250 cm, of SM fibre

6 Dip in chloromethane solution for approximately 4 minutes in glass trough within a fume cupboard.

7 Remove acrylate coating by gently pulling on the now weakened coating. Wear protective gloves.

8 Cleave ends of stripped fibre to maximum length of 210mm (fibre 3)

9 Clean ends of fibre 1, 2 & 3 using ethanol on lint free paper

10 Splice using standard programme 9, fibre 1 to fibre 3

11 Splice fibre 2 to fibre 3

Silver Coating Process

12 Prepare 150ml ammoniacal silver nitrate as described in instructions (DO NOT ADD GLUCOSE SOLUTION)

13 Attach spliced fibres to metal/ PE frame using electrical tape

14 Place frame and fibre in trough, carefully placing fibre ends out of trough and around frame

15 Pour in ammoniacal silver nitrate solution into trough; make sure that fibre is covered.

16 Add glucose solution and gently mix with a spatula avoiding contact with the fibre in solution.

17 Leave for 2.5 minutes in solution

18 Remove from solution and gently rinse with tap water using a beaker or other vessel to pour water over fibre.

Metal Embedding Process

19 File edge of trench at each end of metal piece to a rounded edge. Make sure that edges are not rough.

20 Clean metal piece with ethanol.

21 Place metal piece on quartz strip in the marked position.

22 Stick using a thin layer of super glue the ends of the coated fibre to the end of the quart piece and the other end to a piece of metal that acts as a weight to provide tension. With fibre lying in middle of trench in metal piece use electrical tape to initially position and hold whilst the glue dries. Leave for up to 1 hour or until dry.

23 Prepare flux using HT flux powder, few drops of water and 1 drop of detergent. Mix until it is wall paper paste like in density.

24 Cut length of silver solder equal to length of metal piece using heavy snips.

25 Brush a thin layer of prepared flux into trench and fibre. Remove any excess from surrounding metal with paper tissue.

26 Place solder on top of trench.

27 Switch on water cooler and induction heating systems

28 Open gas supply cylinder but keep flow meter closed.

29 Carefully place quartz strip with components in work tube.

30 Set heating induction system to heat at 300A for 47s

31 Open flow meter until flow is half the maximum of meter.

32 Press start button on heating induction system

33 Watch as solder is heated and melts

34 At end of heating cycle leave gas supply on for approximately 3 minutes

35 Switch gas supply off

36 Remove quartz strip from work tube

37 Leave to cool in air for at least 10 minutes before touching

38 Carefully snip the fibre that is glued down as far from metal as possible.

39 Manufacturing complete.

40 Switch off induction heater, cooler and close gas cylinder. If doing further embedding then these can be left on.

References

[1] (2007) ITER future and DEMO. [Online]. Available: http://ec.europa.eu/research/energy/euratom/index$_e n.cfm?pg = fusionsection = iter - future$

[2] J. Brown, "Structural health monitoring of civil infrastructure," *Philosophical Transactions of the Royal Society A: Mathematical, Physical and Engineering Sciences*, vol. 365, no. 1851, pp. 589–622, 2007. [Online]. Available: http://rsta.royalsocietypublishing.org/content/365/1851/589.abstract

[3] M. J. Walsh, M. Beurskens, P. G. Carolan, M. Gilbert, M. Loughlin, A. W. Morris, V. Riccardo, Y. Xue, R. B. Huxford, and C. I. Walker, "Design challenges and analysis of the ITER core LIDAR thomson scattering system," *Review of Scientific Instruments*, vol. 77, no. 10, pp. 10E525–10E525–4, Oct 2006.

[4] E. H. Smith, *Mechanical Engineers Reference Book.* Elsevier Butterworth-Heinemann, 1998.

[5] P. Niewczas, "Implementation of a Faraday effect based optical current transducer using digital signal processing techniques," Ph.D. dissertation, University of Strathclyde, Centre for Electrical Power Engineering, Department of Electronic and Electrical Engineering, Glasgow G1 1XW, UK, June 2000.

[6] G. Recktenwald. Conversion of thermocouple voltage to temperature.

[7] IEC. IEC 60584 part 1: Thermocouples. reference tables.

[8] Bureau International des Poids et Mesures. (1968) The International Practical Temperature Scale of 1968 (IPTS-68). [Online]. Available: http://www.bipm.org/en/si/history-si/temp$_{s}cales/ipts - 68.html$

[9] I. S.-C. 65B:, "IEC 60584 part 2: Thermocouples: Tolerances," International Electrotechnical Committee, Tech. Rep., 1995.

[10] N. H. Balshaw, Y. Krivchenkov, G. Phillips, S. Davis, and R. Pampin-Garcia, "Iter diagnostic port plug design," *FUSION SCIENCE AND TECHNOLOGY*, vol. 56, pp. 661–665, August 2009.

[11] K. S. Krane, *Introductory Nuclear Physics*. John Wiley and sons, 1987.

[12] J. Wesson, *Tokamaks*, 2nd ed. Oxford, United Kingdom: Oxford University Press, 1997.

[13] R. E. Martin, "The use of thermocouples which transmute during service in nuclear reactors," Atomic Energy of Canada Limited, Chalk River Nuclear Laboratories, Chalk River, Ontario, Canada, Tech. Rep. AECL-6967, June 1978.

[14] S. J. Zinkle and E. R. Hodgson, "Radiation-induced changes in the physical properties of ceramic materials," *Journal of Nuclear Materials*, vol. 191–194, pp. 58–66, 1992.

[15] R. Van Nieuwenhove and L. Vermereen, "Irradiation effects on temperature sensors for ITER applications," *Review of Scientific Instruments*, vol. 75, no. 1, pp. 75–83, January 2004.

[16] V. Riccardo, P. Andrew, M. Buzio, A. Kaye, and P. Noll, "Asymmetric vertical displacement events at JET," *Fusion Engineering Eng.*, pp. 112–115, 1997.

[17] T. Shikama, M. Narui, and T. Sagawa, "Radiation induced electromotive force in mineral insulated cable under reactor irradiation," *Nuclear Instruments and Methods in Physics Research Section B: Beam Interactions with Materials and Atoms*, vol. 122, no. 4, pp. 650 – 656, 1997. [Online].

Available: http://www.sciencedirect.com/science/article/B6TJN-3SP6D7X-61/2/7a1df8bbf72120fcc7263bada0bd5ba1

[18] R. Van Nieuwenhove and L. Vermeeren, “Study of the radiation induced electromotive force (riemf),” SCK.CEN, Mol, Belgium, Tech. Rep., 2003.

[19] R. Van Nieuwenhove, “Study of the radiation induced electromotive force effect on mineral insulated cables for magnetic diagnostics in iter,” *Fusion Engineering and Design*, vol. 66, pp. 821–825, 2003.

[20] R. Vila and E. R. Hodgson, “Report on in-situ radiation tests for MI cable coils, RIEMF voltage and current,” CIEMAT, Spain, Tech. Rep., June 2003.

[21] R. W. Klaffky, B. H. Rose, A. N. GOland, and G. J. Dienes, “Radiation-induced conductivity of Al_2O_3 : Experiment and theory,” *Physical Review B: Condensed Matter*, vol. 21, pp. 3610–3640, 1980.

[22] T. Shikama and M. Narui, “Radiation induced conductivity of ceramic insulators measured in a fission reactor,” *Journal of Nuclear Materials*, vol. 192-194, pp. 575–578, 1992.

[23] K. Noda, T. Nakazawa, Y. Oyama, D. Yamaki, and Y. Ikeda, “First in situ measurement of electrical resistivity of ceramic insulator during irradiation with neutrons of energy 14 MeV,” *Fusion Engineering and Design*, vol. 29, pp. 448–454, 1995.

[24] C. Patuwathavithane, W. Y. Wu, and R. H. Zee, “Radiation induced conductivity in alumina,” *Journal of Nuclear Materials*, vol. 225, pp. 328–335, 1995.

[25] L. Snead, D. White, and S. Zinkle, “Investigation of radiation induced electrical degradation in alumina under ITER-relevant conditions,” *Journal of Nuclear Materials*, vol. 226, pp. 58–66, 1995.

[26] T. Tanifuji, Y. Katano, T. Nakazawa, and K. Noda, “Electrical conductivity change in single crystal $\mathrm{Al_2O_3}$ and MgO under neutron and gamma-ray irradiation,” *Journal of Nuclear Materials*, vol. 253, pp. 156–166, March 1998.

[27] T. Shikama and S. J. Zinkle, “Long term degradation of electrical insulation of Al_2O_3 under high flux fission reactor irradiation,” *Journal of Nuclear Materials*, vol. 258–263, pp. 1861–1866, 1998.

[28] Y. Gao and et al, “A study on radiation effect of $<$ 200 kev protons on m40j/epoxy composites,” *Nuclear Instrumentation and Methods in Physics Research Section B*, pp. 261–268, 2005.

[29] ITER Technical Team, “ITER Technical Basis,” ITER Coordination Committee, Tech. Rep., 2001.

[30] S. Kruger, D. D. Schnack, and C. R. Sovinec, “Dynamics of the major disruption of a DIII-D plasma,” *Plasma Physics*, 2005.

[31] V. Riccardo, S. Walker, and P. Noll, “Parametric analysis of asymmetric vertical displacement events at JET,” *Plasma Physics*, vol. 42, pp. 29–40, 2000.

[32] E. Bertolini, M. Buzio, P. Noll, T. Raimondi, G. Sannazzaro, and M. Verrecchia, “Engineering analysis of JET operation,” in *Proc. of the 16th Symposium on Fusion Engineering*, vol. 1, Champaign (III, USA), October 1995, pp. 464–469.

[33] P. Niewczas, G. Fusiek, C. Lescure, M. Johnson, E. Irvings, A. West, P. Crolla, and M. Walsh, “Concept level evaluation of the full-scale deployment of fibre bragg grating sensors for measuring forces in jet during plasma disruption events,” in *Proceedings of Condition Monitoring 2008.* BINDT, September 2008.

[34] L. Vermeeren and M. WÈber, “Induced voltages and currents in copper and stainless steel core mineral insulated cables due to radiation and thermal gradients,” *Fusion Engineering and Design*, vol. 82, no. 5-14, pp. 1185 – 1191, 2007, proceedings of the 24th Symposium on Fusion Technology - SOFT-24. [Online]. Available: http://www.sciencedirect.com/science/article/B6V3C-4P00S52-5/2/279ba05ea9a7e2a5af2432a3e5ce1842

[35] G. Federici, C. H. Skinner, J. N. Brooks, J. P. Coad, C. Grisolia, A. A. Haasz, A. Hassanein, V. Philipps, C. S. Pitcher, J. Roth, W. R. Wampler, and D. G.

Whyte, "Plasma-material interactions in current tokamaks and their implications for next-step fusion reactors," Princeton Plasma Physics Laboratory (Princeton, NJ USA) and the Max-Planck-Institut für Plasmaphysik, (Garching, Germany), Tech. Rep., January 2001.

[36] C. Lescure, S. Hotchin, E. Ivings, M. F. Johnson, V. Riccardo, M. Walsh, A. West, G. Fusiek, and P. Niewczas, "Measurement of disruption forces in jet using fiber-optic sensors," *Fusion Engineering, 2009. SOFE 2009. 23rd IEEE/NPSS Symposium on*, pp. 1–4, 1-5 June 2009.

[37] P. Orr and P. Niewczas, "An optical fibre system design enabling simultaneous point measurement of magnetic field strength and temperature using low-birefringence fbgs," *Sensors and Actuators A: Physical*, vol. 163, no. 1, pp. 68–74, 9 2010. [Online]. Available: http://www.sciencedirect.com/science/article/pii/S0924424710003183

[38] M. Turenne, R. Johnson, F. Hunte, J. Schwartz, and H. Song, "Multi-purpose fiber optic sensors for high temperature superconducting magnets," *Fusion Engineering, 2009. SOFE 2009. 23rd IEEE/NPSS Symposium on*, pp. 1–4, 1-5 June 2009.

[39] F. Morange, P. Ferdinand, B. Jarret, and et al, "Capteurs à fibres optiques et réseaux associés. etat de l'art - tendances du marché - propositions d'actions (optical fibre sensors and related networks. state of the art - market trends - development proposals)," EDF R&D, Tech. Rep. Ref. EDF/Dir. de 1'Equipement/SEPTEN/EL92-94, 1994.

[40] EPRI, "Research planning study of fiber-optic sensors," Electrical Power Research Institute, Tennesse, USA, Tech. Rep. EPRI ER-6428, August 1989.

[41] P. Ferdinand, S. Magne, O. Roy, V. Dewynter Marty, S. Rougeault, and M. Bugaud, "Optical fiber sensors for the nuclear environment," *Optical Sensors and Microsystems*, pp. 205–226, 2000. [Online]. Available: http://dx.doi.org/10.1007/0-306-47099-3$_1$8

[42] G. Breuzé, P. Jucker, J. Serre, E. Garnero, T. Hamet, and D. Colas, "Fiber optics compatiblity with radiation environment inside PWR containment," in *IAEA*

Specialists' Meeting on "Improvements in Nuclear and Radiation Instrumentation for Nuclear Power Plants". Saclay, France: CEA, 18-20 Oct 1993, p. 1644.

[43] M. Kyoto and et al., "Gamma-ray radiation hardened properties of pure silica core single-mode fiber and its data links system in radioactive environment," *Journal of Lightwave Technology*, vol. 10, no. 3, pp. 289–294, 1992.

[44] M. Buric, T. Chen, M. Maklad, P. R. Swinehart, and K. P. Chen, "Multiplexable low-temperature fiber bragg grating hydrogen sensors," *Photonics Technology Letters, IEEE*, vol. 21, no. 21, pp. 1594–1596, 2009.

[45] J. P. Dakin and B. Culshaw, *Optical Fiber Sensors: Principles and Components v. 1.* Artech House, November 1988, vol. 1.

[46] J. Canning, M. Stevenson, S. Bandyopadhyay, and K. Cook, "Extreme silica optical fibre gratings," *Sensors*, vol. 8, no. 10, pp. 6448–6452, 2008. [Online]. Available: http://www.mdpi.com/1424-8220/8/10/6448

[47] H. A. Macleod, *Thin-film Optical Filters.* Adam Hilger Ltd, Bristol, 1986.

[48] S. Spinner and R. M. Waxler, "Relation between refractive index and density of glasses resulting from annealing compared with corresponding relation resulting from compression," *Applied Optics*, vol. 5, p. 1887, Dec. 1966.

[49] R. O. Davies, "Avogadro's number and Avogadro's constant," *Physics Education*, vol. 8, p. 275, 1973.

[50] D. PDA and R. Kashyap, *Fiber Bragg gratings* [*internet resource*]. London : Academic, c2010.

[51] J.-L. Archambault, L. Reekie, and P. Russell, "100% reflectivity Bragg reflectors produced in optical fibres by single excimer laser pulses," *Electronics Letters*, vol. 29, no. 5, pp. 453–455, 1993.

[52] L. Dong and W. F. Liu, "Thermal decay of fiber Bragg gratings of positive and negative index changes formed at 193 nm in a boron-codoped germanosilicate fiber," *Appl. Opt.*, vol. 36, no. 31, pp. 8222–8226, Nov. 1997. [Online]. Available: http://ao.osa.org/abstract.cfm?URI=ao-36-31-8222

[53] M. Fokine, "Growth dynamics of chemical composition gratings in fluorine-doped silica optical fibers," *Optics Letters*, vol. 27, no. 12, pp. 1759–1765, Jun 2002.

[54] A. F. Fernandez, B. Brichard, A. Gusarov, H. Ooms, C. van Ierschot, F. Berghmans, M. Fokine, and M. Popov, "Behaviour of chemical composition gratings in a very harsh mixed gamma neutron irradiation field," a first look at the effects of radiation on chemical composition gratings.

[55] G. Brambilla and H. Rutt, "Fiber Bragg gratings with enhanced thermal stability," *Applied Physics Letters*, vol. 80, no. 18, pp. 3259–3261, May 2002.

[56] J. Juergens, G. Adamovsky, R. Bhatt, G. Morscher, and B. Floyd, "Thermal evaluation of fiber Bragg gratings at extreme temperatures," NASA, Glenn Research Center, Cleveland, Ohio, Tech. Rep. NASA/TM – 2005-213560, March 2005.

[57] S. Trpkovski, D. J. Kitcher, G. W. Baxter, S. F. Collins, and S. A. Wade, "High-temperature-resistant chemical composition Bragg gratings in Er^{3+}-doped optical fiber," *Optical Letters*, vol. 30, no. 6, pp. 607–609, 2005. [Online]. Available: http://ol.osa.org/abstract.cfm?URI=ol-30-6-607

[58] S. Pal, J. Mandal, T. Sun, K. T. V. Grattan, M. Fokine, F. Carlsson, P. Y. Fonjallaz, S. A. Wade, and S. F. Collins, "Characteristics of potential fibre Bragg grating sensor-based devices at elevated temperatures," *Measurement Science and Technology*, vol. 14, no. 7, pp. 1131–1136, 2003. [Online]. Available: http://stacks.iop.org/0957-0233/14/1131

[59] W. Primak, *The Compacted States of Silica*, ser. Studies in Radiation Effects in Solids, G. J. Dienes and L. T. Chadderton, Eds. Gordon and Breach Science Publishers, 1975, vol. 4.

[60] B. Brichard, A. F. Fernandez, H. Ooms, and F. Berghmans, "Fibre-optic gamma-flux monitoring in a fission reactor by means of cerenkov radiation," *Measurement Science and Technology*, vol. 18, no. 10, p. 3257, 2007. [Online]. Available: http://stacks.iop.org/0957-0233/18/i=10/a=S32

[61] E. J. Friebel, K. Long, C. Askins, M. Gingerich, M. Marrone, and D. Griscom, "Overview of radiation effects in fiber optics," *Proc. SPIE*, vol. 541, pp. 70–88, 1985.

[62] P. Borgermans and B. Brichard, "Kinetic models and spectral dependencies of the radiation-induced attenuation in pure silica fibers," *IEEE Transactions on Nuclear Science*, vol. 49, no. 3, pp. 1439–1445, Jun 2002.

[63] P. Borgermans, B. Brichard, and M. C. Decreton, "Models for the radiation-induced attenuation in pure silica optical fibers: spectral dependencies and absorption band kinetics," in *Photonics for Space and Radiation Environments II*, F. Berghmans and E. W. Taylor, Eds., vol. 4547, no. 1. SPIE, 2002, pp. 53–60. [Online]. Available: http://link.aip.org/link/?PSI/4547/53/1

[64] B. Brichard, A. Fernandez, H. Ooms, P. Borgermans, and F. Berghmans, "Dependence of the POR and NBOHC defects as function of the dose in hydrogen-treated and untreated KU1 glass fibers," *IEEE Transactions On Nuclear Science*, vol. 50, no. 6, pp. 2024–2029, Dec. 2003.

[65] H. Henschel, O. Kohn, and U. Weinand, "Radiation hardening of pure silica optical fibers by high-pressure hydrogen treatment," *IEEE Transactions On Nuclear Science*, vol. 49, no. 3, pp. 1401–1409, Jun. 2002.

[66] F. Jensen, E. Takada, M. Nakazawa, T. Kakuta, and S. Yamamoto, "Consequences of radiation effects on pure-silica-core optical fibers used for Raman-scattering-based temperature measurements," *IEEE Transactions On Nuclear Science*, vol. 45, no. 1, pp. 50–58, Feb. 1998.

[67] H. Henschel and et al, "Comparison between fast neutron and gamma irradiation of optical fibres," *IEEE Transactions on Nuclear Science*, vol. 45, no. 3, pp. 1543–1549, Jun 1998.

[68] F. Berghans and et al, "Evaluation of three different optical fibre temperature sensor types for application in gamma radiation environments," *IEEE Transactions on Nuclear Science*, vol. 45, no. 3, pp. 1537–1542, Jun 1998.

[69] A. Fernandez Fernandez, B. Brichard, O. V. Butov, K. M. Golant, and A. V. Lanin, “High radiation tolerance of temperature resistant Bragg gratings written in n-doped silica-core fibres up to MGy dose levels,” in *Third European Workshop on Optical Fibre Sensors*, A. Cutolo, B. Culshaw, and J. M. López-Higuera, Eds., vol. 6619. SPIE, 2007.

[70] A. Fernandez Fernandez, A. Gusarov, B. Brichard, M. Decréton, F. Berghmans, P. Mégret, and A. Delchambre, “Long-term radiation effects on fibre Bragg grating temperature sensors in a low flux nuclear reactor,” *Measurement Science and Technology*, vol. 15, no. 8, pp. 1506–1511, 2004. [Online]. Available: http://stacks.iop.org/0957-0233/15/1506

[71] T. Shikama, T. Kakuta, N. Shamoto, M. Narui, and T. Sagawa, “Behavior of developed radiation-resistant silica-core optical fibers under fission reactor irradiation,” *Fusion Engineering and Design*, vol. 51-52, pp. 179–183, 2000.

[72] F. Berghmans, A. F. Fernandez, B. Brichard, F. Vos, M. Decréton, A. Gusarova, O. Deparis, P. Mégretb, M. Blondel, and S. C. andAndré Morin, “Radiation hardness of fiber-optic sensors for monitoring and remote handling applications in nuclear environments,” in *Proceedings of SPIE International Symposium on Industrial and Environmental Monitors and Biosensors*, 1998.

[73] H. Henschel, S. K. Hoeffgen, K. Krebber, J. Kuhnhenn, and U. Weinand, “Influence of fiber composition and grating fabrication on the radiation sensitivity of fiber bragg gratings,” *Radiation and Its Effects on Components and Systems, 2007. RADECS 2007. 9th European Conference on*, pp. 1–8, 10-14 Sept. 2007.

[74] H. Bach and N. Neuroth, Eds., *THE PROPERTIES OF OPTICAL GLASS*. Springer, 1998.

[75] H. Henschel, D. Grobnic, S. K. Hoeffgen, J. Kuhnhenn, S. J. Mihailov, and U. Weinand, “Development of highly radiation resistant fiber bragg gratings,” *IEEE TRANSACTIONS ON NUCLEAR SCIENCE*, vol. 58, no. 4, pp. 2103–2111, August 2011.

[76] A. Gusarov, A. Fernandez Fernandez, S. Vasiliev, O. Medvedkov, M. Blondel, and F. Berghmans, “Effect of gamma–neutron nuclear reactor radiation on the

properties of bragg gratings written in photosensitive ge-doped optical fiber," *Nuclear Instruments and Methods in Physics Research Section B: Beam Interactions with Materials and Atoms*, vol. 187, no. 1, pp. 79–86, 1 2002. [Online]. Available: http://www.sciencedirect.com/science/article/pii/S0168583X01008291

[77] A. Gusarov and et al, "Behavior of fibre Bragg gratings under high total dose gamma radiation," *IEEE Trans. Nucl. Sci*, vol. 47, no. 3, pp. 688–692, Jun 2000.

[78] A. Fernandez Fernandez, B. Brichard, F. Berghmans, H. E. Rabii, M. Fokine, and M. Popov, "Chemical composition fiber gratings in a high mixed gamma neutron radiation field," *IEEE Transactions on Nuclear Science*, vol. 53, no. 3, pp. 1607 – 1613, June 2006.

[79] A. Gusarov, Y. Defosse, O. Deparis, M. Blondel, A. Fernandez, F. Berghmans, and M. Decréton, "Effect of ionizing radiation on the properties of fibre Bragg gratings written in ge-doped fibre," in *2001 OSA Technical Digest Series*. Optical Society of America, Jul. 2001, pp. BThC30–. [Online]. Available: http://www.opticsinfobase.org/abstract.cfm?URI=URI=BGPP-2001-BThC30

[80] A. Gusarov and et al, "High total dose radiation effects on temperature sensing fiber Bragg gratings," *IEEE Phot. Technol. Lett.*, vol. 11, no. 9, pp. 1159–1161, Sept 1999.

[81] C. Zhan, Y. Zhu, S. Yin, and P. Ruffin, "Multi-parameter harsh environment sensing using asymmetric Bragg gratings inscribed by IR femtosecond irradiation," *Optical Fiber Technology*, vol. 13, no. 2, pp. 98 – 107, 2007. [Online]. Available: http://www.sciencedirect.com/science/article/B6WP0-4MM95VK-2/2/48a5281c175f0c84743a7295b8aeb699

[82] X. Shu, D. Zhao, L. Zhang, and I. Bennion, "Use of dual-grating sensors formed by different types of fiber Bragg gratings for simultaneous temperature and strain measurements," *Applied Optics*, vol. 43, no. 10, p. 2006, April 2004.

[83] Ampotonix, "Amphotonix optical filters and lasers." [Online]. Available: http://www.amphotonix.com

[84] G. F. Fernando, T. Liu, P. Crosby, C. Doyle, A. Martin, D. Brooks, B. Ralph, and R. Badcock, "A multi-purpose optical fibre sensor design for fibre reinforced

composite materials," *Measurement Science and Technology*, vol. 8, no. 10, pp. 1065–1079, 1997. [Online]. Available: http://stacks.iop.org/0957-0233/8/1065

[85] M. Singh, C. J. Tuck, and G. F. Fernando, "Multiplexed optical fibre Fabry-Perot sensors for strain metrology," *Smart Materials and Structures*, vol. 8, no. 5, 1999. [Online]. Available: http://stacks.iop.org/0964-1726/8/i=5/a=304

[86] S. Magne, S. Rougeault, M. Vilela, and P. Ferdinand, "State-of-strain evaluation with fiber bragg grating rosettes: application to discrimination between strain and temperature effects in fiber sensors," *Appl. Opt.*, vol. 36, pp. 9437–9447, 1997.

[87] S. Sandlin and A. Hokkanen, "Embedding optical fibers in metal alloys," *Instrumentation and Measurement Magazine*, vol. 6, pp. 31 – 36, 2003.

[88] (2004, Nov). [Online]. Available: http://web.archive.org/web/20041125103614/http://www.npl.co.uk/materials/functional/fos/

[89] Y.-J. Rao, "In-fibre Bragg grating sensors," *Measurement Science and Technology*, vol. 8, no. 4, pp. 355–375, 1997. [Online]. Available: http://stacks.iop.org/0957-0233/8/355

[90] M. Born and E. Wolf, *Principles of Optics.* Cambridge, 2006.

[91] B. J. Frey, D. B. Leviton, and T. J. Madison, "Temperature dependent refractive index of silicon and germanium," *Proceedings of SPIE*, vol. 6273, no. 3, p. 10, 2006. [Online]. Available: http://arxiv.org/abs/physics/0606168

[92] G. Cocorullo, F. G. Della Corte, and I. Rendina, "Temperature dependence of the thermo-optic coefficient in crystalline silicon between room temperature and 550 k at the wavelength of 1523 nm," *Applied Physics Letters*, vol. 74, no. 22, pp. 3338 –3340, may 1999.

[93] M. J. O'Dwyer, C.-C. Ye, S. W. James, and R. P. Tatam, "Thermal dependence of the strain response of the optical fibre bragg gratings," *Measurement Science and Technology*, vol. 15, pp. 1607–1613, 2004.

[94] W. Jin, W. C. Michie, G. Thursby, M. Konstantaki, and B. Culshaw, "Simultaneous measurement of strain and temperature: error analysis," *Optical Engineering*, vol. 36, no. 2, pp. 598–609, February 1997.

[95] B. Fredrik, H. Jensen, and et al, “Consequences of radiation effects on pure-silica-core optical fibers used for Raman-scattering-based temperature measurements,” *IEEE Transactions on Nuclear Science*, vol. 45, no. 1, pp. 50–58, Feb 1998.

[96] S. Sandlin and L. Heikinheimo, “Evaluation of a new method for metal embedding of optical fibres for high temperature sensing purposes,” in *Baltica V conference, Condition and Life management for power plants*, vol. 2, 2001, pp. 547 – 557.

[97] Oxford Electronics Ltd, “Cuball single mode optical fibre,” Online. [Online]. Available: http://www.oxford-electronics.com

[98] IVG Fiber, “Single-mode fiber with copper coating,” Online. [Online]. Available: www.ivgfiber.com

[99] C. Lupi, F. Felli, L. Ippoliti, M. A. Caponero, M. Ciotti, V. Nardelli, and A. Paolozzi, “Metal coating for enhancing the sensitivity of fibre Bragg grating sensors at cryogenic temperature,” *Smart Materials and Structures*, vol. 14, no. 6, pp. N71–N76, 2005.

[100] M. Ciotti, V. Nardelli, M. A. Caponero, F. Felli, C. Lupi, and L. Ippoliti, “An optical system for cryogenic temperature measurements,” *Smart Materials and Structures*, vol. 16, no. 5, pp. 1708–1711, 2007.

[101] Y. Feng, H. Zhang, Y.-L. Li, and C.-F. Rao, “Temperature sensing of metal-coated fiber bragg grating,” *IEEE/ASME Transactions on Mechatronics*, vol. 15, no. 4, pp. 511–519, Aug 2010.

[102] Y. Feng, H. Zhang, Y.-L. Li, and G. Peng, “Highly sensitive Ni-Cu duplex metal coated fiber Bragg grating temperature sensor,” in *Photonics and Optoelectronics, 2009. SOPO 2009. Symposium on*, 2009, pp. 1–4.

[103] G.-C. Lin, L. Wang, C. Yang, M. Shih, and T. Chuang, “Thermal performance of metal-clad fiber Bragg grating sensors,” *Photonics Technology Letters, IEEE*, vol. 10, no. 3, pp. 406–408, 1998.

[104] Characteristics of tin-lead solders. [Online]. Available: http://www.ami.ac.uk/courses/topics/0244$_tsm/index.html$

[105] X. Li, W. Tang, and A. Golnas, “Embedding and characterization of fiber-optic and thin-film sensors in metallic structures,” *Sensor Review*, vol. 24, no. 4, pp. 370–377, 2004.

[106] J. S. Leng, D. Winter, R. A. Barnes, G. C. Mays, and G. F. Fernando, “Structural health monitoring of concrete cylinders using protected fibre optic sensors,” *Smart Materials and Structures*, vol. 15, no. 2, pp. 302–308, 2006. [Online]. Available: http://stacks.iop.org/0964-1726/15/302

[107] S. Sandlin, T. Kosonen, A. Hokkanen, and L. Heikinheimo, “Use of brazing technique for manufacturing of high temperature fibre optical temperature and displacement transducer,” *Materials Science and Technology*, vol. 23, pp. 1249–1255(7) ,, October 2007. [Online]. Available: http://www.ingentaconnect.com/content/maney/mst/2007/00000023/00000010/art00018

[108] X. C. Li, F. Prinz, and J. Seim, “Thermal behavior of a metal embedded fiber Bragg grating sensor,” *Smart Materials and Structures*, vol. 10, pp. 575–579, 2001.

[109] H. Alemohammad and E. Toyserkani, “Simultaneous measurement of temperature and tensile loading using superstructure FBGs developed by laser direct writing of periodic on-fiber metallic films,” *Smart Materials and Structures*, vol. 18, no. 9, pp. 095 048–, 2009.

[110] H. R. Alemohamad, E. Foroozmehr, B. Cotten, and E. Toyserkani, “A dual-parameter optical fiber sensor for concurrent strain and temperature measurement: design, fabrication, packaging, and calibration,” *Journal of Lightwave Technology*, vol. TBC, 2013.

[111] V. Rudnev, D. Loveless, R. Cook, and M. Black, *Handbook of Induction Heating.* CRC, 2003, ch. 3.

[112] Ameritherm. Applications of induction heating.

[113] V. Shidlovski. Superluminescent diodes. Short overview of device operation principles and performance parameters.

[114] F. Koyama, “High power superluminescent diodes for multi-wavelength light sources,” in *Lasers and Electro-Optics Society Annual Meeting, 1997. LEOS ’97*

10th Annual Meeting. Conference Proceedings., IEEE, vol. 1, nov 1997, pp. 333 –334 vol.1.

[115] (2009, March). [Online]. Available: http://www.rp-photonics.com/amplified$_s$*pontaneous*$_e$*mission.html*

[116] National Instruments. [Online]. Available: http://www.ni.com

[117] H. L. Hartnagel, J. Pfeiffer, K. Mutamba, J. Peerlings, R. Riemenschneider, and P. Meissner, "III-V membrane structures for tunable Fabry-Perot filters and sensor applications," *Optoelectronic and Microelectronic Materials Devices, 1998. Proceedings. 1998 Conference on*, pp. 49–56, 1999.

[118] J. Graeme, *Photodiode Amplifiers: OP AMP Solutions.* McGraw-Hill, 1996.

[119] A. J. Willshire, "Robust optical-sensor systems for aero-engine monitoring," Ph.D. dissertation, University Of Strathclyde, 2004.

[120] E. Taylor, "Advancement of radiation effects research in photonic technologies: Application to space platforms and systems," *Proc. SPIE*, vol. CR66, pp. 58–92, 1997.

[121] H. Henschel, O. Kohn, and H. Schmidt, "Radiation sensitivity of fiber optic couplers," *Proc. SPIE*, vol. 1791, pp. 151–163, 1992.

[122] R. Gutierez, G. Swift, S. Dubovitsky, R. Bartman, C. Barnes, and L. Dorsky, "Radiation effects on fused biconical taper wavelength division multiplexer," *IEEE Transactions on Nuclear Science*, vol. 41, pp. 1950–1957, December 1994.

[123] A. Fernandez Fernandez, F. Berghmans, B. Brichard, P. Borgermans, A. Gusarov, M. Van Ufflen, P. Megret, M. Decréton, M. Blondel, and A. Delchambre, "Radiation-resistant WDM optical link for thermonuclear fusion reactor instrumentation," *IEEE Transactions on Nuclear Science*, vol. 48, no. 5, pp. 1708–1712, 2001.

[124] *Corning SMF-28e+ Optical Fibre*, Corning, One Riverfront Plaza, Corning, USA, October 2008.

[125] National Instruments. Peak detection using labview and measurement studio. National Instruments.

[126] G. Fusiek, “Wavelength discriminating devices and spectrally encoded sensors for dynamic monitoring of electrical plant,” Ph.D. dissertation, University of Strathclyde, Glasgow, UK, 2007.

[127] J. Sanz, R. De La Fuente, and J. M. Perlado, “Impact of the neutron flux on transmutation products at fusion reactor first-walls,” *Journal of Nuclear Materials*, vol. 155–157, Part 2, no. 0, pp. 592–596, 7 1988. [Online]. Available: http://www.sciencedirect.com/science/article/pii/0022311588903789

[128] V. P. Wnuk, A. Méndez, S. Ferguson, and T. Graver, “Process for mounting and packaging of fiber bragg grating strain sensors for use in harsh environment applications,” in *Smart Structures Conference*, no. 5758-6. SPIE, 2005.

[129] Cupalloys - silver solder suppliers. [Online]. Available: www.cupalloys.co.uk

[130] BSI, “Brazing. Filler metals BS EN 1044-1999,” Online standard, September 1999.

[131] G. L. Squires, *Practical Physics.* Cambridge University Press, 1985.

[132] H. Benson, *University Physics.* Wiley, 1996. [Online]. Available: http://books.google.co.uk/books?id=C5fLlgEACAAJ

[133] G. McDearmon and B. Mathie, “Method and apparatus for shear strain testing of strain sensors,” US Patent, October 2009.